Structural deformation and mineralogy of the Agardhfjellet and Rurikfjellet formations in central Spitsbergen, Svalbard

Karoline Helen Løvlie

UNIS

The University Centre in Svalbard

Thesis submitted for the degree of
Master in Geosciences
60 credits

Department of Geosciences
The Faculty of Mathematics and Natural Sciences

UNIVERSITY OF OSLO

Spring 2020

Structural deformation and mineralogy of the Agardhfjellet and Rurikfjellet formations in central Spitsbergen, Svalbard

Karoline Helen Løvlie

Supervisors: Mark Mulrooney and Kim Senger. Co-supervisor: Elin Skurtveit

Structural deformation and mineralogy of the Agardhfjellet and Rurikfjellet formations in central Spitsbergen, Svalbard

http://www.duo.uio.no/

Printed: Reprosentralen, University of Oslo

Front page photo: Co-student Lise Nakken and the author gazing at Janusfjellet and the study area. The green cabin was the field camp for the second field campaign. Photo credits: Rakul Johannesen.

Abstract

The Upper Jurassic-Lower Cretaceous Agardhfjellet and Rurikfjellet formations comprise a 450 m thick shale-dominated succession. This succession is present across central parts of Spitsbergen, Svalbard, and is the targeted caprock for the Longyearbyen CO_2 Lab. The focus of this study has been on the Slottsmøya Member of the Agardhfjellet Formation and the Wimanfjellet Member of the Rurikfjellet Formation.

Structural measurements collected from two drill cores and two outcrops, located 15 km apart, are the basis of this study. Additionally, X-ray diffraction (XRD) and Scanning Electron Microscope (SEM) analyses have been conducted on two samples from one of the drill cores. The drill cores exhibit high fracture frequencies, dominated by low-angle shear fractures seen as polished surfaces with slickensides. The outcrops show highly fractured beds, with mainly high-angle open and shear fractures. Mode I and Mode II fractures are interpreted in both drill core and outcrop data. Contractional, meso-scale structures are observed in the field area. The recorded deformation is interpreted to be the result of tectonic events that has affected Spitsbergen after the deposition of the Agardhfjellet and Rurikfjellet formations. These events include the Cretaceous magmatic event which resulted in uplift, Paleogene transpression and Cenozoic deglaciation and erosion. The mineralogy is consistent with a typical shale composition, where clay minerals and quartz constituents show the highest fractions. XRD analyses determine that clay minerals comprise 35% and 51% of the Agardhfjellet and Rurikfjellet formations, respectively. The study shows that the Agardhfjellet and Rurikfjellet formations are highly fractured, with a décollement zone present along the boundary. This is interpreted as the primary reason for the highly deformed rock mass. However, the interval appears to have a good sealing property seen as a vertical pressure difference exists between the targeted reservoir and caprock succession. The reason for the functional seal is not fully understood, but appears to be related to several factors such as: (i) thickness resulting in satisfying confining pressure, (ii) large amounts of clay minerals, (iii) preferential orientation of existing fractures in relation to current stress regime, (iv) and a décollement zone forming a barrier for vertical fluid flow.

Acknowledgements

First of all I want to express gratitude to my supervisors Mark Mulrooney and Kim Senger, and co-supervisor Elin Skurtveit. Their guidance and input have helped me improve this work. I am especially grateful for the opportunity they gave me to spend time at UNIS and Svalbard, and to be able to study the world class geology in the high North.

Secondly, I want to thank my faithful study partner Lise Nakken. For your tolerance, kindness and for all the fun we've had during the last five years. It would not have been the same without you. I also want to thank all the friends I have made during the time as a geology student, you have made this time worthy of remembering. A special thanks to the guys at 217, for making the final stage of the thesis more fun.

Thanks to my family and friends for all the support and care. To my mom and stepdad for encouraging me when the work has been frustrating, and to my friends for making sure I have a social life besides working on this thesis. Thanks to my two brothers, for taking the time to check for typos and misspellings.

The field work would not have been possible to conduct without the wonderful field assistants who joined; Tom Birchall, Matthijs Nuus, Rakul Johannesen, Astrid Vikingstad and Peter Bethlem. Thank you so much for the fun, but intense days in field. And for scouting for polar bears when my eyes were staring at the never ending shale. Further, the people at the Logistics department at UNIS are acknowledged for supplying field equipment and quick evacuations when needed.

Thanks to the people helping me with lab work at UiO and preparing the samples needed for the SEM analysis.
Last, but not least, thanks to Ole for all the help with LaTeX and proofreading the text.

This thesis is for my dad, Lars. I hope you would have been proud.

Table of Contents

List of Figures

List of Tables

Chapter 1

Introduction

1.1 Background

Carbon Capture and Storage (CCS) is recognized as one of the main contributing methods to limit the ongoing increase of anthropogenic emissions of CO_2 by the Intergovernmental Panel on Climate Change (IPCC). By implementing CCS, there is an estimated reduction of 19% of the current global CO_2 emissions by 2035 (Birol, 2010). This technology will be an important step to reach the 2 °C goal of the Paris Agreement (Rogelj et al., 2016).

CCS is a method where carbon is captured at a point source (e.g., a power plant), transported to a suitable injection site (by e.g., pipelines, ships or trucks), and injected into a reservoir in the subsurface (e.g., saline aquifers or depleted hydrocarbon reservoirs) for permanent storage (Metz et al., 2005), as illustrated in Figure 1.1. Injection of CO_2 into the subsurface is a technology that has been utilized within the hydrocarbon industry since the 1980s to enhance oil recovery (Beliveau et al., 1993), and is therefore a well understood technology. The feasibility of CCS can best be understood by industry-scale projects such as the Sleipner Project (Torp and Gale, 2004), but also pilot-scale projects such as in Japan (Xue et al., 2006) and Ketzin in Germany (Forster et al., 2006) can confirm the possibility of storing the CO_2 subsurface.

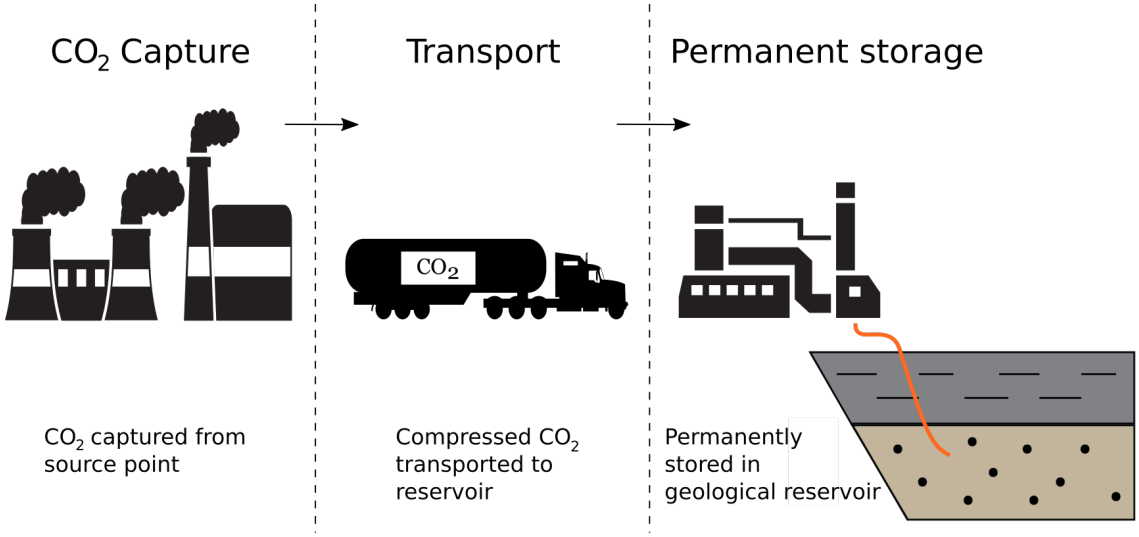

Figure 1.1: General concepts of CCS.

For storage of CO_2 to be feasible, parts of the conventional petroleum system needs to be in place, such as the storage formation, caprock and trap. Typical caprocks are low-permeability rocks such as shale or evaporites (e.g., Song and Zhang, 2013; Gale et al., 2014). In general, four different trapping mechanisms are recognized for CCS (Zhang and Song, 2014): (i) hydrodynamic trapping, (ii) residual trapping, (iii) solubility trapping, and iv) mineral trapping. Hydrodynamic trapping is regarded as the primary trapping mechanism, and refers to the CO_2 being trapped as a supercritical fluid or gas under a low-permeability caprock. This type of trap is dependent on a caprock with a capillary entry pressure higher than the buoyancy or hydrodynamic force that the CO_2 will act with. For this trapping mechanism, a structural or stratigraphic closure that provides both a lateral and vertical seal needs to be present. In addition, the caprock should possess properties such as low permeability and sufficient thickness. This type of trap can also be referred to as a structural, stratigraphic or hydrothermal trap. The residual trapping refers to CO_2 and brine having different densities, and hence the CO_2 will be trapped in the pore space, and will be immobile due to the brine surrounding it. The solubility trapping refers to the dissolution of the CO_2 in the fluids present at the injection site. Properties such as the salinity, temperature and pressure defines if the gas dissolves. The dissolution continues until an equilibrium is reached within the fluid. The mineral trapping refers to the injected CO_2 being incorporated into stable mineral phases already present. A reaction

with the minerals present or organic matter needs to happen for this type of trap to work (Zhang and Song, 2014).

The potential for caprocks to leak is a major concern for the CCS. There are three recognized leakage scenarios through caprocks (Busch et al., 2008): (i) mechanical failure leading to rapid leakage when the seal is breached, or by damage of well corrosion causing fracture networks, this is referred to as hydraulic seals; (ii) exceeding of capillary break-through pressure causing long term leakage; (iii) dissolved gas lost through water-saturated pore space, referred to as membrane seal.

Longyearbyen's power is sourced from from the local coal-fueled power plant. In 2007 a project (the Longyearbyen CO_2 Lab, Fig. 1.2) to capture and store the CO_2 emitted from this power plant was initiated to characterize the subsurface reservoir-caprock system (Braathen et al., 2012). This project is an onshore, pilot-scale site for geological CO_2-sequestration at depths between 700 meters and 1000 meters on central Spitsbergen, Svalbard (Ogata et al., 2014b). In this project the Upper Triassic-Lower Jurassic Wilhelmøya subgroup is the targeted storage succession, and the Upper Jurassic—Lower Cretaceous Janusfjellet Subgroup, consisting of the Agardhfjellet and Rurikfjellet formations, acts as the targeted caprock. On central Spitsbergen this subgroup is measured to be more than 400 m thick (Dypvik et al., 1991). The Agardhfjellet Formation is considered to be the lateral time-equivalent to the Barents Sea (the Fuglen and Hekkingen formations), North Sea (the Draupne Formation) and Norwegian Sea (the Spekk Formation) dark shales (Koevoets et al., 2018).

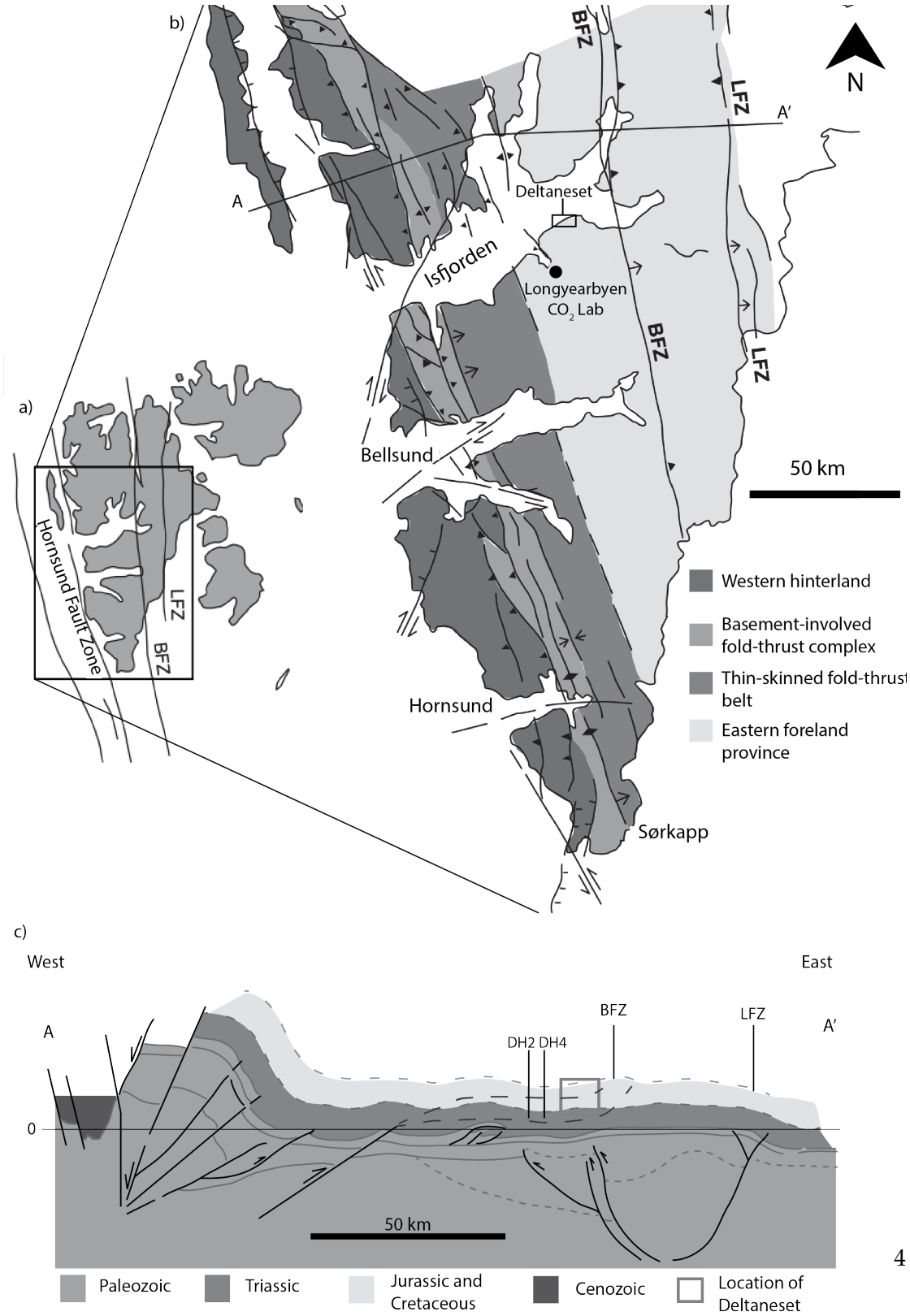

Figure 1.2: Location of the Longyearbyen CO_2 Lab and the field site. a) Outline of Svalbard, b) structural element map of southern part of Spitsbergen, and c) cross section of central Spitsbergen. Modified from Bergh et al. (1997) and Ogata et al. (2014b). BFZ - Billefjorden fault Zone, LFZ - Lomfjorden Fault Zone.

In 2010 several leak off tests (LOT) were conducted on the targeted reservoir and caprock succession, and the tests recorded vertical pressure differences, with pressure up to 30% below hydrostatic level in the lower targeted storage formation (Braathen et al., 2010). The LOTs combined with isotope analysis confirms that the seal is efficient (Huq et al., 2017; Braathen et al., 2012), at least on a thousand year time scale. Values of up to 50 bar has been recorded in the reservoir and lower caprock succession (Birchall et al., 2018). Flow capacity measurements (Braathen et al., 2010) confirmed a good storage formation, which is assumed to be due to natural existing fractures. A secondary seal is recognized within the permafrost currently present in the area (Braathen et al., 2012; Olaussen et al., 2019). Onshore pilot scale projects such as this contribute to an understanding of how CO_2 migrates, and can help to optimize the technology and monitior CO_2 migration (e.g., Lavadera et al., 2018).

The Longyearbyen CO_2 Lab has a CCS system that is considered unconventional. The typical trap is not present, as the succession is cropping out approximately 15 km north of the planned injection site (Bælum et al., 2012). In addition, a tight reservoir has been considered a challenge. Initially, the mean porosity is 13% and average permeability is 1.5 mD, but permeability values up to 39 mD has been measured (Senger et al., 2015; Mulrooney et al., 2019). Hence the system is considered to be good, due to the natural existing fractures resulting in the given, satisfying permeability measurements. The lateral extent of the caprock formation is assumed to be of great enough extent to make sure the injected fluids are trapped (Braathen et al., 2012). Still, further research need to be conducted to increase the understanding of the mechanical properties of the caprock.

1.2 Motivation

Studies focused on fracturing in shale-dominated units increased in the 1980s when exploration for shale gas in the US increased, and the importance of natural existing fractures within the shale was recognized (Gale et al., 2014). Still, there is a lot more to be studied about structural features within shale-dominated units. Shale, due to its fine grained nature, is not fully understood regarding its properties and composition (Aplin et al., 1999). Central Spitsbergen holds a unique opportunity to study shale-dominated successions due to the possibility of combining field and drill core data. An enhanced understanding of such a mechanically weak succession can therefore be acquired here. This knowledge is

valuable both for CO_2-sequestration, as well as in a petroleum exploration and production perspective. The data in this study is primarily acquired to enhance the understanding of the caprock properties of the Agardhfjellet and Rurikfjellet formations.

1.3 Aims and Objectives

The focus of this study is to conduct a structural analysis by looking at deformation structures and analysing the mineralogy of the Late Jurassic to Early Cretaceous succession herein defined to be the Agardhfjellet Formation (the upper Slottsmøya Member), and the Rurikfjellet Formation (the lower Wimanfjellet Member). This stratigraphic interval is cropping out at Deltaneset, in addition to being present in several drill cores from the Longyearbyen area, making it a unique study area for this shale-dominated succession. Field observations and drill core data, as well as XRD and SEM analyses, are used in this study. This provides an improved documentation of the cap rock properties of this interval as well as an increased understanding of the tectonic impact of the mechanically weak succession. The aims of this study are:

- Determine fracture abundance and origin of fractures within the studied succession, and relate it to tectonic events.
- Form a three-dimensional understanding of the extent of fracturing in the studied interval, by comparing outcrop and drill core data.
- Map the structural deformation present within the upper Agardhfjellet and lower Rurikfjellet formations, focusing on the décollement zone reported to be in this interval.
- Study the mineralogy of the aforementioned formations to see if there are any differences between the two formations, and how the mineralogy may be related to the deformation of the rock.

By combining the aims, the overall goal is to evaluate the caprock potential of the upper Agardhfjellet and lower Rurikfjellet formations.

Chapter 2

Theoretical background

2.1 Deformation in shale-dominated units

2.1.1 Fracture characteristics

Fractures are defined to be a discontinuity exhibiting a planar or sub-planar expression with one narrow dimension compared to the two other dimensions (Fossen, 2010). A fracture forms as a result of either external stress or internal stress, such as tectonic or thermal, respectively (Fossen, 2010). A defining property of fractures is the loss of cohesion. Fractures develop in rocks that are prone to brittle deformation, and can be described as structural heterogeneities. The role fractures play (as either a conduit or baffle) depends on parameters such as their size, distribution, strength, spatial arrangement, intersection and mode (Gale et al., 2014).

The fracture mode is an important parameter when predicting the fluid flow pathway within a rock (Fossen, 2010). Fractures can be divided into four primary modes, and are identified on the basis of how two masses move relative to each other (Fig. 2.1). The relative movement that causes a fracture to develop is a result of how forces have acted on the host rock (Fossen, 2010; Schultz and Fossen, 2008). The different fracture modes include:

Mode I: An extensional type of displacement recognized as opening of opposing walls, known as joints. These fractures develop perpendicular to the minimum stress axis. Joints can be either bed-confined, meaning restricted to one lithological bed, or through-going, meaning that it cuts through one or more sedimentary beds. If the

joints are sealed with mineral cement, they are referred to as veins.

Mode II: A shear fracture formed parallel to the slip direction.

Mode III: A shear fracture formed with rotational or tearing forces.

Mode IV: A compressional type of displacement recognized as a closing of two opposing walls, known as an anti-crack. These fractures form perpendicular to the maximum stress axis, and include features such as stylolites.

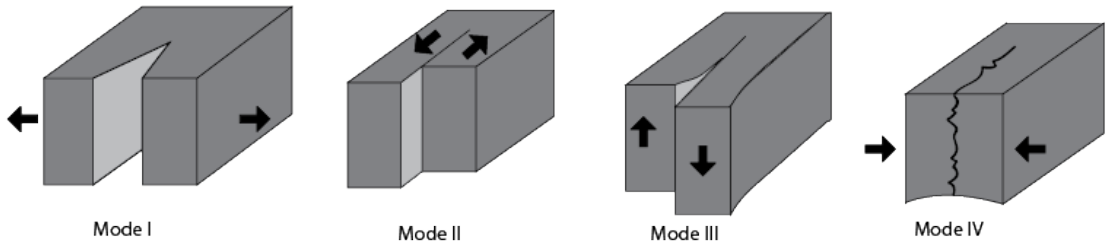

Figure 2.1: The different modes of fracturing. Arrows indicate movement of the opposing fracture walls. Modified from Fossen (2010).

Further, fractures can be arranged in sets based on similar attributes such as orientation (Hancock, 1985). Different sets makes up fracture patterns, and can be referred to as fracture networks. Within one set of fractures, a number of characteristics may differ. They can show a variety of height, length and aperture (Schultz and Fossen, 2002). Fracture networks are defined based on properties such as orientation, size, and connectivity of multiple fractures (Andersen et al., 2013). The fracture network indicates the connectivity within a rock mass in a given area, which can confirm fluid flow properties of the host medium.

The morphology of fractures observed in the field is described by Nelson (1985) and can be divided into four main types: (i) open fractures, (ii) deformed fractures exhibiting slickensides and filled with gouge, (iii) mineral-filled fractures, and (iv) vuggy fractures. The open fractures do not show any deformation and do not contain mineral cementation along the fracture planes. The deformed fractures are characterized by offset along

the fracture planes, with material derived from the fracture plane itself as gouge-fill. The surfaces with slickensides indicate syn-deformation of the fracture planes. The mineral filled fractures indicate that a secondary or diagenetic fracture has grown along the fracture plane. Vuggy fractures refer to dissolution of mineral cement when re-opening of the fracture has occurred (Nelson, 1985).

Fractures in outcrops provide insight into natural occurring fractures, and a possibility to study sub-seismic (less than 20 m displacement) features (Laubach et al., 2009). Outcrop studies provide data that can be used to understand fractures in the subsurface, by learning about fracture patterns that can be used to understand similar patterns at greater depths. However, multiple studies conducted throughout the last couple of decades reveal differences between fracture patterns found at depths exceeding 1 km and outcrops (e.g., Laubach et al., 2009). Impact from weathering, pressure-temperature paths and decompaction can have an affect on fracture patterns. Gale et al. (2014) report differences between fractures in the subsurface and in outcrops regarding appearance, with many sealed fractures in the subsurface and a dominance of joints in outcrops. Only a small number of mineral filled fractures are observed in the outcrops (results based on shale studies).

The mechanical properties of a rock affects the rocks' strength, ability to deform, and determine what structures may form within the rock mass (Bell, 1993; Kohlstedt et al., 1995; Crider and Peacock, 2004). The porosity of the rock is an important property, in addition to the resulting permeability the fractures can lead to (Wong et al., 1992; Fossen and Bale, 2007). Rock masses with low porosity tend to expand in volume during shearing, and often exhibit zones of concentrated shearing (Schultz and Fossen, 2008). The type of structural discontinuity that occurs depends on the porosity of the rock. High porosity rocks ($>$ 10% to 20%, e.g., sandstones) often form tabular discontinuities known as deformation bands, while joints and faults are not related to the porosity and can hence form in rocks with any porosity value (Schultz and Fossen, 2008). The chemical properties of the rock are also important, as it defines what chemical reactions may occur where the fracture is located. This refers to the way the fracture develops as well as the implications for fluid flow after the fracturing has occurred (Laubach et al., 2009).

2.1.2 Fractures in shale

The term shale refers to a rock with constituent particles such as quartz, feldspar, clay minerals, organic matter, pyrite, carbonates and phosphates (Gale et al., 2014). Studies on shale and fracturing within shale-dominated units have matured in the last years, due to the economical benefits of shale gas. For many years the importance of fractures as fluid-flow pathways has been studied within sandstone and other typical reservoir rocks due to their importance in petroleum exploration. With the increased necessity for knowledge about caprocks, studies of fracturing in shale have also increased. Shales act as the seal for almost all petroleum provinces as well as waste disposal sites (Aplin et al., 1999). Further, fractures within shale is a controlling factor when it comes to shale gas production (Gale et al., 2014).

Initially, shale will exhibit a ductile response to an increased load. But, when exposed to chemical diagenesis and build up of overpressure, a brittle response may occur (Nygård et al., 2006). Properties such as low porosity, small grain size and a high proportion of brittle minerals such as quartz and feldspar can correspond to greater strength within the shale (Nelson, 1985). In general, shales rich in clay minerals or organic matter often exhibit a low strength (Guo et al., 2013). Shale often has a low Young's modulus, and thereby typically exhibit a low fracture abundance and in some cases no fractures at all (Laubach et al., 2009). High clay fractions and organic material within shale often result in ductile deformation, whereas a high content of silica, feldspar and carbonates typically corresponds to more brittle behavior (Miller and Paterson, 1994). This corresponds to typical low brittleness index (BI) for clay-rich rocks (Guo et al., 2013). As such, brittle behaviour is more likely to be found in shale with a high content of brittle minerals. However, rocks that have been exposed to catagenesis exhibit fracture growth when a high organic content is present (e.g. Rodrigues et al., 2009). High organic content in shale tends to correspond to shear and tensile fracturing (Sone et al., 2011).

Filling of veins is dependent on the host rocks ability to provide reactants by local dissolution and diffusion (Gale et al., 2014). This partly depends on burial and subsequent heating of the strata. Within fractures in shale, calcite filling is mainly found (Gale et al., 2014). The sealing properties of the sealed fractures depends on the chemical composition of the filling as well as the mineralogy of the host rock (Gale et al., 2014). For a fracture to work as a baffle to fluid flow, it needs to contain minerals with good sealing properties.

Fractures in shale can be hard to distinguish from other, natural discontinuities. Bedding-

parallel fractures can be hard to separate from bedding. The nature of shale is anisotropic, which typically gives unclear results. In addition, weathering may impact the recording of the bedding-parallel fractures and lead to an underestimation of these types of fractures in the field (Gale et al., 2014). Bedding-parallel fractures have been linked with catagenesis where they are most abundant (e.g. Cobbold and Rodrigues, 2007).

By mapping patterns of fractures, which may be linked to the shale composition, burial history and stratigraphy, the understanding of the fracture mechanisms can be increased. As a result of this, the response of natural fractures to external forces can be predicted (Smart et al., 2014).

2.1.3 Theory of faulting

Faults are defined as planar or zonal structures, where shear displacement occurs across the structure (Billings, 1972). Faults can be broadly categorized as three types, and are illustrated in Figure 2.2 (Anderson, 1905): reverse faults or thrust planes, normal faults, and strike-slip faults.

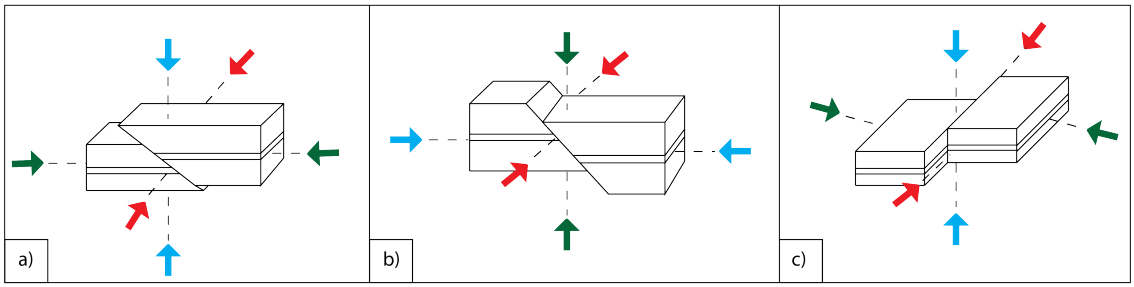

Figure 2.2: The Andersonian fault classification showing the causal stress orientation for each fault type. The green arrows indicates σ_1, the red arrows indicate σ_2 and the blue arrows indicates σ_3. a) reverse fault/thrust plane, b) normal fault, c) strike-slip fault.

The reverse or thrust faults are defined by the maximum principal stress (σ_1) being horizontal and the lowest stress (σ_3) being vertical (Anderson, 1905). Faults with a reverse movement can be recognized as either reverse faults or thrust faults, where reverse faults are steeply-dipping ($> 30°$), and thrust faults are typically low-angle ($< 30°$). Fundamental to these faults, the hanging wall is displaced upwards relative to the footwall (Peacock et al., 2016), and hence older strata is on top of younger strata. Normal faults occur when σ_1 is vertical and σ_3 is horizontal (Anderson, 1905). As a result of this stress

orientation, the hanging wall is displaced downwards in relation to the footwall (Peacock et al., 2016). Strike-slip faults are formed when σ_1 and σ_3 are both horizontal and oriented 90° to each other (Anderson, 1905). Displacement is in the horizontal plane, and will be parallel with the orientation of the fault (Peacock et al., 2016).

The fault architecture consists of a fault core and a damage zone. The fault core is also called the slip surface, and can either be a single surface or a zone of several slip surfaces. In soft, sedimentary rocks such as shale, the core typically consists of non-cohesive smeared out material. When a fault forms in a sedimentary rock, the clay and silt can be smeared out to a continuous membrane. The damage zone is characterized by brittle deformation of the wall-rock. Typical for this zone is shear fractures and tensile fractures (Fossen, 2016).

2.2 Relevant structural terms

Important structural terms referred to in this thesis are explained shortly. These structures are typical for fold-and-thrust-belts (Fossen, 2016).

Horse: This structure occur between the thrust faults that form duplex structures, where they are arranged piggy-back and typically dip towards the hinterland. Horses are recognized as an S-shape in the vertical profile. (Fossen, 2016).

Décollement: A sub-horizontal detachment zone acting as a level of shearing, where the overlying strata is detached from the lower lying strata (Cook and Varsek, 1994; Ogata et al., 2014a). Shale as a mechanically weak rock often accumulates strain along these zones, where the driving force is the hydrostatic pressure gradient. In fold-thrust-belts, shale often accomodates concentrated deformation and slip (Gale et al., 2014).

Duplex: A fold-and-thrust-belt structure, bound by a roof thrust above, and a floor thrust below. This structure is characterized by multiple, linked contractional faults internally (Cook and Varsek, 1994). Duplexes form as a mechanism for transfer of slip from one horizon to a shallower one (Boyer and Elliott, 1982). The slip decreases along the floor thrust and increases along the roof thrust. The geometry of the horses control the shape of the duplex (Butler, 1982).

Pop-up structure: A structure consisting of two thrust faults with opposing orientation, where one is foreland vergent and the other one is hinterland vergent. The strata in between the two thrusts are uplifted by the reverse movement (McClay, 1992). This is a thrust structure often found in the foredeep, the frontal and weakly deformed part of a fold-and-thrust belt. It is commonly formed where the basal friction is low.

Chapter 3

Geological setting

Spitsbergen is the largest island of the Svalbard archipelago and hosts a consistent rock succession ranging in age from the Precambrian to Tertiary age (Dallmann et al., 2015). In this thesis, parts of the Late Bathonian to Hauterivian sedimentary rock succession previously known as the Janusfjellet Formation (Dypvik et al., 1991) has been studied. This formation is now defined as a subgroup, comprising the Agardhfjellet and Rurikfjellet formations. The main focus of this chapter will therefore be on the geological evolution of the archipelago from which time these formations were deposited.

3.1 Tectono-stratigraphic evolution

3.1.1 Geographic location

The archipelago of Svalbard is today located at the northwestern edge of the Barents Sea, between 71° and 84° north, and 10° and 35° east. The archipelago is bound by a steep, passive continental margin in the north (Faleide et al., 1984), whereas towards the west, Spitsbergen is bounded by a transverse spreading ridge (Bergh et al., 1997). Svalbard represents an uplifted part of the Barents shelf, where the outcropping stratigraphy is analogous to subsurface Barents Sea geology. Svalbard has therefore been a key study area to understand the subsurface geology of the Barents Sea for a long time, and has often been used to conduct correlation studies of the two areas (e.g., Nøttvedt et al., 1993).

3.1.2 Depositional environment and lithostratigraphy

Svalbard was located in the southern hemisphere during the Precambrian, but has slowly drifted northwards to its current location (Dallmann et al., 2015). During the intervening time, the archipelago has experienced several tectonic phases and eustatic sea-level variation. The development of the area where Svalbard is located has been dominated by N—S trending structures that initially formed during the Caledonian orogeny in the Silurian-Devonian, and lineaments related to this event (McKerrow et al., 2000).

In the Early Jurassic, most of the Earth went through a shift from an arid or semi-arid to a more humid climate. Globally, this was a tectonically active period, with major reorganization of the continental plates. As a result, there were numerous sea-level changes, with flooding of large landmasses as well as an exposure of shelf areas and the formation of internal basin highs occurred (Dallmann et al., 2015). By the end of the Jurassic, the break-up of the supercontinent Pangaea was completed, resulting in the Gondwana and Laurasia supercontinents in the southern and northern hemispheres, respectively. At this time, Svalbard was located at approximately 60° N (Fig. 3.1).

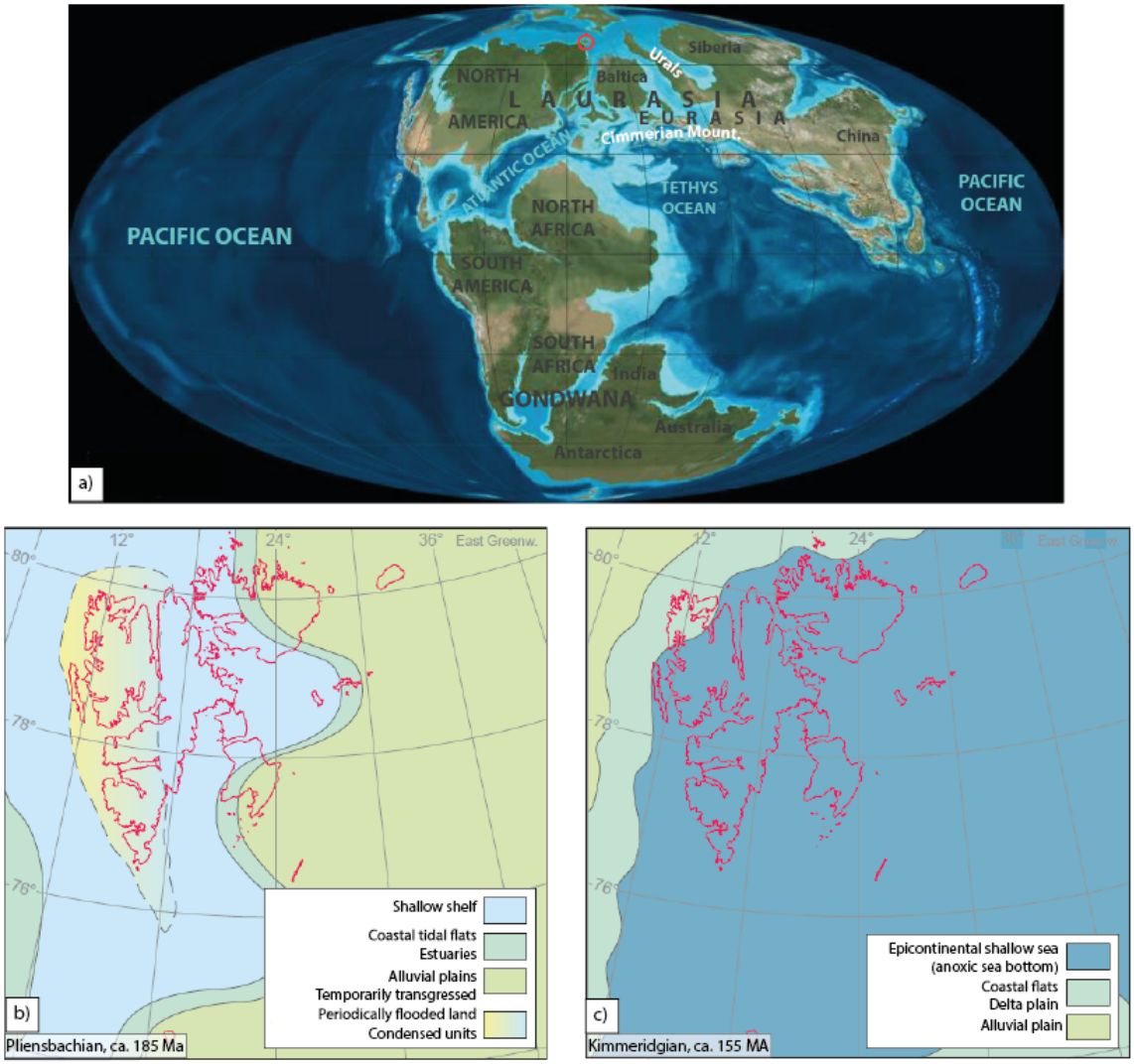

Figure 3.1: a) Svalbard's position (marked as a red circle) during the Jurassic, Svalbard's depositional environment during b) Pliensbachian, and c) Kimmeridgian. Obtained from Dallmann et al. (2015)

In the mid-Jurassic, Svalbard was situated on a shallow-shelf to marginal marine platform. During this time, the deposition of the Wilhelmøya Subgroup occurred (Dypvik et al., 1991). In the Late Jurassic, the sea level rose, and large parts of Europe and North America became flooded. This created epicontinental seas and separated landmasses. Atmospheric concentration of CO_2 was high at this time, which enabled high production

and preservation of organic matter. The Upper Jurassic shale-dominated units comprise many of the oil and gas provinces that are in production worldwide today (Dallmann et al., 2015).

The Agardhfjellet Formation comprise four members: Oppdalen, Lardyfjellet, Oppdalssåta, and Slottsmøya (Dallmann, 1999). The formation was deposited during a transgressive event in the Bathonian, and is interpreted as open marine shelf deposits (Fig. 3.1, Dypvik et al., 1991). The Brentskardhaugen Bed, a coarse sandstone bed, defines the lower boundary of the formation. After this unit, a highly bioturbated siltstone follows, before continuous dark shale (with some interbedded siltstone and carbonates) makes up for the rest of the formation (Dypvik et al., 1991). During the time of deposition, the environment was oxygen deficient. The time-equivalent Hekkingen Formation in the Barents Sea is a prolific source rock (Worsley, 2008).

A 200 m thickness variation within the formation is observed, with an observed thickness of 250 m to the west and 50 m to the east of Spistbergen (Dallmann et al., 2015). This variation is interpreted to be related to erosion in the east prior to deposition of the overlying strata. In addition, post-depositional tectonic events such as the Cenozoic transpressional event has resulted in folding and faulting of the strata which caused repetition of the formation (Major et al., 2000).

The boundary between the Agardhfjellet and Rurikfjellet formations is defined by a condensed section and a major unconformity, the base Cretaceous unconformity (BCU) (e.g., Grundvåg et al., 2019). During the time of deposition of the Rurikfjellet Formation, Svalbard was located at 65° N (Fig. 3.2).

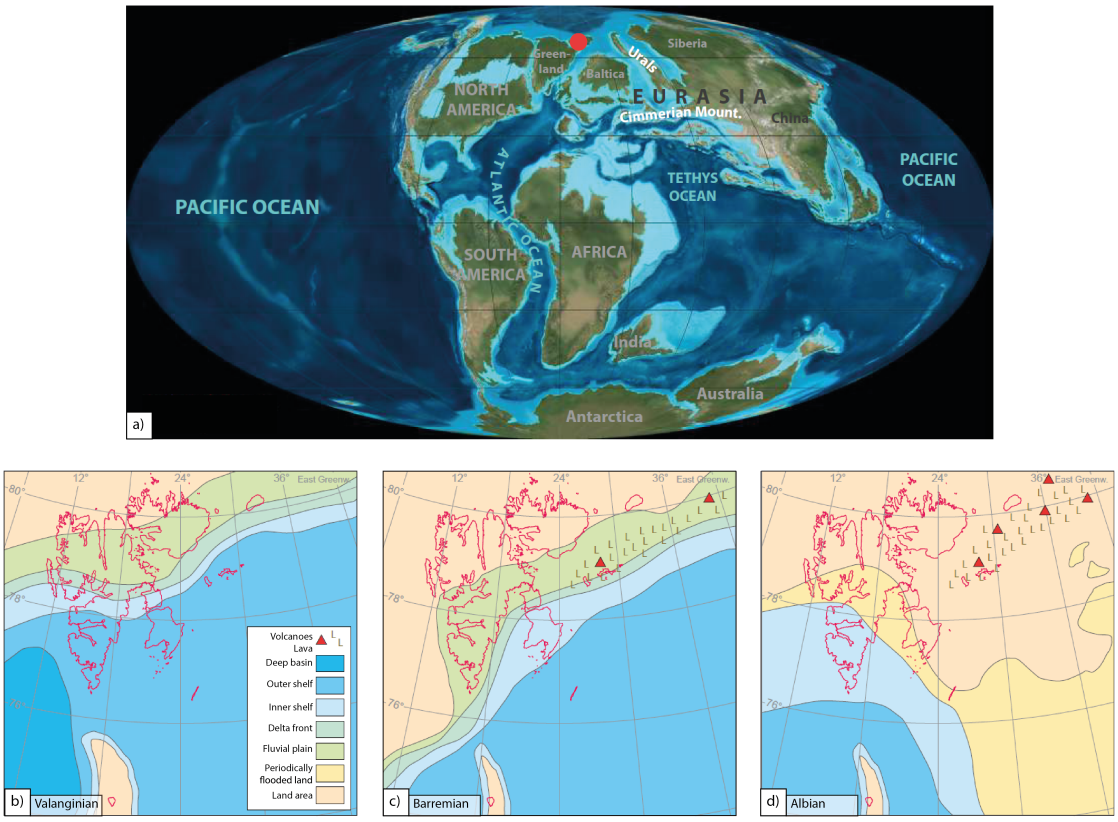

Figure 3.2: a) Geographic position of Svalbard (marked as a red circle) during the Cretaceous, Svalbard's depositional environment during b) Valanginian, c) Barremian, and d) Albian. Obtained from Dallmann et al. (2015)

The base of the Rurikfjellet Formation is defined by the Myklagardfjellet Bed, which is an up to 10 m-thick reddish-yellow or green plastic clay (Dallmann, 1999). The boundary between the two formations is not easily recognized in the field as it is often highly weathered. In addition, it is poorly developed in some areas making it hard to distinguish between the shale-rich upper member of the Agardhfjellet Formation and lower member of the Rurikfjellet Formation (Dallmann et al., 2015).

The Rurikfjellet Formation consists of two members, the Wimanfjellet and Ullaberget members (Dallmann, 1999). Due to the break-up of the landmasses during Cretaceous, igneous activity led to heat flux within the oceans resulting in an increase in the volume of water, where the sea-level was approximately 100 m to 200 m above current levels (Dall-

mann et al., 2015). The Rurikfjellet Formation shows a regressive depositional sequence, as demonstrated by the formation showing an upward coarsening trend. The Wimanfjellet Member is a shale-dominated unit (Midtkandal et al., 2018), and is interpreted to have been deposited in an outer shelf environment during Valanginian–Early Hauterivian times (Grundvåg et al., 2019) in northern latitudes (Fig. 3.2). The Kikutodden Member is rich in silt- and sandstones and reflects the further shallowing of the sea level (Dallmann et al., 2015).

The coarsening upwards succession is overlapped by the Helvetiafjellet Formation. A northwestern provenance has been observed in this overlying formation, indicating that the sedimentary source changed towards the northwest during the Cretaceous (Midtkandal and Nystuen, 2009).

Based on geochemical analyses, the Janusfjellet Subgroup of Svalbard and the Hekkingen Formation of the Barents Sea (Fig. 3.3) show similar sedimentological conditions (Dypvik and Harris, 2001). This indicate similar provenance for the two areas.

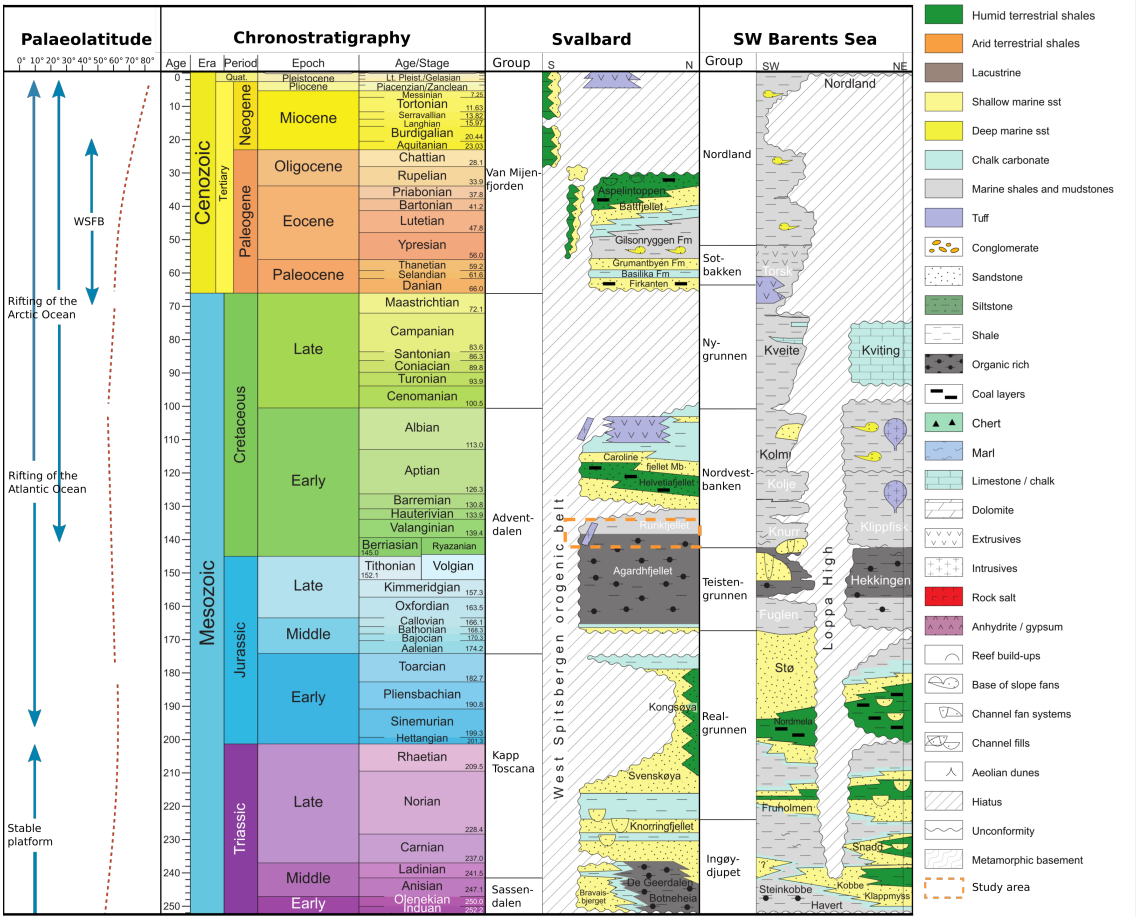

Figure 3.3: Lithostratigraphic table, correlating Svalbard and Barents Sea lithostratigraphy. Modified from Geological Time Scale Foundation (2016) and Dallmann et al. (2015).

3.1.3 Tectonic events

Svalbard has gone through several tectonic phases during the tectonic evolution of the area. The Spitsbergen subsurface is dominated by multiple structural lineaments with N—S and NNW—SSE trends. The most prominent fault zones reflected by these lineaments are the Billefjorden Fault Zone, the Lomfjorden Fault Zone and the Hornsund Fault Zone (Andresen et al., 1992). These fault zones are interpreted to have their origin in the Devonian, and have gone through numerous of reactivations during subsequent tectonic

events (Steel and Worsley, 1984). In general, the tectonic events have controlled the sedimentation of the strata (Dallmann, 1999; Steel and Worsley, 1984), as demonstrated by erosional surfaces, change in depositional patterns, non-depositional episodes, and different transport directions.

During the late Permian to Early Carboniferous there was a minor instability after the formation of the Caledonian Orogeny. The lineaments present caused a division between the highs in the west and the lows in the east, acting as a determining factor for deposition at that time by causing relief that influenced the drainage pattern. Svalbard was a stable, marine platform by the Late Carboniferous (Steel and Worsley, 1984).

During the Jurassic, the splitting up of Pangaea was complete (Dallmann et al., 2015). The platform cover (i.e. the Mesozoic succession) was highly impacted by the opening of the Amerasian basin in the Early Cretaceous (Dörr et al., 2013). The opening of this basin resulted in volcanic activity, leading to the development of the High Arctic Large Igneous Province (HALIP) in the Arctic region (Tarduno et al., 1998a,b) during Barremian to Early Campian (Senger et al., 2014). The sedimentary succession present at that time was intruded by the Diabasodden Suite dolorites. In addition, the northern parts of Spitsbergen was uplifted due to the heat flux associated with the magmatic activity which initiated further north (Maher et al., 2001; Nejbert et al., 2011). More than 1 km of the sedimentary succession on northern Spitsbergen was eroded as a result of this, and a major hiatus of the Late Cretaceous stratigraphic succession was formed (Dallmann, 1999; Dörr et al., 2013). Svalbard experienced a total of 3 km uplift due to the HALIP activity (Harland, 1997). As a result of the uplift late Cretaceous strata is not present at Svalbard, and a 3° regional, southwestward dip is persistent in Svalbard's strata (Bælum et al., 2012).

The intrusions from the HALIP are mainly found in the Triassic successions, but in some localities e.g., Botneheia and the east coast of Spitsbergen, the Agardhfjellet Formation has been cut into by dykes and sills respectively. Igneous intrusions also demonstrate NW—SE and NE—SW trends, suggesting that these were the main stress fields during the emplacement of the intrusions (Senger et al., 2013).

In the Paleogene, the opening of the Atlantic Ocean continued, but was punctuated by a phase of dextral transpression between Svalbard and Greenland (Braathen et al., 1999; Dallmann, 1999). This movement led to a fold-and-thrust-belt on the western side of Spitsbergen, called the West Spitsbergen fold-and-thrust belt (WSFTB). The WSFTB is characterized by a western thick-skinned province where structures are basement involved, and an eastern thin-skinned province with three different levels of décollement

zones, along weak evaporite and shale intervals. Two of these décollement zones bound the Longyearbyen CO_2 reservoir (Bergh et al., 1997; Braathen et al., 1999; Blinova et al., 2013).

The WSFTB developed during five different stages, as recognized by Bergh et al. (1997): (stage 1) an early development of shortening, and an establishment of décollements in the Carboniferous and Permian strata; (stage 2) a main shortening event associated with the formation of the dominant north-northwest-trending fold and thrust belt; (stage 3) a modification of the thrusts from stage 2 displayed as both monoclinal uplift and observed folding of décollements in the eastern zone; (stage 4) out-of-sequence thrust and truncation of earlier thrusts; (stage 5) extensional features forming in the east.

During this event, a foreland basin referred to as the Central Tertiary Basin (CTB), formed on the eastern side of the WSFTB (Steel and Worsley, 1984). Longyearbyen is located in the middle of this basin. Within the CTB, the section which this thesis focuses on was overlain by a 3 km overburden (Marshall et al., 2015b), causing mechanical and chemical compaction of the strata present (Bergh and Andresen, 1990; Braathen et al., 1999). The Mesozoic strata can be found along the NNW—SSE trending basin boundary in central Spitsbergen today.

The Paleocene-Eocene stage of the WSFTB generated thrust sheets transported eastward along weak intervals such as evaporites and shales, where décollement zones were localized (Bergh et al., 1997). The shale-dominated Upper Jurassic-Lower Cretaceous succession is interpreted to contain one of these detachment levels (Bergh and Andresen, 1990).

Svalbard has gone through several phases of deglaciation causing isostatic rebound and decompaction. In the Cenozoic, erosion and especially glacial erosion was an active process. This has led to approximately 3.5 km of uplift in central Spitsbergen (Henriksen et al., 2011; Bohloli et al., 2014). The underpressure within the reservoir of the Longyearbyen CO_2 Lab is associated with this mechanism. The strata present shows loading mechanisms, and later the unloading and erosion of the overburden displayed as unloading joints, probably reactivated during the deglaciation and decompaction (Ogata et al., 2014b).

3.1.4 The Agardhfjellet and Rurikfjellet formations

The focus of this study is on the Janusfjellet Subgroup, and in particular on the Slottsmøya Member of the upper Agardhfjellet Formation and the Wimanfjellet Member of the lower Rurikfjellet Formation. This subgroup comprise a 450 m thick, shale-dominated succession (Dypvik et al., 1991) acting as the targeted caprock and top seal for the Longyearbyen CO_2 Lab (Braathen et al., 2012; Olaussen et al., 2019).

The Agardhfjellet Formation is present at central Spitsbergen, and has been the focus of previous studies (e.g., Dypvik et al., 1991). This formation has an upwards increase of total organic content (TOC) to about 12% before it drops to 1.5%–2% at the top of the formation (Dypvik, 1984; Koevoets et al., 2018). The thickness variations within the Agardhfjellet Formation, ranging from 50 to 250 m, is due to the tectonic thinning of the formation as a result of the thin-skinned thrusting and sub-vertical fault movement from the Cenozoic transpressional event (Major et al., 2000). As a result of the mechanical properties of the shale, the Agardhfjellet Formation is rarely undisturbed. The combination of different structural discontinuities (e.g., imbricate structures and faults) has resulted in an alteration of the original thickness, hence it has not been preserved (Ohm et al., 2020). A western/northwestern provenance is interpreted for the formation (Koevoets et al., 2018).

The Myklegardfjellet Bed, which is the lower unit of the Rurikfjellet Formation, is defining the boundary to the underlying Agardhfjellet Formation (Fig. 3.4). This is a soft plastic clay, which easily weathers (Major et al., 2000; Grundvåg et al., 2019). The Wimanfjellet Member of the Rurikfjellet Formation consists of shales and mudstones. The boundary to the overlying Kikutodden Member is defined by the first occurring sandstone bed, and after this the formation becomes more sandy (Grundvåg et al., 2019). The Wimanfjellet Member is deposited in an open marine shelf, below storm wave base (Grundvåg et al., 2019). The coarsening upwards trend of the formation indicate a regressive environment. The formation has a significant lateral extent, with a continuous thickness making it a part of the top seal for the underlying Triassic to Middle Jurassic reservoir unit for geologic CO_2 storage (Braathen et al., 2012). A northwestern provenance has been indicated by previous palaegeographic reconstructions for the Rurikfjellet Formation (Grundvåg et al., 2019, and references therein). The Rurikfjellet Formation has a constant TOC value of 0.5% to 2%, indicating that the oxygen level was higher during the deposition of this formation (Dypvik, 1984) than for the Agardhfjellet Formation.

Porosity measurements has been conducted on samples from the Janusfjellet Sub-

group, revealing a low porosity of approximately 2% to 3% (Alemu et al., 2011). The mineralogy has been characterized as a typical shale composition, with clay minerals such as illite, smectite, chlorite and kaolinite. Other minerals such as quartz, feldspar, siderite, dolomite and pyrite have also been observed (Dypvik et al., 1991) within this subgroup.

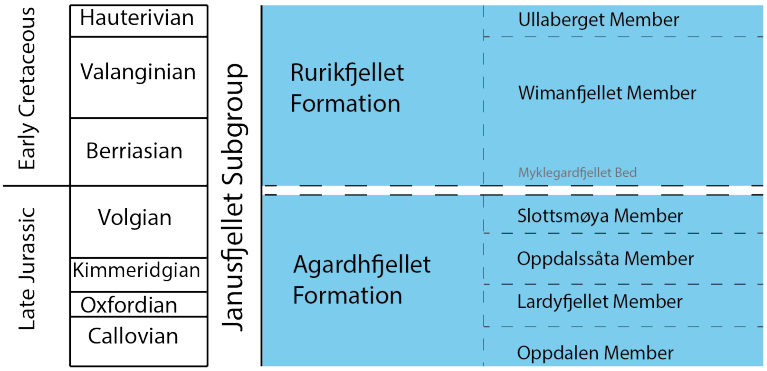

Figure 3.4: Stratigraphic chart for Janusfjellet Subgroup. White area between the dashed lines illustrate BCU. Modified from Dallmann (1999).

Chapter 4

Data and Methods

This chapter outlines the data sets and methods used in the study, summarized in Table 4.1. Structural field data have been integrated with structural data collected from drill cores. In addition, Scanning Electron Microscope (SEM) and X-ray diffraction (XRD) analyses were performed using two samples from DH4 at depths of 383 m (Rurikfjellet Formation) and 427 m (Agardhfjellet Formation).

Table 4.1: The multidisciplinary approach to the objectives of this study.

Method	Analyses	Aims	Data sets	Resolution	Key references
Fracture analysis	Structural logging of cores	Determine abundance, frequency, and physical characteristics of fractures	132 m of drill core	< 1 cm	Ogata et al. (2014b) Braathen et al. (2010)
	Line-intersection method, outcrops	Determine lithology dependence, abundance, and frequency of fractures	5 scanlines with 369 measured fractures	< 1 cm	Ogata et al. (2014a) Mulrooney et al. (2019)
Fault analysis	Structural measurements	Determine stress regime that has affected the study area	Structural measurements of strike and dip in the field	1 – 10 cm	Bergh et al. (1997) Ogata et al. (2014a)
Mineralogical analysis	XRD	Determine mineralogical composition	2 samples from DH4 at depths 427 m and 383 m	1 cm	Dypvik (1984) Grundvåg et al. (2019) Koevoets et al. (2018)
	Bulk analysis	Determine whole rock composition			
	Clay analysis	Determine clay mineral composition			
Petrographical analysis	SEM	Determine surface mineralogy and distribution of minerals within the samples	2 samples from DH4 at depths 427 m and 383 m	1 µm	Reed (2005)

4.1 Study area

All data used in this study were collected from central Spitsbergen, Svalbard. The positions of which are summarized in Figure 4.1.

The drill cores were collected as part of the Longyearbyen CO_2 Lab between 2007 and 2012 (Braathen et al., 2012; Olaussen et al., 2019). The two drill cores used in this study are DH2 from approximately 3 km northwest of Longyearbyen, and DH4 from Adventdalen approximately 4 km southeast of Longyearbyen. The drill cores have a diameter of 78 mm, where the combined length of the studied cores were 132 m. The gathering of data from the drill cores took place during February 2019. The structural data collected from the cores have been linked with the sedimentary logs made by Koevoets et al. (2018) and Grundvåg et al. (2019), where Koevoets et al. (2018) log from DH5 has been used as a proxy for DH4. This is because DH5 is located only 90 m away from DH4, and it is therefore assumed that the sedimentology is fairly similar. Simplified logs were made based on the previous publications in combination with observations done during the structural logging.

Unique to this study is new field data collected from Deltaneset during field campaigns in the summer of 2018 and 2019, where the succession studied in the drill cores crops out 15 km north of Longyearbyen (Fig. 4.1). The first field campaign was conducted over a period of 4 days in 2018 and involved reconnaissance mapping and initial outcrop photograph acquisition. The second field campaign was conducted during a period of 10 days, when most of the data gathering was conducted. The different localities examined in the field were chosen based on where the best exposures of the structures aimed to study were. The two main localities, shown in Figure 4.2, outlines where the scanlines were produced and other structural deformational features were observed. The succession outcrops in the lower part of Janusfjellet, where the specific areas were located in the upper Konusdalen West and 200 m to the east of this.

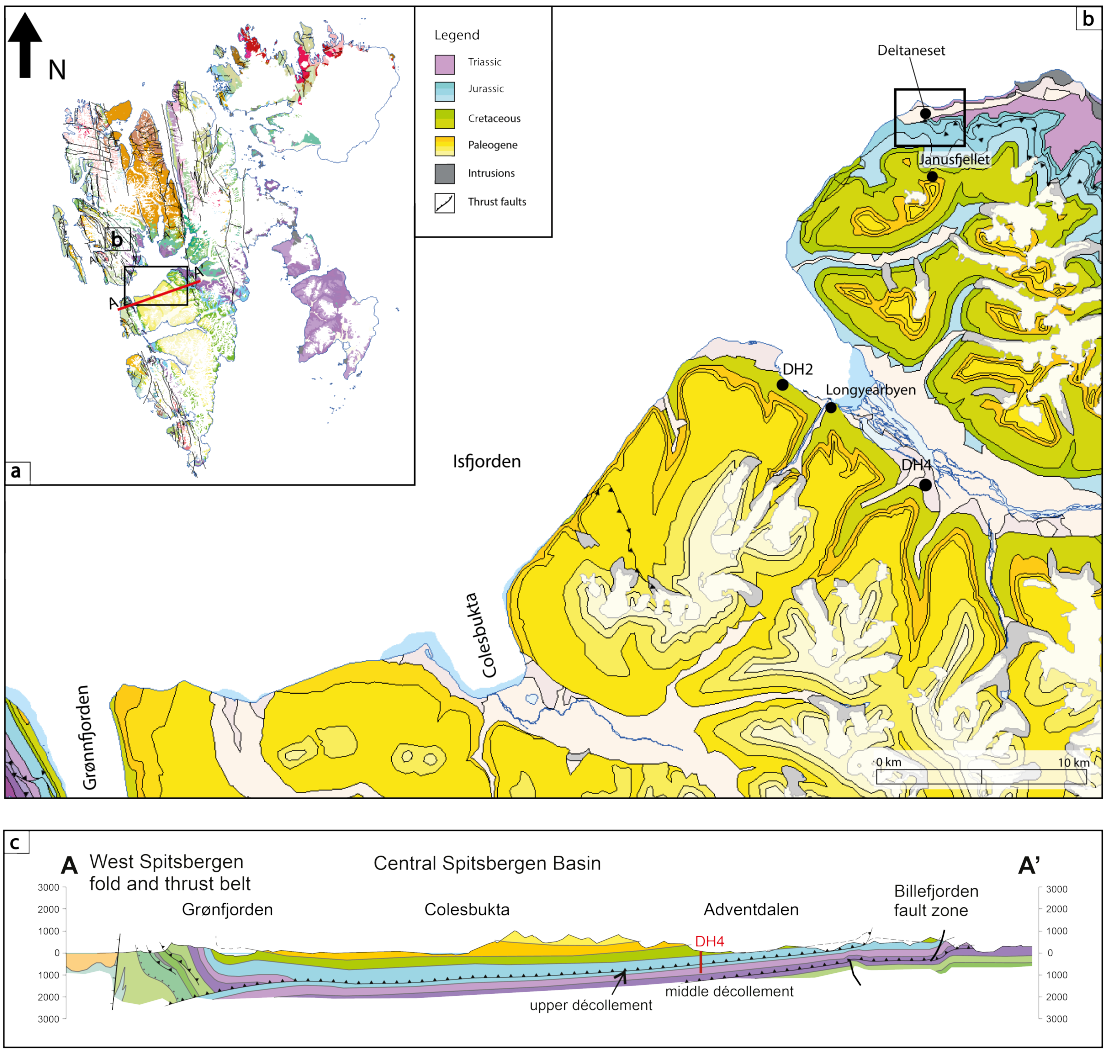

Figure 4.1: a) Geological map of Svalbard, b) close up of the central parts of Spitsbergen, where study areas are marked, c) cross section of central Spitsbergen highlighting the CTB. Modified from Norwegian Polar Institute (2012) and Dallmann et al. (2015).

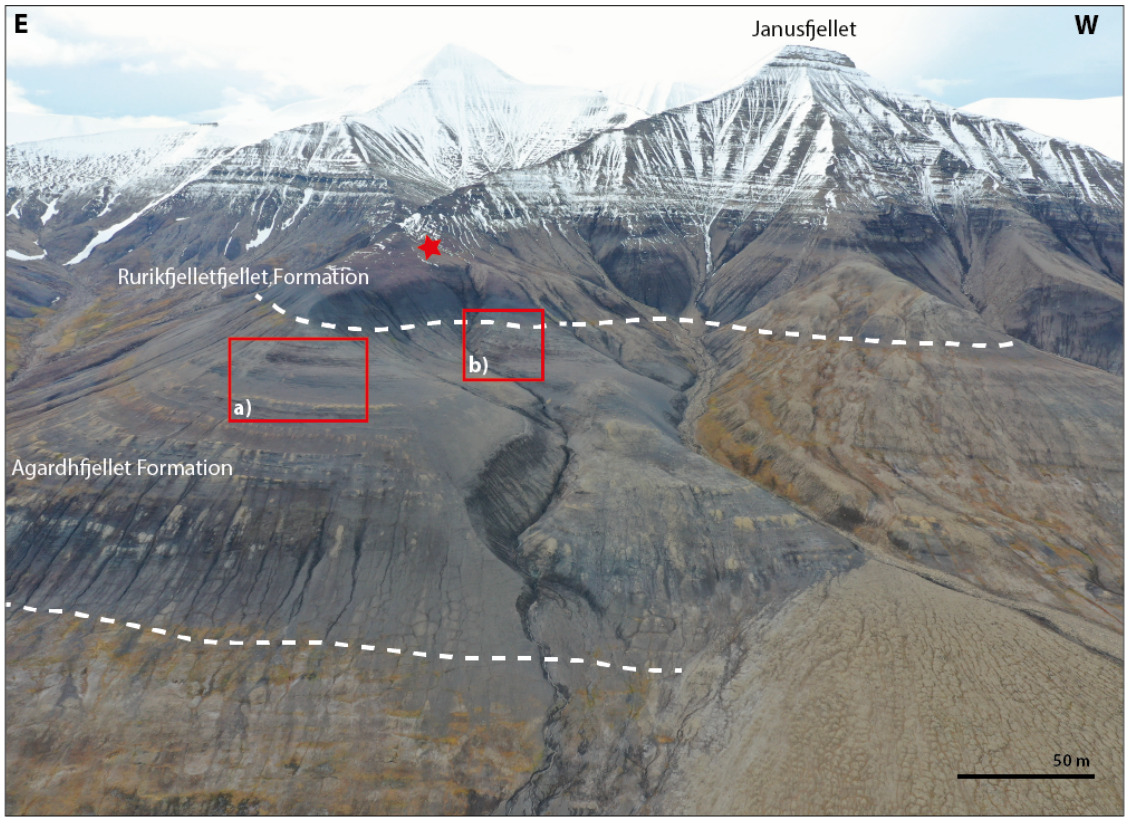

Figure 4.2: Field sites seen from the northeast. a) East of Konusdalen West, where a meso-scale thrust structure was mapped, b) Konusdalen West where scanlines were produced and a meso-scale thrust fault structure was mapped. Star indicates area where observed fault propagation fold was located. Janusfjellet is approximately 800 m.

4.2 Field data

Scanlines (i.e. the 1-D line-intersection method, after Singhal and Gupta (2010)), were produced in different stratigraphic intervals to provide lateral fracture frequency plots. The different stratigraphic intervals represent different lithologies, and were aimed at to see if there was any lithology dependence related to the fracturing. Frequency is used to address the abundance of fractures of a given size per unit of rock, and is illustrated by the scanline length (Gale et al., 2014). Fracture orientations were measured perpendicular to the bedding, and according to the right hand rule, using a geological compass. Five

scanlines were produced with a total of 369 fractures measured, with a $\sim$1 cm resolution.

The fractures were defined based on their mode of fracturing. Further, a description of the fractures after Singhal and Gupta (2010) was conducted, and includ recordings of the following characteristics:

- Orientation (i.e., strike and dip).
- Stratigraphic position (mid-point depth of the cores).
- Spacing and frequency (i.e., vertical in cores and horizontal in outcrops).
- Surface asperity (i.e., character of roughness/smoothness of the fracture walls).
- Coating and in-fillings (if observed).

In addition to producing scanlines, structural mapping of thrust faults and large through-going discontinuities was conducted in order to form a comprehensive understanding of the stress regime that has affected the area. Furthermore, simplified sedimentary logs were constructed to correlate the intervals studied in the field with the intervals mapped in the cores. The different lithological units were defined based on grain size, lithological composition, bedding thickness, sedimentary structure and fresh surface color.

4.3 Borehole data

Detailed structural logging was conducted on the intervals between depths at 450 m and 510 m in DH2 and depths between 380 m and 452 m in DH4 in order to determine the abundance and the frequency of the fractures. Primarily a distinction between open and closed discontinuities was recorded. The fracture characteristics were described using the characteristics listed in Section 4.2. In addition, a distinction between natural and drilling induced fractures were made based on the appearance of the fractures, such as freshness, how well the opposing walls matched and the presence of slickensides. The studied interval of drill cores were chosen based on previous descriptions of where the décollement zone is present within the drill cores (Braathen et al., 2012). The boundary between the two formations are based on Braathen et al. (2012) and Koevoets et al. (2018).

The drill cores were not oriented, hence only the dip angle could be measured.

The optical televiewer data presented in Braathen et al. (2012) and Ogata et al. (2014b) has been used to compare fracture frequencies observed in the drill cores.

4.3.1 Processing of fracture data

Microsoft Excel (2016) was used to construct bar charts illustrating fracture frequencies along vertical transects of the cores, and to determine which dip angles that were most abundant.

The cores and outcrop data sets were analyzed together to create a quasi three dimensional understanding of the fracture network within the succession. The cores give a good overview of the distribution vertically within the succession, while the data from the field give an understanding of the lateral distribution of the discontinuities present.

The processing and visualization of the field data were conducted using Excel and Stereonet 10 (Allmendinger et al., 2011). In Excel, column charts were made to illustrate the observed lateral frequencies, while Stereonet 10 was used to identify and exhibit fracture sets.

4.4 Mineralogical analysis

Mineralogical and petrographical analyses were conducted on intervals from DH4, at depths of 383 m and 427 m (Fig. 4.3). These intervals were chosen based on the observed presence of fractures within the cores, aiming to see if there was any difference regarding mineralogy above and below the most deformed sections, and if there were any compositional differences between the Agardhfjellet and Rurikfjellet formations. The uppermost sample (at 383 m depth, further referred to as S383) is from the Rurikfjellet Formation and the lowermost sample (at 427 m depth, further referred to as S427) is from the Agardhfjellet Formation (Koevoets et al., 2018; Grundvåg et al., 2019). The use of cores to conduct these analyses is ideal, since they are not impacted by weathering. The fracture surfaces in both samples show similar characteristics, both being polished with slickensides. The results of the analyses is therefore primarily applicable to fractures exhibiting these characteristics.

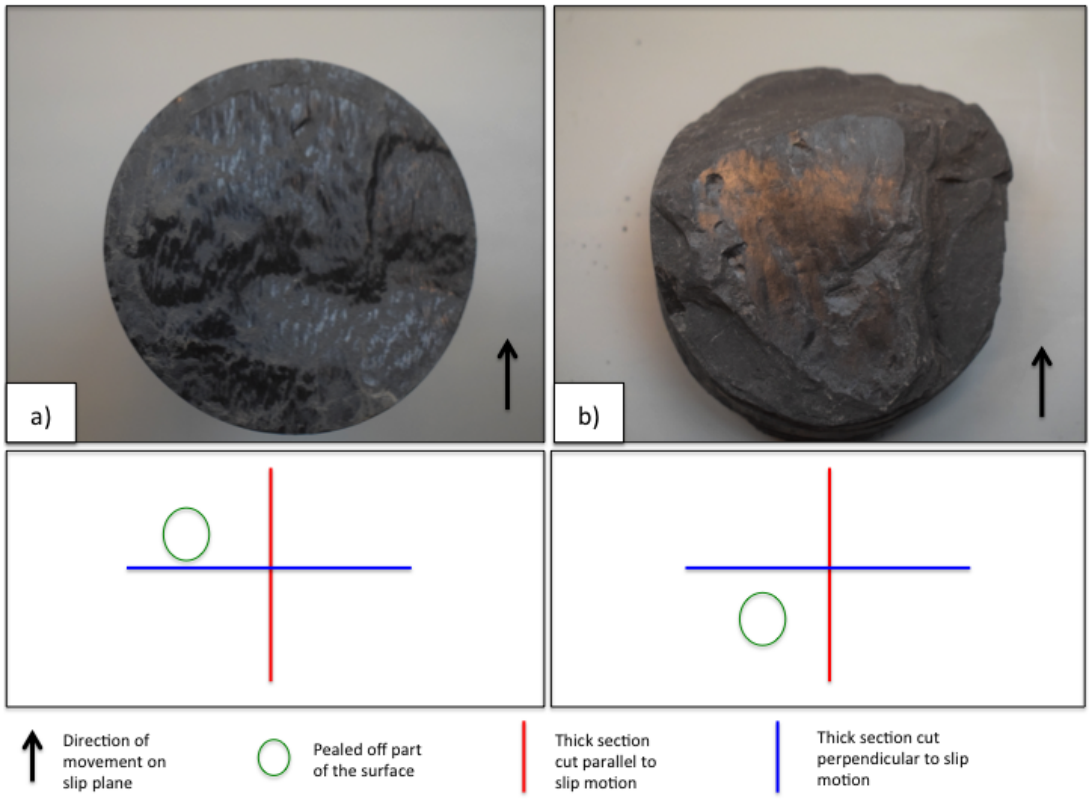

Figure 4.3: The samples from DH4 used to conduct the mineralogical and petrographical analyses. a) sample S427, b) sample S383. Legend below indicates how the thick sections for the SEM are cut and where the peeled off parts of the slip surfaces were collected.

X-ray Powder Diffraction (XRD) is an analysis used to identify the minerals present (Reed, 2005). This method is based on correlating the diffraction that occurs when X-rays enter a crystal lattice, as described by Bragg's Law

$$n\lambda = 2d\sin\theta, \tag{4.1}$$

where n is the order of diffraction, λ is the wavelength of the X-ray, d is the lattice spacing of the crystals, and θ is the diffraction angle (Fig. 4.4).

Here, the planes have a distance d and intercept the radiation with wavelength λ (both given in Å) and an angle θ. The angle between the refracted and the original X-ray is given as the experimental parameter 2θ (Fig. 4.4; Moore and Reynolds (1997)).

Equation 4.1 shows the relationship between the angle of diffraction and the d-spacing of the lattice to the wavelength of the radiation.

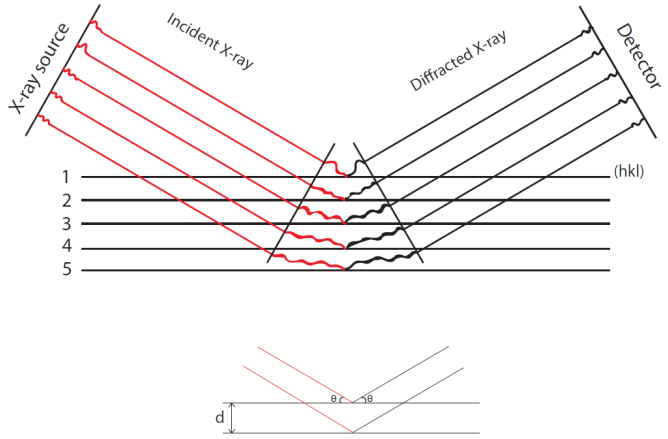

Figure 4.4: Schematic illustration of the principles of X-ray diffraction based on Braggs's law for parallel planes. Modified from (Moore and Reynolds, 1997)

For this study, a Bruker D8 ADVANCE diffractometer with Lynxeye 1-dimensional position-sensitive detector (PSD) was utilized, with CuK-α radiation (λ = 0.154 nm) operated at 40 mA and 40 kV.

4.4.1 Bulk analysis

For the bulk analysis, the samples were first dry milled in a steel disc mill, before a McCrone Micronizing mill was used for 10 minutes for wet milling. The milling process reduces the particle size down to approximately 0.05 mm. After the wet milling, the samples were left to dry at 60 °C over night. The powders from each sample were then prepared in small sample disks, giving randomly oriented samples. A whole-rock analysis was conducted on these randomly oriented samples with a step size of 0.01 degree from 2 degrees to 65 degrees at a count time of 0.3 s for the 2θ. The resultant values are given in 2θ, and represent characteristic diffracted X-ray wavelengths of the different minerals.

4.4.2 Clay analysis

For the clay analysis, the samples were first gently crushed using a mortar. Each sample was put in a volumetric flask separately, and mixed with 200 mL of sodium carbonate and water solution. The clay size fractions were then separated from the larger grain sizes by disaggregating and dispersing the samples in an ultrasonic bath for 10 minutes. The samples rested for 24 hours before approximately 400 mL of distilled water was added, and the samples were put back in the ultrasonic bath for 10 more minutes. After this the samples were left for 6 hours, giving the particles time to settle. The upper 600 mL were then separated from the rest. Approximately 130 mL of each sample was filtered, and attached to a glass slide. This resulted in oriented samples, which then went through the XRD-analysis after being subjected to four different treatments. First the samples were air-dried over night, before they were placed in the XRD-diffractometer. Next they were treated with ethylene glycol (glocalated) within a closed container, before placed back in the XRD-diffractometer. After this they were placed in an oven with a temperature of 350 °C for an hour, before they were out in the XRD-diffractometer. The last treatment was an hour in the same oven as previously, but with a temperature of 550 °C, before they were put in the XRD-diffractometer.

4.4.3 Summary of XRD

For both the bulk and the clay analyses, a diffractogram was produced based on the feedback from the X-rays. The software Diffrac.EVA from Bruker Corporation and the open source software Profex were used to interpret the diffractograms. Each peak on the diffractorgrams represents the different minerals detected. For the clay analysis, a flow diagram from USGS (Poppe et al., 2001) was used to determine what minerals were present based on their distinctive peaks. Illite is identified by the peak at approximately 10 Å, chlorite by the peak at approximately 14 Å and the kaolinite by the peak at approximately 7 Å from the derived diffractograms.

The aim of these analyses was to identify the different minerals present in the samples. The bulk analysis resulted in a semi-quantitative whole rock composition, while the clay analysis resulted in a qualitative clay mineral composition. Human error when interpreting the resulting diffractograms needs to be considered, and is the reason why the bulk analysis is referred to as semi-quantitative. Values of less than 1% of the total amount of dry sample is disregarded, due to the uncertainty of the presence of these minerals.

4.5 Petrographical analysis

Six samples, four thick sections and two pieces mounted to a pin from the two cores (Fig. 4.3) were analyzed in the scanning electron microscope (SEM). For the analysis a Hitachi SU5000 FE-SEM with Dual Bruker Quantax XFlash 30 EDS system was used. The analysis targeted the following:

- Mineralogical composition and organisation within the samples.
- Differences regarding mineralogy comparing samples S383 and S427.
- How the fractures appear on the surface.

Due to the weakness of the shale, thin sections were not possible to make, thick sections were therefore prepared. Two of them were made from sample S427, and two from sample S383, where one was made parallel to the direction of motion on the fracture surface and one was made perpendicular to this. The two pins had grain mounts attached that were peeled off of the fracture surface, one from the sample S427 and one from the sample S383 (Fig. 4.3).

Before conducting the analysis the thick sections were treated with a carbon coating, while the grain mounts were treated with a gold coating as the samples can not conduct electricity on their own (Reed, 2005).

The samples were mainly analyzed using the backscattered electron (BSE) images. In some cases the secondary electron (SE) imaging was used to study the topography of the fracture surfaces. For further theoretical information about these two imaging methods, see Reed (2005).

Chapter 5

Results

This chapter presents the results derived from the data presented in the previous chapter and includes:

- A complete fracture analysis of the upper Slottsmøya and lower Wimanfjellet members of the Agardhfjellet and Rurikfjellet formations in boreholes DH2 and DH4.
- Interpretation of decimeter-scaled deformation features in the Slottsmøya Member of the Agardhfjellet Formation at Deltaneset, central Spitsbergen.
- Mineralogical composition and distribution descriptions determined by XRD and SEM analyses of S383 and S427.

5.1 Fracture analysis

The fracture analysis is based on structural logging of the drill cores and scanline data obtained from the field studies. The close proximity of the field area to the area where the drill cores are obtained give an outcrop analogue to the subsurface stratigraphy seen in the drill cores. The data from the drill cores gives a vertical understanding of the fracture distribution, whereas the outcrop provides a lateral understanding of the deformation.

5.1.1 Structural logging of boreholes

A total of 1172 fractures within 132 m of core were identified and measured, where 607 were identified in DH4 (at depths between 380 m and 452 m) and 565 fractures were

identified in DH2 (at depths between 450 m and 510 m). The boreholes are situated 7 km apart (Fig. 4.2). Both open fractures and mineral filled veins were recorded. In addition, sections of heavily crushed core were observed (Fig. 5.2) in which fracture frequency could not be recorded (grey areas in the logs; Fig. 5.1).

The boundary between the Slottsmøya and Wimanfjellet members of the Agardhfjellet and Rurikfjellet formations is based on previous publications (Koevoets et al., 2018; Olaussen et al., 2019), and is defined by the presence of the Myklegardfjellet Bed. The boundary is interpreted to be located at 405 m depth in DH4 and at 480 m depth in DH2. The fracture frequencies vary from 0 fractures/meter (f/m) to 37 f/m throughout the upper Slottsmøya Member and 0 f/m to 34 f/m in the lower Wimanfjellet Member within both of the drill cores.

DH4: The interval between depths 394 m and 417 m exhibits high fracture frequencies, with a range of 10 f/m to 37 f/m and holds the highest abundance of crushed core (Fig. 5.1). The boundary between the Slottsmøya Member and the Wimanfjellet Member is interpreted to be in the middle of this highly shattered zone. Above this zone, the frequencies decrease to below 4 f/m. In the lowest interval (between depths 418 m and 452 m), the fracture frequency is 0 f/m to 14 f/m with few crushed intervals (Fig. 5.1). Only ten calcite filled veins were detected, which were distributed throughout the studied interval (i.e., not clustered). The veins were mainly steeply dipping, with dips ranging from 50° to 80°.

DH2: The interval between depths 451 m and 487 m exhibits higher frequencies than what is observed in the rest of the studied part of this core. Within said interval, 0 f/m to 34 f/m were observed and multiple intervals of completely crushed core were recorded (more common than in DH4). This interval correlates to the the lower part of the Wimanfjellet Member. Below this zone, the fracture frequencies are low with a measured amount of 0 f/m to 3 f/m. A small increase in fracture frequency is observed towards the lower part of the studied core, with a range from 0 f/m to 15 f/m at depths between 500 m and 510 m. 18 calcite filled veins 18 were observed, some were clustered. Most veins exhibit steep dips, but two showed lower dip angles in the range of 0° to 28°. All veins are situated in the interval between depths 468 m and 472 m.

In DH2, the zones with the highest fracture frequencies and crushed core are thicker

than in DH4. The number of measured fractures is approximately the same for both wells, but the distribution of the fractures throughout the cores is different. With regards to depth, the most intense deformation is observed at a greater depth in DH2, which is located farther northwest. The simplified sedimentary logs (Fig. 5.1) made from both drill cores show that the lithologies mainly consists of shales and silty shales. In DH2 some thin fine-grained sandstone beds have also been identified. The intervals exhibiting the highest fracture frequencies in the two drill cores corresponds to the finest grained lithologies, mainly consisting of either shale or silty shale (Fig. 5.1), but no major lithological differences are recorded in the cores.

The highest fracture frequency seems focused along the boundary between the Agardhfjellet Formation and the overlying Rurikfjellet Formation in both drill cores. A décollement zone has been recorded to be located along or in close proximity to the boundary (Olaussen et al., 2019), which corresponds to the findings in this study. The difference in depths of this highly fractured zone between the two drill cores corresponds to the regional dip of the CTB of 1° to 3°.

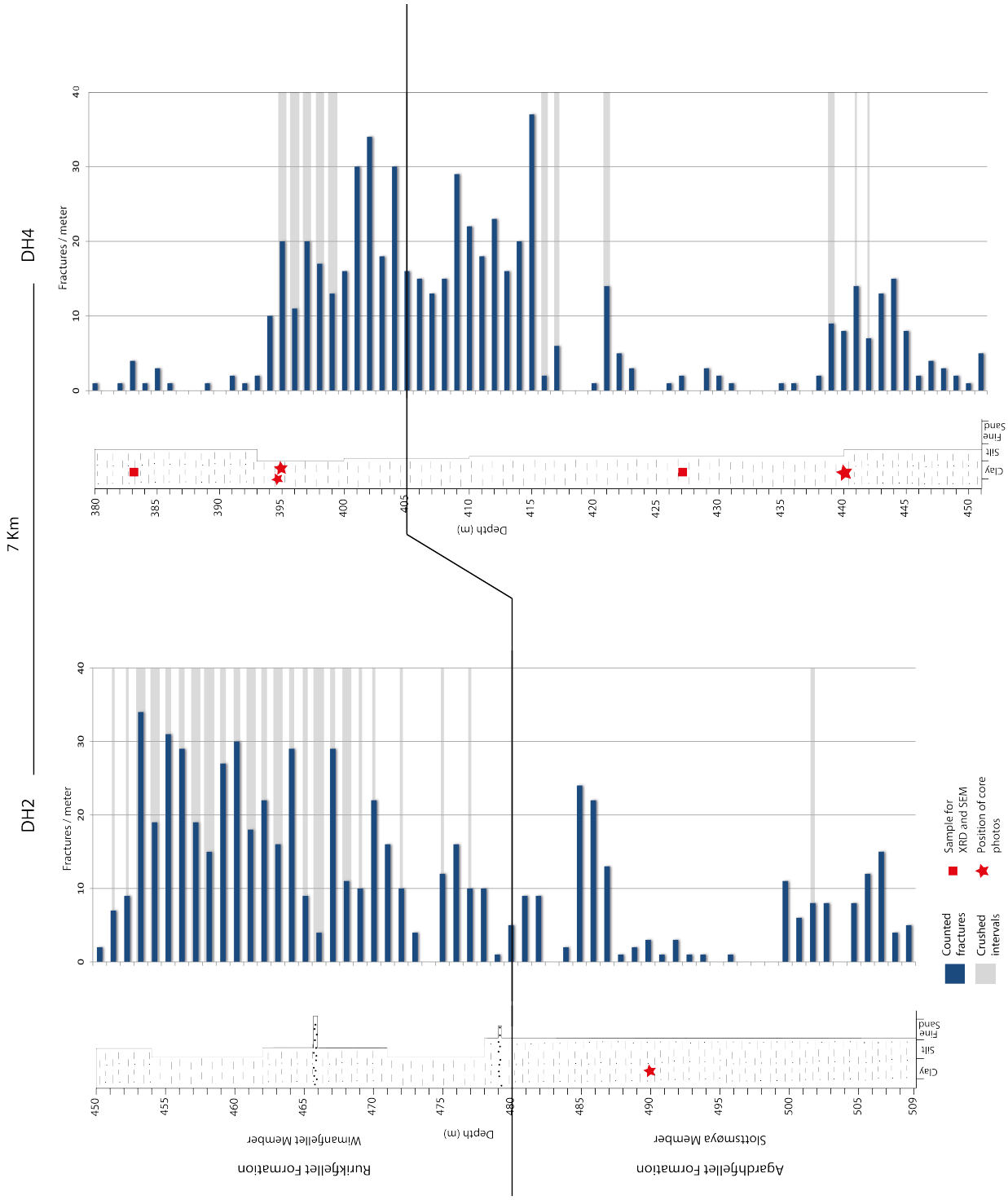

Figure 5.1: Fracture frequency plots for DH2 and DH4. The blue bars represents the number of fractures recorded at the given depth (m), and the grey lines indicate zones of crushed core. The width of the grey lines represents the thickness of the interval of crushed material within the given meter.

Figure 5.2: Crushed core (lower part of the picture) compared to the highly fractured core (upper part of the picture). The crushed part of the core has mid point depth 398.7 m. The fractured core is situated upsection in relation to the crushed core in this photo.

Measured fractures exhibit a wide range of dips. Most fractures show a dip between 0° and 30°. Dip distribution is similar in both drill cores (Fig. 5.3). The areas with the most intensely crushed core exhibit most of the horizontal to sub-horizontal fractures, whereas the areas with a lower fracture frequency exhibit a larger range of dip angles. The veins often show steeper dip angles compared to the open fractures, with most angles ranging from 50° to 90° (Fig. 5.4). The cores predominantly show flat-lying bedding, and as such, the dip angles are measured relative to the bedding planes. The drill cores are not oriented, hence the fracture strike could not be recorded.

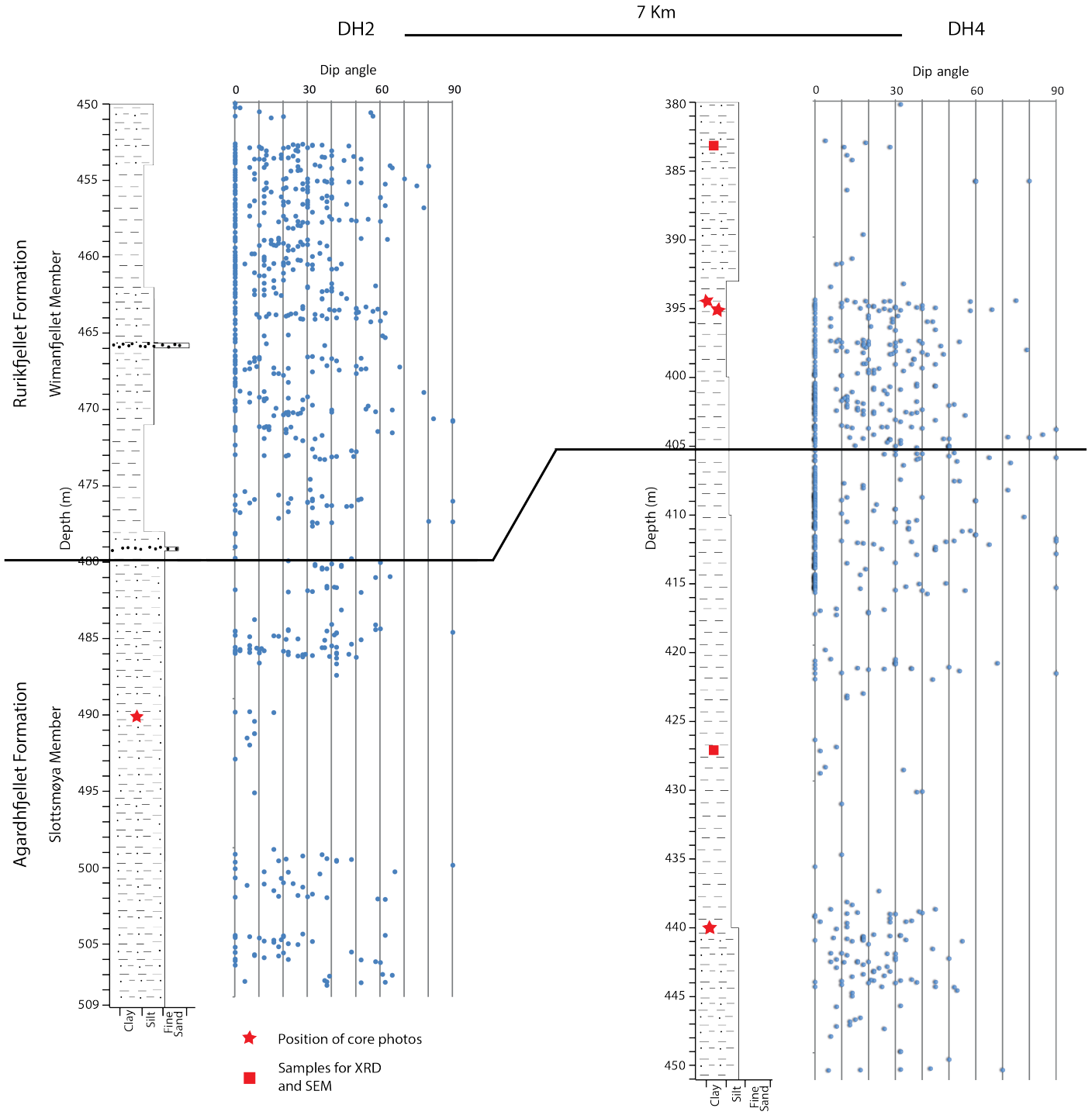

Figure 5.3: The distribution of dip angles vertically within DH2 and DH4. The areas with highest frequencies also show the largest proportions of low-angle fractures.

Figure 5.4: Steeply dipping calcite veins, with an aperture of 1 mm to 2 mm, from the Rurikfjellet Formation. The vein was situated at 383 m depth in DH4. The diameter of the core is 78 mm.

5.1.1.1 Fracture modes and characteristics

The fractures that were measured in the two drill cores were characterized by the four fracture modes listed in Section 2.1.1. Further, fracture surfaces were defined based on appearance. Of the 1172 fractures measured, 147 surfaces could not be defined in DH4 and 6 could not be determined in DH2 as they were considered altered after coring or too porous to define. In addition, the veins did not show any surfaces and could therefore not be characterized. In DH4, 10 veins or clusters of veins were identified and in DH2, 18 veins (sometimes clustered) were identified. Therefore, 452 and 552 surfaces were identified as polished and/or rough in DH4 and DH2 respectively (Fig. 5.5). The fracture surfaces measured can show components of polished and/or rough surfaces, or none of them. The results show that 86.7% of the surfaces in DH4 exhibit polished or partly polished surfaces whereas 16.8% show rough or partly rough surfaces. In DH2, 60.5% show polished or partly polished surfaces, 26.8% rough or partly rough surfaces, and 14.7% not polished or rough. The fractures in both drill cores exhibit slickensides on approximately 38.0% of surfaces (Fig. 5.5). The polished low-angle surfaces with slickensides are interpreted to be Mode II fractures. Whereas the rough surfaces, often high angled, are interpreted to be Mode I fractures. In general the veins recorded have an aperture of approximately 1

mm to 2 mm, and they are filled with carbonates/calcite (Fig. 5.4). The carbonate filling implies that these discontinuities have acted as pathways for fluids in the past, before mineralization has led to a healing of the joints (Gale et al., 2014).

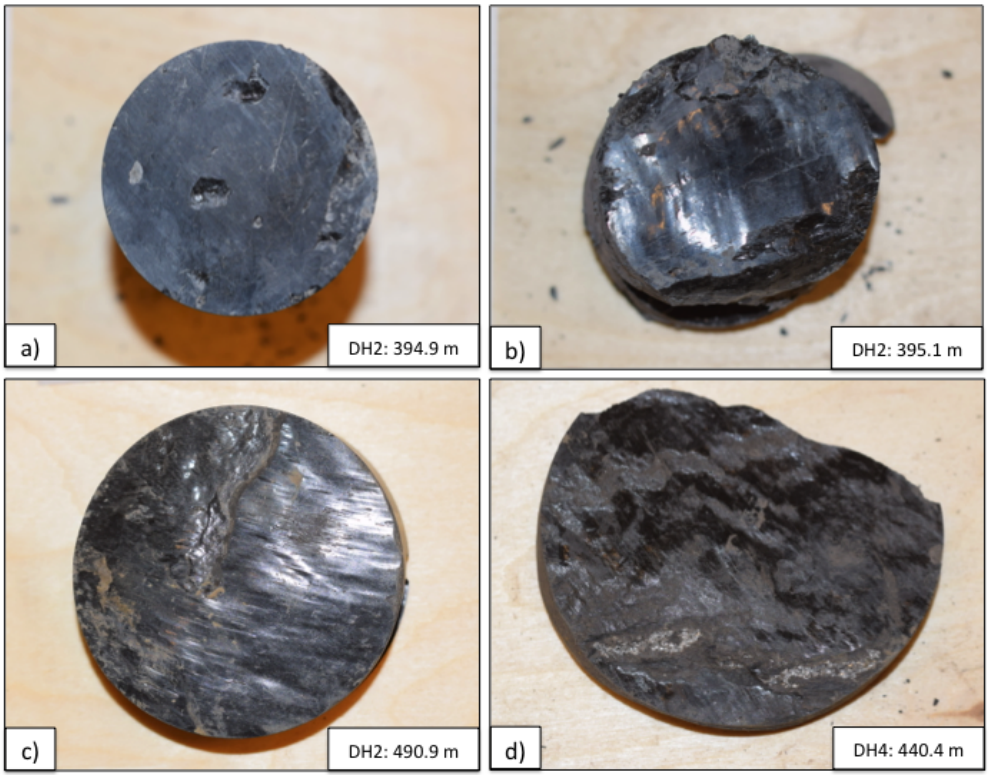

Figure 5.5: Different types of open fractures observed in DH2 and DH4. a) rough fracture surface without slickensides from the Wimanfjellet Member, b) polished surface without slickensides from the Wimanfjellet Member, c) polished surface with slickensides from the Slottsmøya Member, d) polished and rough surface with slickensides from the Slottsmøya Member. All drill cores are 78 mm in diameter.

5.1.2 Outcrop studies

Five scanlines consisting of a total amount of 369 measured fractures were produced (Table 5.1). A high lateral fracture frequency was observed within all of the lithological units studied. Based on the limited data set, the coarser grained units, silty shale and fine-grained sandstone, show both a higher maximum amount of fractures and average fracture frequency than that seen in the shales.

Table 5.1: Overview of scanline data, where KW1 represents the lowermost and KW5 represents the uppermost stratigraphy.

Scanline	Number of fractures	Logged distance (m)	Average (f/m)	Max (f/m)	Lithology
KW1	89	7.9	11.1	15	Black paper shale
KW2	50	8.6	5.6	10	Black to grey paper shale
KW3	83	6.2	11.9	25	Brownish silty shale
KW4	100	6.4	14.3	22	(Silty) black shale
KW5	47	2.8	15.6	17	Fine sand (silty), well cemented

The fracture measurements reveal five dominant fracture sets that trend NNW—SSE (F1), NE—SW (F2), NW—SE (F3), ENE—WSW (F4) and N—S (F5). Dip angles were primarily steep, with a range between 60° and 90° (Fig. 5.6). No discontinuities interpreted as fractures had a dip lower than 38°.

Distinguishing between bedding and horizontal fractures has proved difficult due to the highly weathered outcrops. A bias towards the steeper dipping fractures therefore needs to be considered when interpreting the results. In addition, the orientation of the scanlines with regard to the bedding has an impact on the results obtained from the data set. As the outcrop only has a two-dimensional exposure, the orientation of the scanlines with regard to the bedding is difficult to define and is therefore assumed to be perpendicular to the bedding planes.

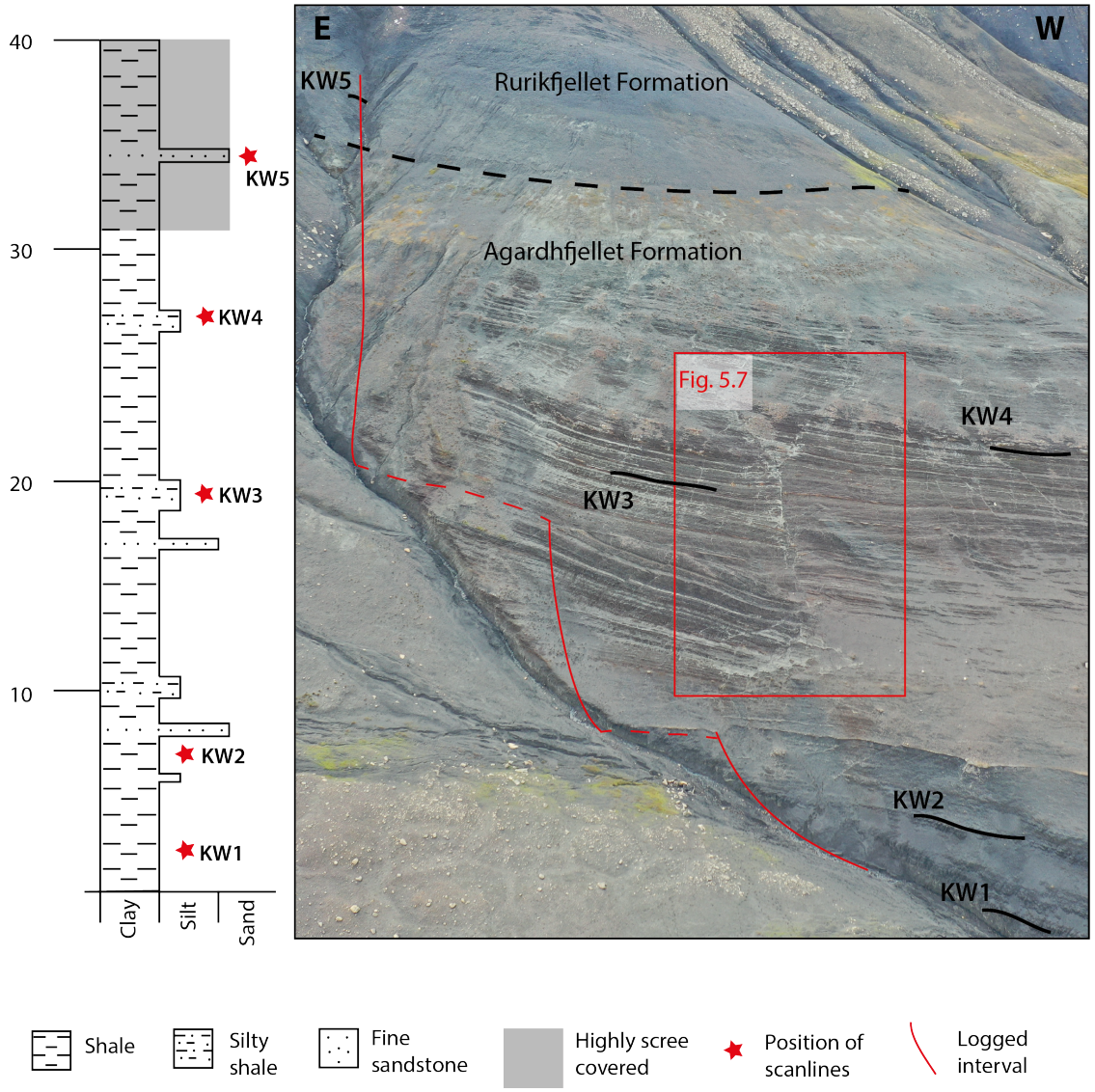

Figure 5.6: The study area at Konusdalen West where the scanlines were obtained. The position of the scanlines are marked with a black line, and labeled with KW1 to KW5. All scanlines are collected from (south)east to (north)west. Location of outcrop is shown in Figure 4.2.

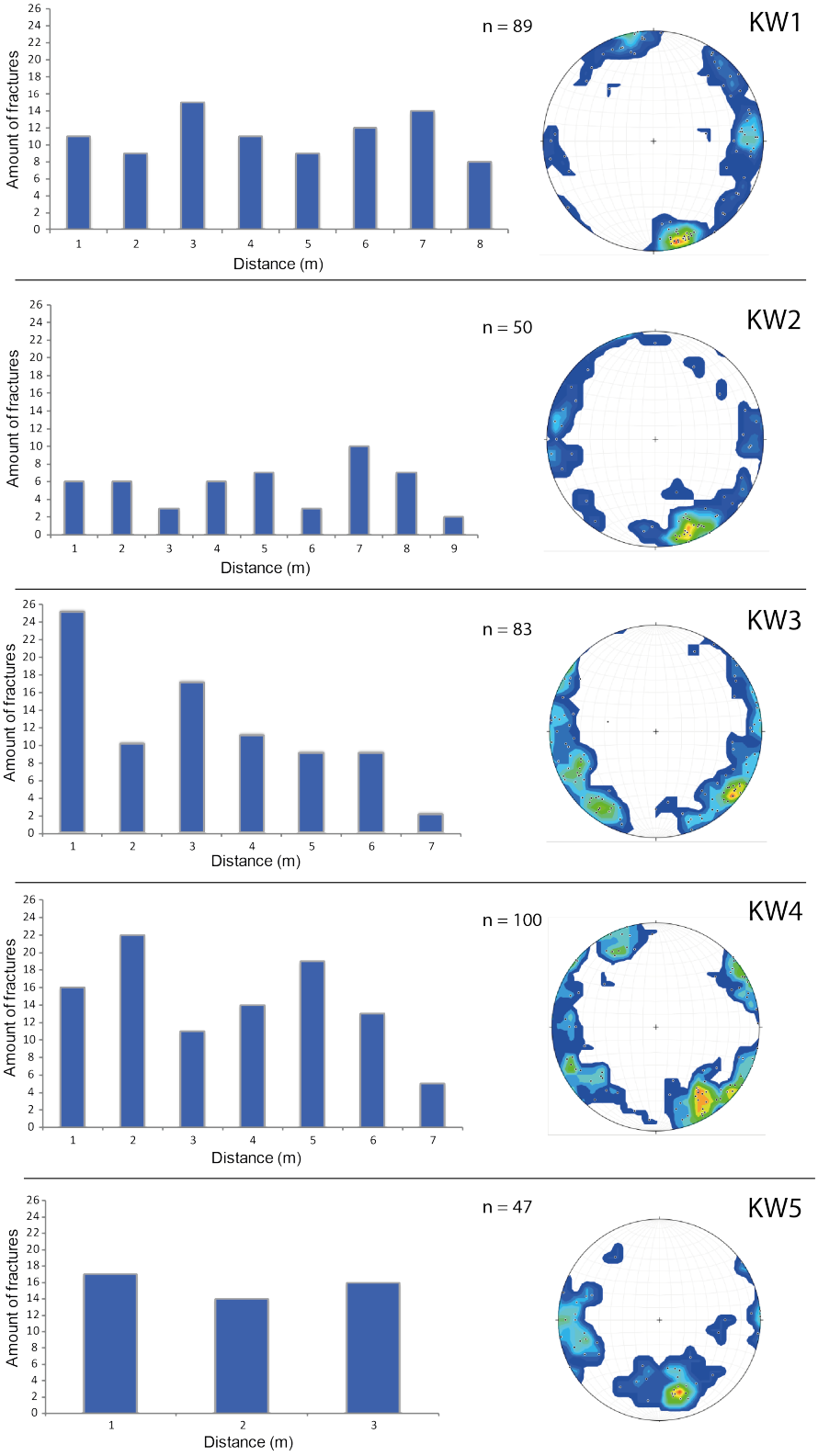

Figure 5.6: The frequency and orientation of the fractures from five scanlines measured in upper Konusdalen West. Stereonets are made with a 1% contouring of the poles. n = number of fractures measured.

Fracture frequency varies along the scanlines produced (Fig. 5.6). Beds with the coarsest grained material, i.e., sandstone and siltstone have the highest recorded fracture frequencies. An average of 15.7 f/m was observed in the fine-grained sandstone beds, an average of 11.9 f/m and 14.3 f/m were seen in the silty-shale beds, whereas an average of 5.6 f/m and 11.1 f/m were observed in the shale beds (Tab. 5.1). As such, grain size is interpreted as a controlling factor in fracture frequency.

Most fractures were observed as open, and are interpreted to be Mode I fractures. Some healed, Mode I fractures containing a white/yellow mineral infill were also identified. The filling is interpreted to be gypsum and calcite based on previous publications such as e.g., Koevoets et al. (2018), but no hydroclorid acid was used to identify the mineral fill. Some fracture sets had a perpendicular orientation and showed some slickensides along the surfaces. These were interpreted to be high-angle conjugate fracture sets and defined as Mode II fractures. The distinction between bed-confined and through-going fractures was not possible to determine in the field because of the highly scree covered and weathered outcrops.

5.2 Faulting and folding

Different meso-scale structures (< 20 m long) were observed in the field. These were mainly mapped at two different locations (Fig. 4.2), and is interpreted to be situated in the same stratigraphic interval.

5.2.1 Meso-scale discontinuities

Two thrust faults with opposing dips were observed in the upper Konusdalen West (Fig. 4.1), illustrated in Figure 5.7. The fault to the east (PUF) change direction upwards from SSE to SE, while the fault to the west (APUF) has a direction from SW. Both faults are steeply dipping, with approximately a 76° dip towards each other at the upper part. In the lower part of PUF, displacement is measured to be 1.86 m across the fault. The strata between the two upper faults is upthrown with respect to the strata in the footwall of each fault segment. This thrust structure, consisting of the two fault segments, is interpreted to be a pop-up structure. The orientation of the main fault is consistent with formation during the Paleogene transpressional event (Bergh et al., 1997). Given this context, the two faults can be considered hinterland (PUF) and foreland (APUF) vergent.

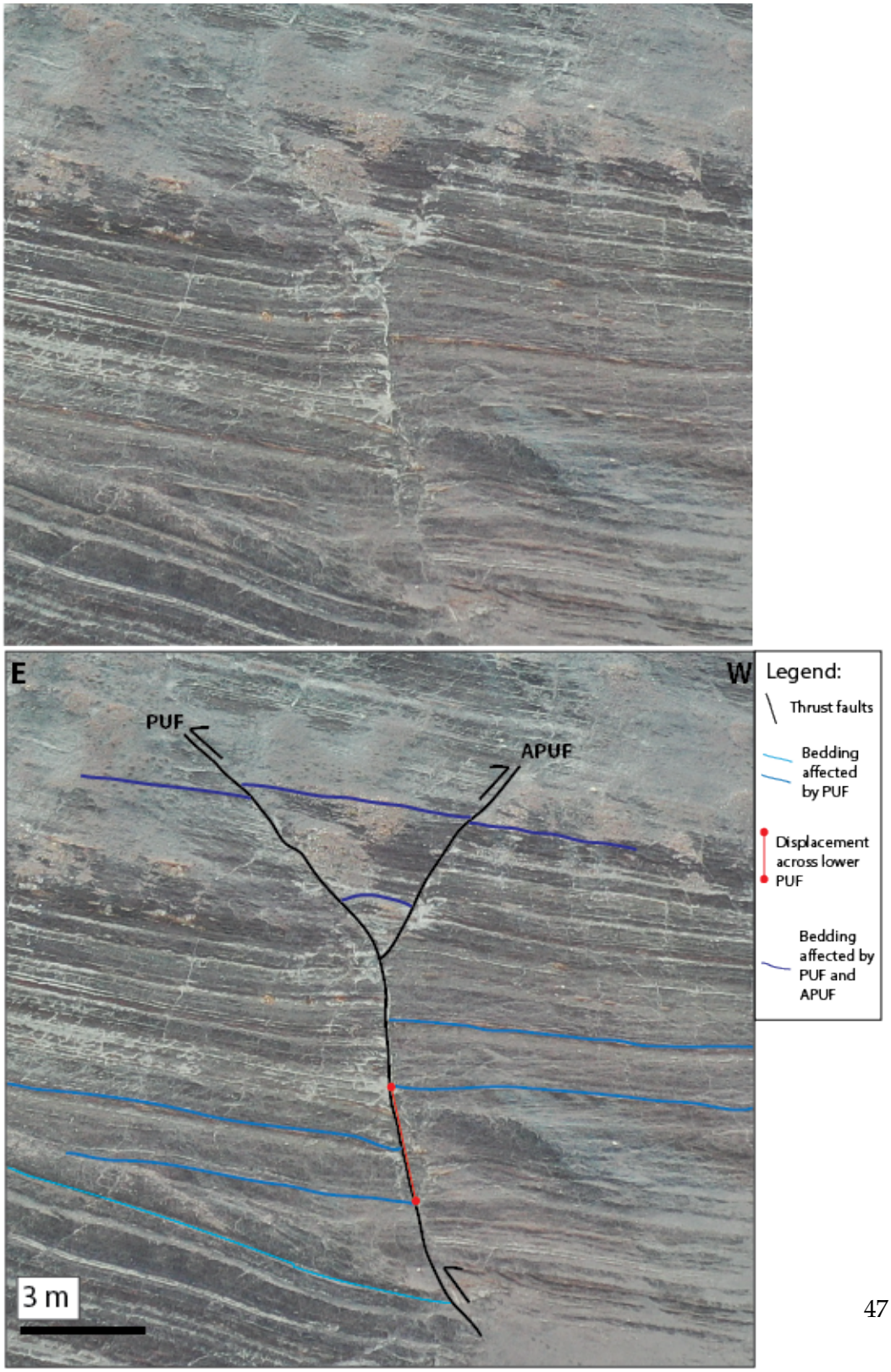

Figure 5.7: Two thrust faults with opposing dips define a pop-up structure in the upper Konusdalen West. The displacement along PUF is measured to be 1.86 m. The upper picture shows the outcrop without interpretation.

Multiple, NNW—SSE oriented lineaments are observed to the east of the structure observed at Konusdalen West (Fig. 4.1). These features have consistent orientations and are apparently bounded by a roof and a floor thrust, as they are tipping out. The features are interpreted to be genetically linked horses, where the thrust fault to the east (DF1) have a higher dip angle than the thrust fault further to the west (DF2). Dip angles are 70° to 78°, and 58° to 70°, respectively (Fig. 5.8). The displacement across these faults can be observed in the coarser grained silty shale which provide markers. Maximum observed displacement is highly varied, and ranges from 1 cm to 40 cm for different faults. Between the silty shale intervals, which exhibit brittle deformation, the black paper shales exhibit more ductile deformation where small scale folding is observed. The feature consisting of the multiple small-scale faults is interpreted as a duplex structure.

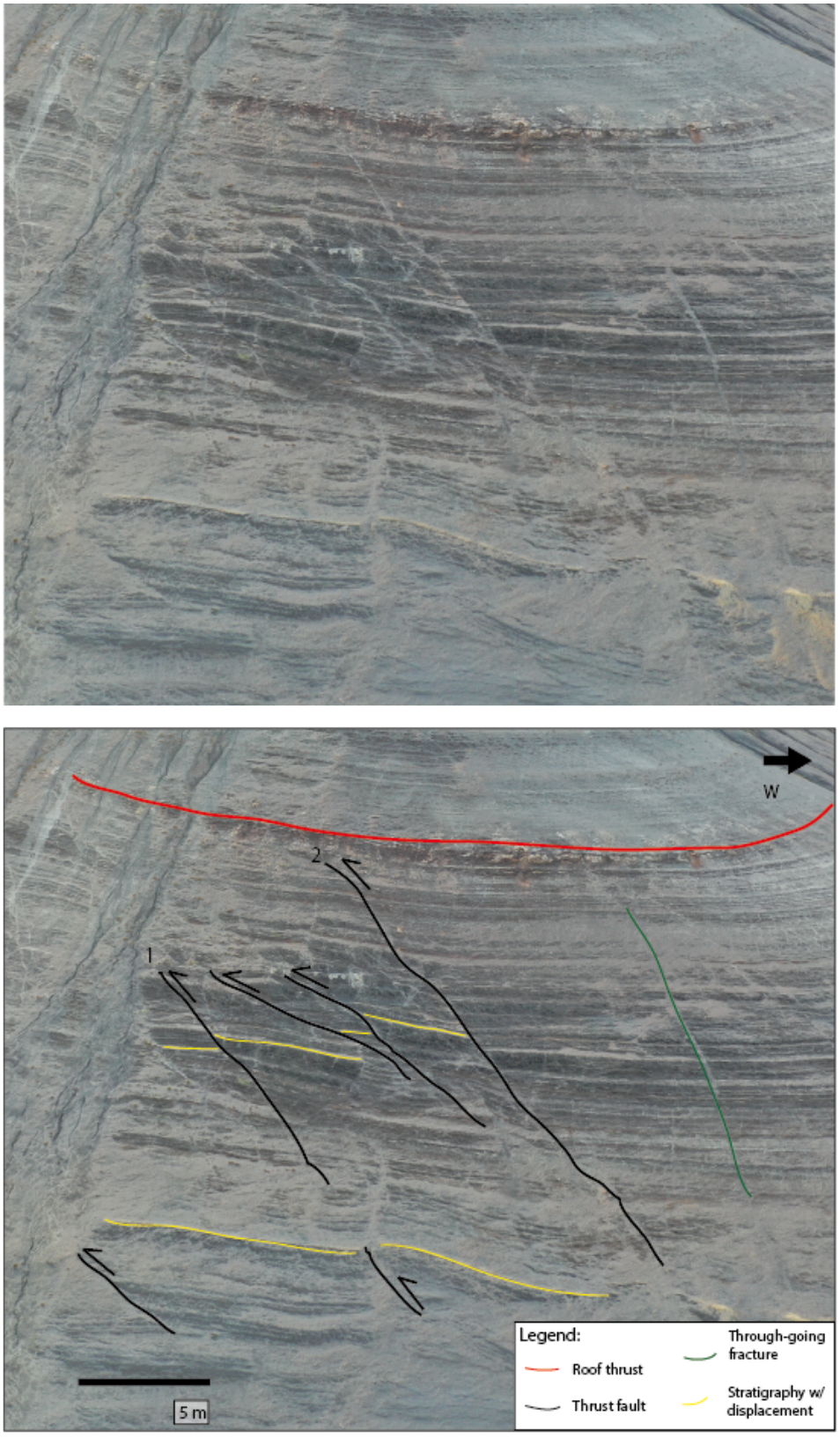

Figure 5.8: Multiple, steeply dipping thrust faults bound by an apparent upper roof thrust at the study area east of Konusdalen West (Location shown in Fig. 4.2). This is interpreted to be a duplex structure. The floor thrust is not visible in the picture. 1-DF1 and 2-DF2 in the text. The upper picture shows the outcrop without interpretation.

In addition, through-going, whiteish lineaments (> 1 m long) were observed throughout the studied area (e.g., green line, Fig. 5.8). These show no apparent displacement across them, and were therefore interpreted to be through-going, healed joints. These fractures exhibit a NW—SE orientation, and often exhibit white/yellowish mineral fillings (Fig. 5.8). These discontinuities were found close to the larger brittle deformation structures, such as the pop-up structure and the duplex structure, with the same orientation as measured on the larger thrust faults. The fractures are mainly sub-vertical (70° to 85° dip) and healed within the black paper shale, these features are also documented by Ogata et al. (2014a).

The thrust structures are interpreted to be in the upper Agardhfjellet Formation, with the thrust plane of the décollement zone along the boundary between the Agardhfjellet and Rurikfjellet formations acting as the roof thrust.

5.2.2 Fold structures

Within the black shale, tight folding (cm to 10s of cm scale wavelength) was observed. The shale exhibited highly deformed layers close to competent beds containing coarser grained material. In the Wimanfjellet Member, the ductile deformation was observed wrapping around a competent, sand-rich bed (Fig. 5.9).

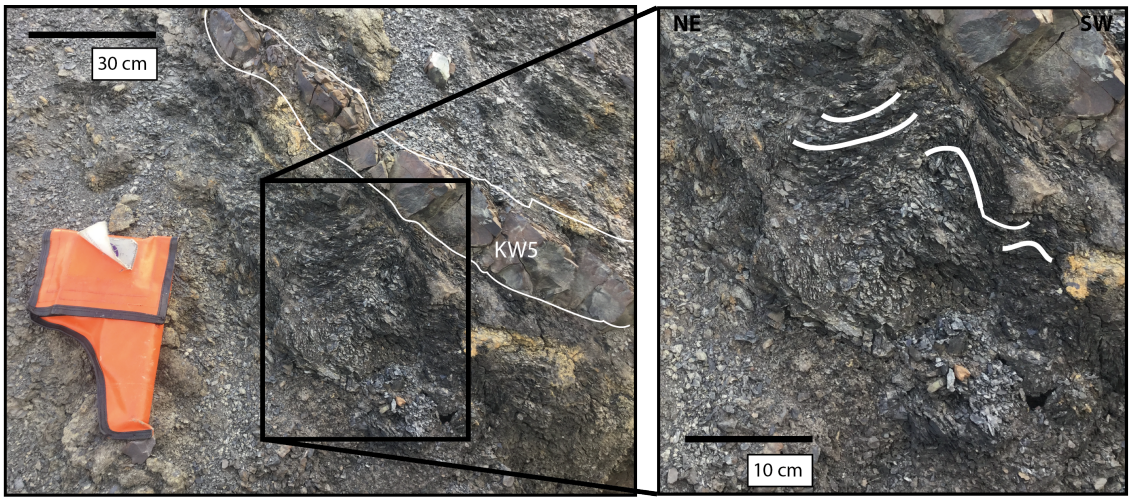

Figure 5.9: Black paper shale below competent sandstone bed illustrating ductile deformation in the area. White lines indicate the folding of the black paper shale. Location is just below KW5 marked in Figure 5.6.

Further up Janusfjellet to the east of Konusdalen West, tight folds verging towards the NE are also observed on a larger scale (m scale wavelength). These features are seen where the whiteish layers are tightly folded (Fig. 5.10). This feature is one example of multiple similar folds, and is interpreted as a fault propagation fold formed in a contractional regime. The white layers is interpreted to be a result of previous fluid flow.

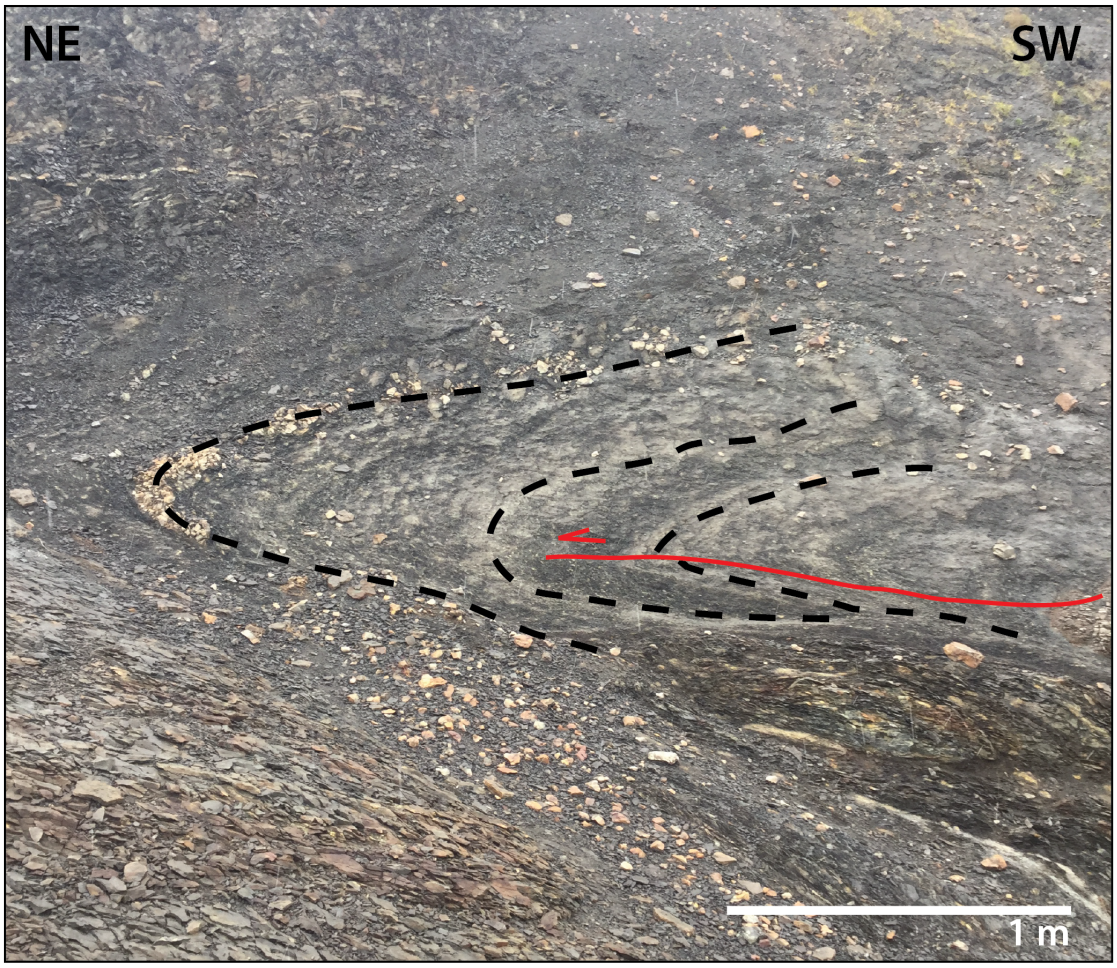

Figure 5.10: Fault propagation fold observed higher up Janusfjellet to the east of Konusdalen West, with a NNW—SSE orientation. Black dashed lines marks the folded bedding and red line marks the fault plane. Location of the fault is marked in Figure 4.2.

5.3 Mineralogy and compositional description

The composition and distribution of minerals within the studied interval is described using two samples from DH4. A comprehensive description is given based on the XRD and SEM analyses, using the methods described in Section 4.4 and 4.5.

5.3.1 Mineral composition

The description of the mineral composition is derived from the semi-quantitative XRD bulk analysis and the qualitative clay analyses. Mineralogy determined from the analyses are listed in Table 5.2.

Clay minerals comprise 52.1% of the bulk sample from S383, and 35.3% of the sample S427. Both samples are therefore dominated by clay minerals. The same clay minerals are present in both samples, with the main constituent being muscovite/illite. The two other clay minerals identified in the bulk analysis are chlorite and kaolinite.

The peaks used to identify illite, chlorite and kaolinite, as mentioned in Section 4.4.3, are observed in both samples. These peaks exhibit different intensities for each sample. Sample S383 exhibits a peak at 11 Å in untreated conditions. This peak indicates that an illite-smectite transition phase may be present. No other indicators of smectite are observed. The absence of smectite indicates a burial depth of more than 1 km of the rock mass, which caused a dehydration of the clay minerals. This depth corresponds to previous findings of burial (Olaussen et al., 2019).

Quartz is the other main constituent within the two samples. The amount of quartz is approximately the same for the two samples, with 26.4% in S383 and 24.2% in the S427.

Three carbonate minerals are observed, with different occurrences in the two samples. Dolomite is observed in both samples. Siderite is recognized in sample S427. Calcite is only observed in S383. The total abundance of carbonate minerals are considerably larger in sample S427.

Feldspar is observed in different variants. Both K-feldspar, such as orthoclase, and plagioclase such as albite are observed in both of the samples. The anorthite (plagioclase var.) is only observed in sample S427.

Sheet silicates such as biotite and muscovite is observed in both samples. The peaks for the muscovite and illite is hard to separate, hence they are referred to combined. The clay analysis confirms the presence of illite.

Table 5.2: XRD derived bulk composition of samples S383 and S427. Values are given as percentage of total amount of the dry sample. 2M refers to the polytype of the muscovite.

	Mineral	S383 (%)	S427 (%)
Non-clay minerals	Quartz	26.4	24.2
	Cementite	3.4	3.9
	Anatase (TiO2)	3.1	0.0
	Gibbsite	2.4	2.7
	Orthoclase	2.1	3.4
	Albite	2.0	2.5
	Biotite	1.7	3.7
	Aragonite	1.5	0.0
	Rutile	1.4	1.7
	Pyrite	1.1	4.6
	Dolomite	1.0	2.5
	Calcite	1.0	0.0
	Plagioclase - An	0.0	4.3
	Siderite	0.0	3.1
	Azurite	0.0	1.6
	Gypsum	0.0	1.6
	Monazite	0.0	1.4
	Hornblende	0.0	1.2
	Dravite (Tourmaline)	0.0	1.1
Clay minerals	Muscovite (2M)/Illite	42.5	26.3
	Chlorite	8.5	3.8
	Kaolinite	1.1	5.2
Total clay content		52.1	35.3

The two samples have a different composition of the accessory minerals. Cementite representing iron rich carbonate cement is observed, as well as considerable amounts of minerals such as pyrite and titaniumoxide minerals (rutile and anatase). The minerals that are interpreted in the diffractograms showing a lower appearance than 1.5% in Table 5.2 are somewhat difficult to distinguish, but contributes to a better fit in the diffractograms and eliminates some of the residual peaks (see Appendix A).

For the bulk XRD analysis, the minerals recorded with a lower abundance than 1% were removed due to the uncertainty of presence. These minerals are excluded from the total count, and make up approximately 1% of the total amount of the dry samples.

Based on the mineralogy, a brittleness index (BI) can be calculated, and is defined by Wang and Gale (2009) to be the fraction of brittle minerals (e.g., quartz and dolomite) within the matrix volume. In our case

$$BI = \frac{V_{\text{Quartz}} + V_{\text{Dolomite}}}{V_{\text{Quartz}} + V_{\text{Dolomite}} + V_{\text{Clay}} + V_{\text{Calcite}} + V_{\text{TOC}}} \tag{5.1}$$

where V_m is the volume of mineral m.

TOC values used in the calculations are based on previous findings (Dypvik, 1984; Koevoets et al., 2018), and are set to 1.25% and 1.75% for S383 and S427, respectively. Inserting TOC values and observed volumes from Table 5.2) into Equation (5.1), we find that for S383 $BI = 0.34$, and for S427 $BI = 0.42$.

5.4 Mineral distribution

The results for the mineral distribution is derived from the SEM analyses of the four thick sections and two pieces mounted to a pin from DH4, as described in Section 4.5 and shown in Figure 4.3. The two samples analyzed are both collected from intervals exhibiting a polished surface with slickensides.

5.4.1 Agardhfjellet Formation

Sample S427 shows that the illite is present in the entire sample and acts as a matrix for the observed grains. The grains show no preferred orientation within the matrix (Fig. 5.11).

Three carbonates, dolomite, siderite and ankerite, are observed in the sample. In the thick-section that was cut perpendicular to the slip movement, the dolomite is distributed

evenly within the sample. In the thick-section cut parallel to the direction of movement, the dolomite is arranged along the slip surface. Within the grains arranged along the slip surface, internal deformation is observed as cracks/fractures. The dolomite exhibits an anhedral shape, whereas siderite is often observed as sub-rounded and subhedral crystals throughout the sample.

The quartz grains observed are evenly distributed and vary in size from a few µm up to 50 µm. Generally the quartz exhibits a (sub-)rounded and subhedral shape. Quartz is observed throughout the studied part of the sample, and is abundant.

Pyrite is also observed throughout the sample and exhibits a framboidal shape, and is sometimes found within the quartz grains. When studying the slip surface, pyrite is also observed scattered along this surface.

Clay minerals such as chlorite and kaolinite are observed within the matrix (Fig. 5.11). These clay minerals exhibit an elongated shape, show no preferred orientation and are evenly distributed throughout the studied part of the samples. In addition, muscovite is observed as elongated grains within the matrix.

Organic fragments recognized as black spots is observed in varying size and is distributed evenly throughout the matrix (Fig. 5.11). Organic matter is also present along the slip surface.

Other minerals such as albite (feldspar var.) and apatite are observed and usually exhibit sub-rounded and subhedral shapes.

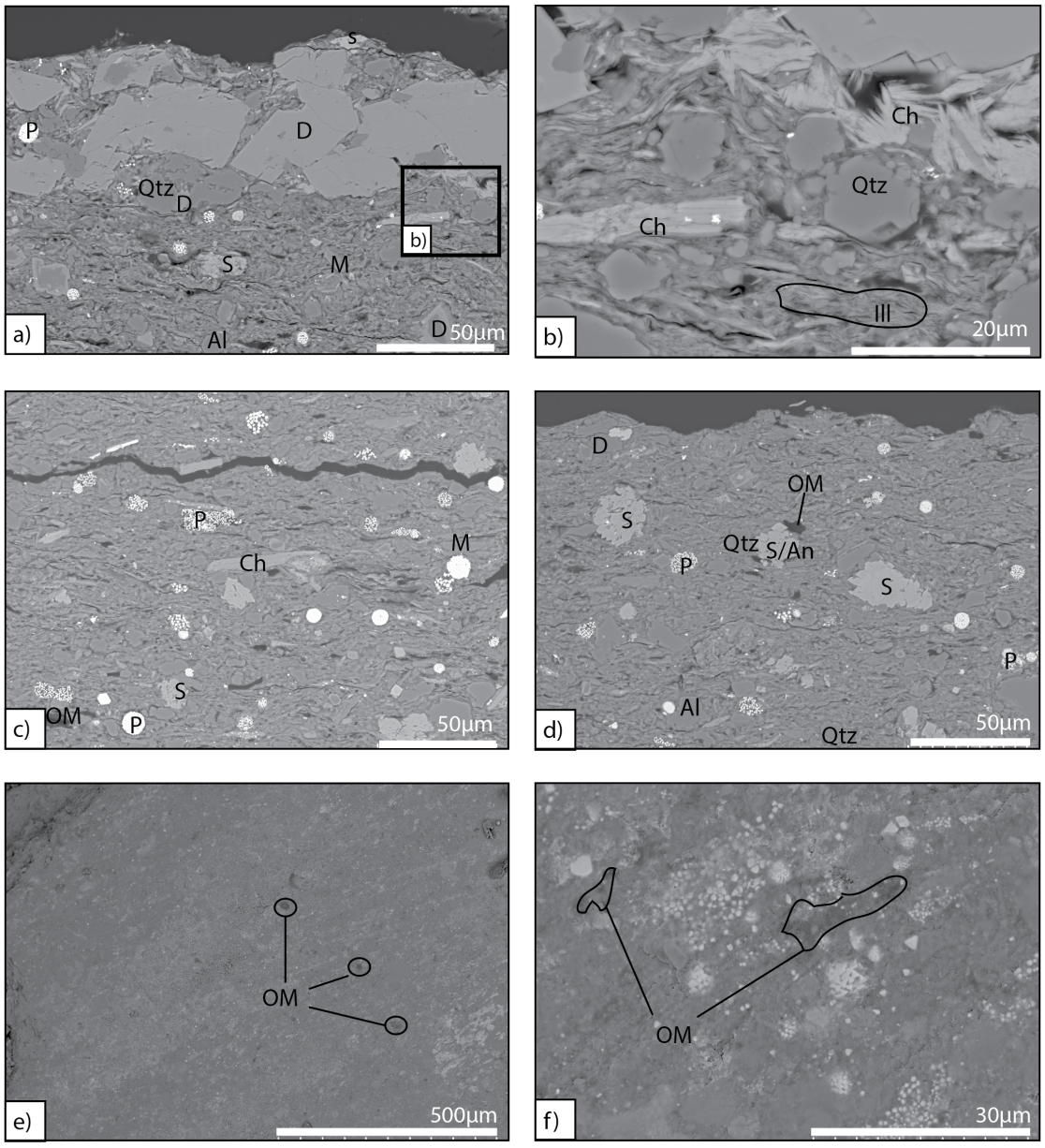

Figure 5.11: SEM images of the thick sections and pin samples from sample S427. a) and b) are from the sample cut perpendicular to the movement direction, c) and d) are from the sample cut parallel to the movement direction, e) and f) are from the surface sample. a) Dolomite arranged along the slip surface, b) distribution of different minerals within the matrix, c) and d) show the distribution of the minerals within the matrix, pyrite is widespread, e) and f) show how the organic matter is present on the slip surface. In f) the pyrite is also visible. P - pyrite, D - dolomite, Qtz -quartz, M - muscovite, Al - albite, S - siderite, Ch - chlorite, Ill - illite, OM - organic matter, An - Ankerite. All photos are BSE images.

5.4.2 Rurikfjellet Formation

The SEM analysis of the thick-sections from sample S383 exhibit a matrix supported rock, with illite acting as the matrix (Fig. 5.12). No preferred orientation of the grains are observed. In general, quartz and clay minerals are the most abundant grains supported by the matrix.

Carbonate minerals, siderite and dolomite, is present throughout the sample. The siderite is often found alone, with a sub-hedral/euhedral and subrounded shape. In some places the siderite encapsulates the dolomite. The siderite observed in this sample is rich in manganese (Mn). The dolomite present in the sample is euhedral, and evenly spread throughout the sample.

Quartz is observed throughout the studied part of the sample and exhibits sub-rounded and subhedral shapes. The size of the quartz varies from a few µm up to 40 µm.

The pyrite is observed as both framboidal shapes in large clusters and as small fragments with an anhedral shape. The clusters of pyrite is prominent is this sample compared to sample S427.

Chlorite is observed as elongated grains within the matrix and is present throughout the sample. Around the clusters of pyrite, the kaolinite forms platy minerals. In addition, muscovite is observed as elongated grains.

Organic matter can be seen throughout the sample and along the slip surface. The organic matter is recognized as black spots.

Other minerals such as titanium-oxide (TiO_2, e.g. rutile) are observed as small grains of a few up to ten µm. Apatite, zircon, feldspars such as albite, chalcopyrite and tourmaline are also observed in different quanta. In addition, a mix of illite and apatite can be observed in clusters.

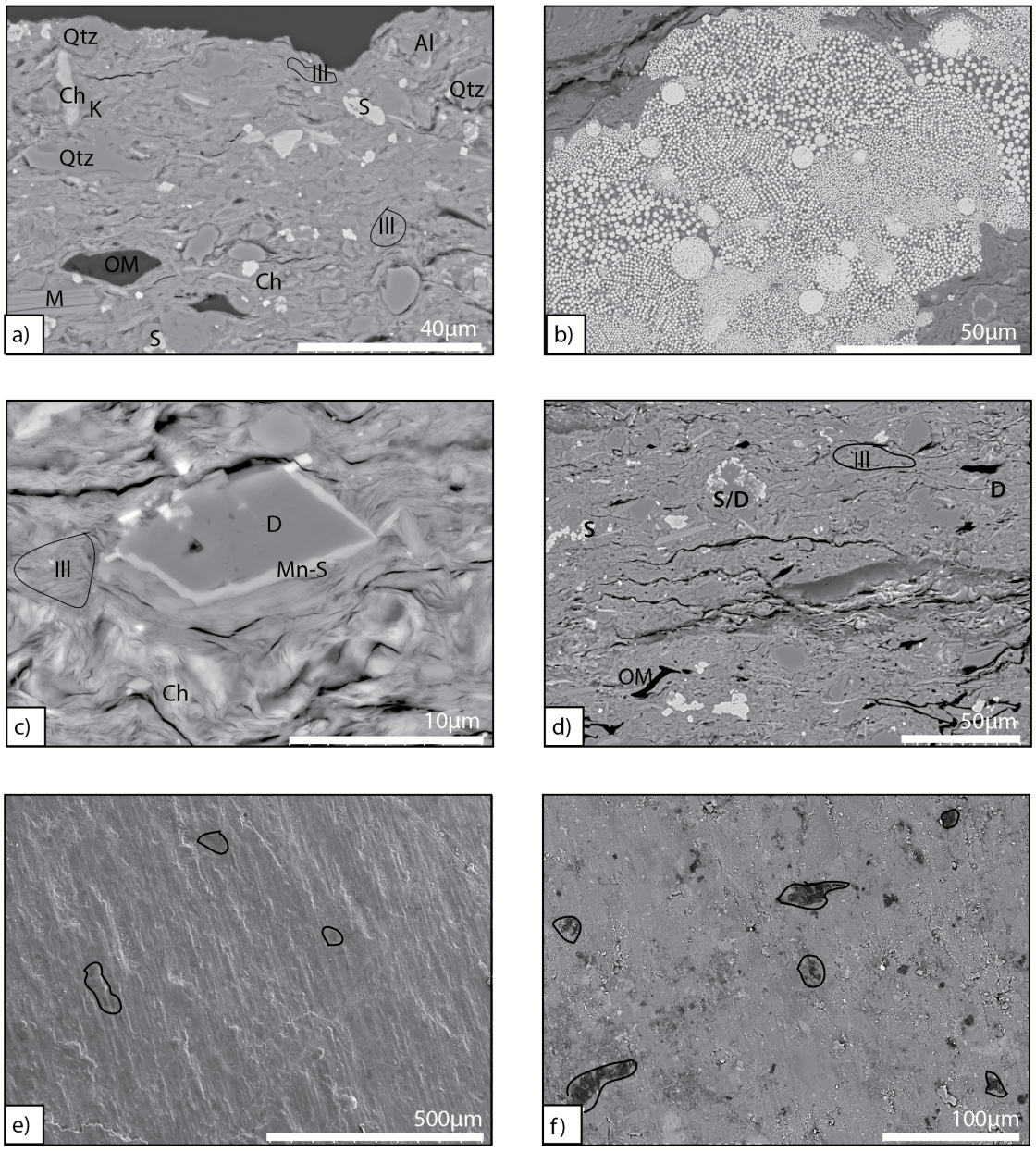

Figure 5.12: Distribution of minerals within sample S383. a-d) are from the sample cut parallel to the movement direction , e) and f) slip surface marked with black areas illustrating organic matter. Qtz - quartz, Ch - chlorite, OM - organic matter, Il - illite, Al - albite, D - dolomite, Mn-S - Mn-rich siderite. a-d) and f) are BSE images, and e) is SE-image.

5.4.3 Summary of mineralogy

SEM and XRD analyses show that illite/muscovite and quartz are the primary rock forming minerals. The carbonate composition observed differs, whilst siderite is observed in both samples from the SEM analysis it is only observed in sample S427 in the XRD analyses.

Illite acts as the matrix within both of the samples, while quartz makes up a large bulk of the rock in both of them. The same clay minerals are observed. Organic matter is observed within both samples, both within the matrix and along the slip surface, and may have been a controlling factor regarding the position and expression of the fractures.

The carbonate composition observed is the same for both samples, but the siderite seems more abundant in sample S383. Dolomite is more abundant within sample S427, where grain sizes are generally larger. Pyrite occurs with different characteristics in both samples. In sample S383 the pyrite is often found in clusters, whereas in sample S427, the pyrite is distributed evenly throughout. In both samples, the pyrite mainly exhibits a framboidal shape. The accessory minerals that are observed in smaller quanta differs between the two samples, where sample S383 has a more varied mineralogy than sample S427.

The Agardhfjellet Formation is calculated to have a higher BI than the Rurikfjellet Formation.

Chapter 6

Discussion

In this chapter, the results presented in Chapter 5 will be discussed in relation to the caprock potential of the Janusfjellet Subgroup (the Agardhfjellet and Rurikfjellet formations) in central Spitsbergen. Firstly, the deformation observed in the upper Agardhfjellet and lower Rurikfjellet formations i.e., dominant fracture orientation and deformation style will be discussed with regard to a regional tectonic context. This is followed by a discussion of the mineralogy of the Slottsmøya and Wimanfjellet members of the Agardhfjellet and Rurikfjellet formations respectively, and how it may have influenced the deformation style. The section concludes with an evaluation of the caprock potential of the studied succession.

6.1 Deformation in the upper Agardhfjellet and lower Rurikfjellet formations

The following section focuses on deformation observed in both the drill cores and outcrops. The dominant orientation observed is discussed in a regional context, and a conceptual structural development of the upper Agardhfjellet and lower Rurikfjellet formations is presented and based on data from fractures and meso-scale structures.

6.1.1 Fracture density and characteristics

The upper Agardhfjellet and lower Rurikfjellet formations are highly fractured. In the drill cores, 1172 fractures were measured and zones of crushed core were observed along

the 132 m examined in DH2 and DH4. In the outcrop, 370 fractures were measured along the 32 m studied. Ogata et al. (2014b) measured 870 fractures in the interval between 672 and 970 m in DH4, which is recognized to be the targeted reservoir rock for the Longyearbyen CO_2 Lab. This illustrates that slightly lower frequencies were observed in the reservoir unit.

The drill cores exhibit frequencies between 0 and 37 f/m, in which an interval of approximately 25 m displays the highest concentration of fractures in each drill core (Fig. 5.1). The lithologies recognized in the drill cores are mainly shale and silty shale, hence no specific lithological control on fracture distribution could be determined. However, the fractures have previously been recorded to be generally more abundant in the finer grained units in DH4 (Elvebakk, 2010). The scanlines obtained in field were collected along different beds of various lithological composition. The average amount of fractures were ranging from 5.6 f/m in the finer-grained units (shale) to 15.7 f/m in coarser grained units such as the silty shale (Tab. 5.1, Fig. 5.6). The maximum f/m is lower in shales than in the silty shale/fine-grained sandstone with 10 f/m to 15 f/m *vs.* 17 f/m to 25 f/m, respectively (Tab. 5.1). As such, lithology is considered to control fracture frequency observed in the outcrop.

The vertical scanlines obtained from the drill cores show a large proportion of low-angle fractures (approximately 60%, Fig. 5.3), whereas the lateral scanlines from the field exhibit 75.6% fractures with vertical to sub-vertical dips (70° to 90°) as seen in Figure 5.6. No fractures with dip angles lower than 38° were recorded in the field, due to the difficulty of distinguishing the difference between them and bedding planes. Ogata et al. (2014a) did a study of the fractures within the reservoir and caprock succession for the Longyearbyen CO_2 Lab, and reports both low-angle and high-angle fractures in the finer-grained units studied in the field. This suggests that low-angle fractures are also present in the interval examined in the study area, but due to weathered surfaces they could not be identified.

The fracture characteristics obtained from the drill cores reveal that large proportions (approximately 70%) exhibit polished surfaces with slickensides. These are typical for the low-angle fractures, which are therefore interpreted as shear fractures defined as Mode II (e.g., Schultz and Fossen, 2008; Fossen, 2010). This coincides with the interpretation of low-angle fractures in the drill cores by Ogata et al. (2014a), who argue that these were formed during the sub-horizontal contraction during the Paleogene. The open fractures with steeper dip angles and rough surfaces are consistent with Mode I (joints). Healed

fractures and mineralized veins were observed both in the field and drill cores, and are also interpreted to be Mode I fractures.

The differences observed between drill core and outcrop data can be attributed to differential decompaction, where the outcrops have experienced more uplift (approximately 600 m) than the strata present in the drill cores. This is also argued by Ogata et al. (2014a). Uplift causes fracturing by decreased confining pressure (Van Stappen et al., 2018). In addition, the location of the drill cores and the outcrop are situated at different parts of the CTB and have experienced different structural settings as of where they are situated according to the limb of the foreland basin (Fig. 6.1). Further, the outcrop is highly weathered and has gone through repeated freeze and thaw cycles, hence a bias to examine the more competent beds in the field needs to be accounted for as these beds can resist the mechanical weathering better.

6.1.1.1 Décollement zone in the Lower Cretaceous strata

The most intensely fractured intervals observed in the drill cores are arranged along or in close proximity to the boundary between the Agardhfjellet and Rurikfjellet formations (Fig. 5.1). Within this interval fracture frequencies of up to 37 f/m were observed. In addition, this zone corresponds to the intervals of crushed core. The fractures within this zone exhibit large proportions of low-angle fractures (Fig. 5.1), usually with a polished surface and slickensides. This zone is interpreted to be the thrust plane for a décollement along the boundary of the two formations.

In the field, the décollement zone can be recognized by crushed and highly weathered shale between sub-horizontal and less deformed bedding observed both above and below (Fig. 5.7, Fig. 5.8). This zone is interpreted to have affected the formation of the pop-up and duplex structures, by e.g., acting as a passive roof thrust. Décollement zones can transfer through thrust faults to weak layers higher up in the stratigraphy and act as sliding planes for the rock mass present, often as (sub-)horizontal horizons or slightly dipping towards the orogen (Cook and Varsek, 1994). This corresponds with observations done in the field.

Braathen et al. (2012) reported a décollement in the Upper Jurassic-Lower Cretaceous succession within the drill cores for the Longyearbyen CO_2 Lab. They observed higher fracture frequencies than what is observed in this study when using a televiewer, reaching 50 f/m in some intervals. The higher fracture frequencies observed by Braathen et al.

(2012) may be due to false measurements of drilling induced fractures and bedding, or related to the highly crushed zones where the televiewer estimated amount of fractures better than what was possible in this study. Braathen et al. (2012) further reports fault gouge within this zone, which can be related to the crushed zones observed in this study. The décollement zone is also described by previous studies e.g., Bergh and Andresen (1990) and Ogata et al. (2014a).

The presence of a thrust plane for the décollement zone in the middle of the studied interval is consistent with the highly fractured rock mass. Braathen et al. (2012) argued that the zone can be as thick as 180 m (between 370 m and 550 m depth), meaning that the décollement zone may encompass the entire interval studied in this contribution. Still, different vertical fracture frequencies were observed in this study, implying that the thrust plane may be situated where the most intensely deformed core was observed (at approximately 450 m to 475 m depth, and 392 m to 417 m depth in DH2 and DH4, respectively). This observation corresponds well with the results from Braathen et al. (2012), where the main thrust plane is reported to be at 455 m in DH2 and 402 m in DH4.

The most intensely deformed part of the core is interpreted to be situated at different depths within the two drill cores. This is due to the local dip caused by the formation of the WSFTB (Bælum et al., 2012). DH2 is situated closer to the collision zone, whereas DH4 is farther to the foreland and hence the same stratigraphic interval accumulating the strain is located further up closer to the foreland (Fig. 6.1).

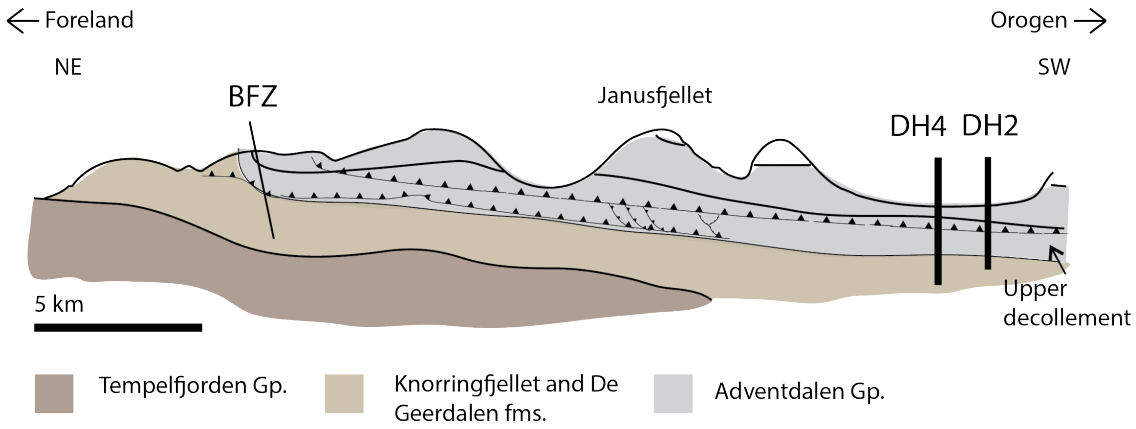

Figure 6.1: Schematic illustration of the décollement zone in field, and how the thrust structures observed is related to the different levels of the décollement. The décollement gently dips towards the orogen. Based on (Ogata et al., 2014b).

The density of fractures observed in both the drill cores and outcrop show that the Agardhfjellet and Rurikfjellet formations are highly fractured. Both sub-vertical and horizontal to sub-horizontal fractures are observed. The upper décollement zone reported by previous studies, e.g., Bergh and Andresen (1990), Braathen et al. (2012) and Ogata et al. (2014a) has slip surfaces situated in the middle of the studied interval of the cores. This highly fractured zone can also be observed in the field as black, crushed shale. This décollement zone is recognized to be a primary contributor to the deformation observed in this study.

6.1.2 Fracture sets and origin

Five high-angle fracture sets have been identified in this study. These fracture sets exhibit NNW—SSE (F1), NE—SW (F2), NW—SE (F3), ENE—WSW (F4) and NNE—SSW (F5) orientations (Fig. 6.2). The fracture sets measured are interpreted to be tectonic and diagenetic.

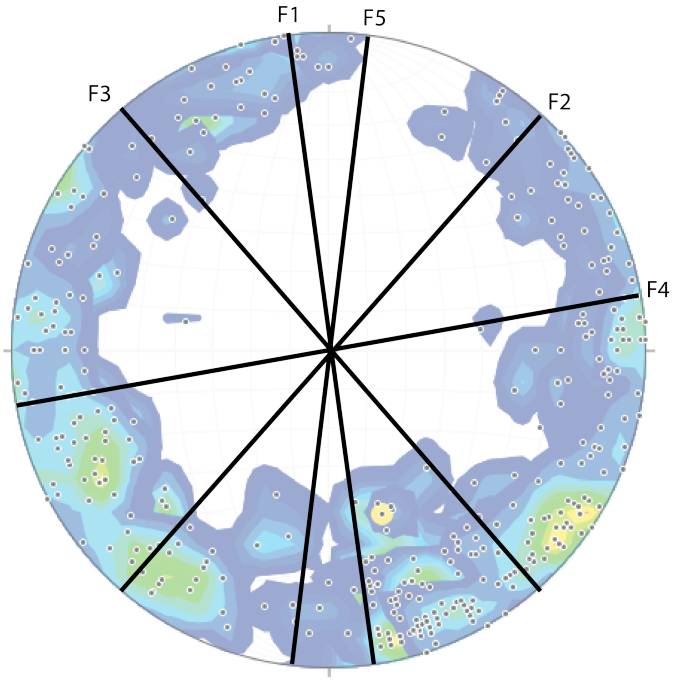

Figure 6.2: The five fracture sets displayed on a stereonet where all measurements have been plotted. The stereonet is made with a 1% contouring of the poles, and the color is reduced with 60% opacity.

F1 strikes NNW—SSE, with a mean strike of 352°. F1 is observed in four of the five scanlines and present in all the lithologies studied. This fracture set is observed in previous studies by Lord (2013) and Ogata et al. (2014a) in the De Geerdalen Formation and Schaaf et al. (2017) in the Agardhfjellet Formation. Ogata et al. (2014a) observed both joint sets and shear fractures oriented NNW—SSE, and concludes they are related to different stages of the formation of the WSFTB, and assigned this to the clockwise rotation of the horizontal contraction where the main stress orientation rotated from approximately NE—SW to ENE—WSW. In addition, the major structures of the WSFTB is parallel to F1 (Braathen et al., 1999) as seen by the major lineaments along the west coast of Spitsbergen. F1 is therefore interpreted to have formed as a joint set, related to the formation of the WSFTB.

F4 trends ENE—WSW with a mean strike of 72° and is present in all lithologies. This fracture set has been documented in the Triassic and Jurassic strata (Lord, 2013; Ogata

et al., 2014a) and in the dolerite intrusions (Festøy, 2017). It is therefore considered to be regional. The stress regime forming the WSFTB had a SW—NE orientation (Bergh et al., 1997). Healed fractures and veins exhibiting similar trends have also been observed in the study area as referred to by previous publications (Ogata et al., 2014a). Assuming that the main joint sets of central Spitsbergen, which are interpreted to be regional, are aligned parallel to the WSFTB, the E—W to ENE—WSW trending sets are interpreted to be a product of this stress regime (Ogata et al., 2014a). Maher et al. (2020) states that ENE—WSW fractures in central Spitsbergen have an origin from the HALIP event, which imply that previously formed fractures within this set were reactivated during the Paleogene.

F5 is mostly observed in the fine-grained sandstone beds (KW5), but some fractures with this orientation were also observed in the silty shale (KW3 and KW4). This fracture set has a mean strike of 12°. Scanlines KW3 and KW4 were obtained some few meters away from the pop-up structure observed in upper Konusdalen West, where the antithetic fault (as described in Section 5.2.1) also display this orientation. This fracture set was also observed further down-section by Ogata et al. (2014a) as a subordinate joint set. F1 and F5 and strike approximately parallel to the major fold axes of the WSFTB (Braathen et al., 1999), and is therefore argued to be related to fracturing during migration of detachment folds (Ogata et al., 2014a) during the Paleogene transpression.

F2 and F3 are observed within all lithologies studied, and have also been observed in previous studies, e.g., Lord (2013), Ogata et al. (2014a) and Schaaf et al. (2017). These fracture sets show a cross-cutting relation. They can be considered regional, but are not prominent. Ogata et al. (2014a) defines these two sets as high-angle, conjugate shear fractures and relate them to contraction during Paleogene. Assuming this interpretation is consistent with the fracture sets observed in this study, F2 and F3 can be conjugate shear fractures formed during the same conditions as the joint set seen in F4. F2 and F3 are hence formed oblique to the contractional stress.

Maher et al. (2020) also argues that the N—S (F1 and F5 herein) trending fractures may have a HALIP origin. NNW—SSE oriented sets are also argued by Lord (2013) to have originated from the Cretaceous extension and uplift. In addition, tectonic activity along reactivated, prominent structural lineaments on Spistbergen (Lord, 2013) need to be considered. The proximity of the study area to the Billefjorden Fault Zone (BFZ) means that the deformation can have been affected by reactivation of these lineaments. Some of the fractures observed in this study are therefore interpreted to have been formed during the Cretaceous, before being re-activated at a later stage.

6.1.3 Meso-scale structures

In the outcrops studied at Deltaneset (Fig. 4.2), multiple contractional structures were observed. The meso-scale structures are interpreted as pop-up and duplex structures. These are typical for the frontal parts of a fold-and-thrust-belt system which is relatively weakly deformed compared to the more central part of the collision zone (Boyer and Elliott, 1982; McClay, 1992). Fault propagation folds were observed up-section further up Janusfjellet (Fig. 4.2, Fig. 5.10), and is characteristic of the contractional regime during the Paleogene.

The faults comprising the pop-up structure exhibits NNW—SSE to NW—SE and NE—SW orientations, with dip directions towards the (W)SW and NW respectively (Fig. 5.7). The two fault segments dip in opposite directions, converging towards each other, and as a result of the thrust movement a block has been displaced upwards between them. In addition, a duplex structure were observed to the east of the pop-up structure (Fig. 6.3). The orientations of the thrust faults comprising the duplex structure is NNW—SSE, with dip angles towards the SW/WSW. The eastern segment of the pop-up and the faults within the duplex show orientations consistent with Bergh et al. (1997), typically seen in what they refer to as the eastern zone of the WSFTB. The two structure systems are therefore interpreted to have been formed during the Paleogene contraction. As such, the pop-up and duplex structures are hinterland dipping, with the antithetic fault of the pop-up structure formed as a back-thrust. Typical for duplexes is that they are created with a forward progression of thrusting (Boyer and Elliott, 1982), and the observed duplex hence formed with a progression towards the NE.

The thrust structures such as the pop-up structure and duplex that have been observed are typical for thin-skinned fold-and-thrust belts. The boundary between the Agardhfjellet and Rurikfjellet formations is interpreted to be just above the two mapped structures. The discussed décollement zone is interpreted to be along this boundary (or in close proximity to it), and acts as a roof thrust for the duplex, whilst during the formation of the pop-up structure it could not have been active. The pop-up is observed to not be affected by the décollement, hence it is not interpreted to have been active during the formation of this structure. It is therefore assumed that there is a difference between the relative timing of these two systems.

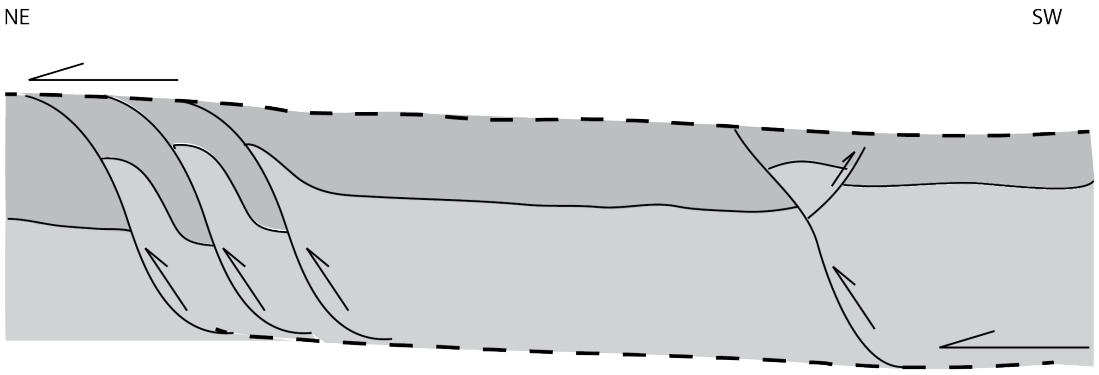

Figure 6.3: Schematic illustration of the thrust structures present, not to scale. The dashed lines indicate different levels of the décollement zone present, the arrows indicate direction of movement.

The thrust fault structures show steeper dip angles than for typical Andersonian faults, i.e., 45° or lower (e.g., Anderson, 1905; Fossen, 2010). The continuous deformation as a result of the Paleogene contraction resulted in a long deformation phase. Shortening of the strata after the thrust structures were formed can have led to steepening of faults (McClay and Insley, 1986). Previous studies, i.e., Bergh et al. (1997) and Braathen et al. (1999) reported steeply dipping reverse faults related to the WSFTB, and concludes that Paleogene contraction deformed the strata in multiple stages, including both contraction and strike-slip movement.

The fault propagation fold (FPF) is typical for a contractional regime, and can be observed in any part of a fold-and-thrust-belt. The observed FPF in the study area has a plunge towards NNW, and hence exhibit orientations that are consistent with other features in the WSFTB (Bergh et al., 1997) such as thrust faults and folds. As a response to the thin-skinned shortening of the Svalbard strata during the evolution of the WSFTB, upright and disharmonic folds formed in the incompetent shales above the Gipshuken décollement (Bergh et al., 1997). In the eastern zone of the fold-and-thrust-belt, where the succession targeted in this study is situated, folds have been recorded to display fault-bend fold geometries (Bergh et al., 1997). This is consistent with the findings in this study.

Normal faults have been mapped in the lower Agardhfjellet Formation further down-section in lower Konusdalen West (Nakken, 2020), with NE—SW orientation. These structures are situated approximately 150 m down-section from the contractional features ob-

served in this study. The different tectonic expressions may imply a decoupling between two levels of the décollement due to differential movement. Braathen et al. (1999) also report normal faults in the coal mines in central Spitsbergen, which they associated with tensional fractures that formed parallel to the shortening axis during the Paleogene transpression. A different interpretation of this normal fault system suggest they formed due to local extensional zones, as a result of differential loading during the formation of the WSFTB in the contractional regime (Ogata et al., 2014a). The presence of both extensional and contractional features testifies to multiple stages of the Paleogene event, where space issues caused differential deformation.

The σ_1 of the Paleogene contractional event has an orientation from the SW, implying that the duplex and pop-up structures are aligned with the transport direction of the stress field related to this event. In general, the fold-and-thrust-belt strikes NNW—SSE. The WSFTB is dominated by transport directions perpendicular to the orogen (Bergh and Andresen, 1990; Wennberg et al., 1994; Bergh et al., 1997). In addition, the duplex suggests a transfer of slip from a deeper slip surface to the one recognized above as the upper décollement zone.

6.1.4 Summary of how the tectonic events relate to the observed structures

The tectonic events that has affected the Janusfjellet Subgroup after deposition can be summarized as three main events (Fig. 6.4). The understanding of the tectonic influence is based on the major tectonic events Svalbard has gone through, as described in Section 3.1.3, and how they can relate to the interpretation of the data sets obtained from the drill cores and outcrops. The understanding of how the tectonic events have affected the upper Agardhfjellet and lower Rurikfjellet formations is based on previous models made by Ogata et al. (2014a).

During the Early Cretaceous, NW—SE oriented seafloor spreading in the Arctic Ocean caused volcanic activity (e.g., Tarduno et al., 1998b). This also led to development of the High Arctic Large Igneous Province where central Spistbergen was intruded by igneous sills and dykes (e.g., Tarduno et al., 1998b; Senger et al., 2013). The magmatic activity led to an increased heatflux which resulted in an uplift of up to 1 km in the northern parts of Spitsbergen (Dallmann, 1999; Dallmann et al., 2015). This uplift may have generated additional fracturing by decompacting the strata and decreasing the confining pressure. Uplift also affected the pre-existing BFZ, and likely formed fractures with preferential ori-

entations to this zone (Harland, 1997; Maher et al., 2020) such as e.g., F1 and F5. The main stress fields during the Cretaceous magmatic event are reported to be NW—SE and NE—SW based on emplacement of sills and dykes, and hence fractures oriented preferential to this (e.g., F2 and F3) may also have been formed in the upper Agardhfjellet and lower Rurikfjellet formations (Senger et al., 2013).

Paleogene transpression is interpreted to have formed the majority of fractures and meso-scale fault systems observed in this study (Fig. 5.5, Fig. 5.7, Fig. 5.8). The opening of the North-Atlantic, and associated dextral movements resulted in the transpression that formed the WSFTB (Bergh et al., 1997; Braathen et al., 1999). The orogen that formed due to this is oriented in a NNW—SSE direction. The majority of the fracture sets observed in this study are interpreted to have been generated by this event, where F1 and F5 are oriented sub-perpendicular to the σ_1 and F4 is oriented sub-parallel to σ_1. The sub-horizontal contraction formed shear fractures and associated conjugate fracture sets (Ogata et al., 2014a), as F2 and F3 are interpreted to be. The meso-scale thrust structures are formed in relation to a σ_1 from the SW, and also exhibit orientations consistent with the major thrusts formed during this event (Bergh et al., 1997; Braathen et al., 1999).

Further development of the fracturing occurred due to the uplift and unloading during the Cenozoic (Dörr et al., 2013; Dallmann et al., 2015). Reactivation of especially the high-angle joints present may be attributed to this event. During the Quaternary, glaciation and deglaciation have contributed to erosion and further unloading of the strata (Ogata et al., 2014a). In the outcrops, weathering and freeze/thaw cycles can also have effected the presence of fractures (Tharp, 1987). The frigid climate in the high Arctic where Svalbard is situated is consistent with these processes (Mulrooney et al., 2019).

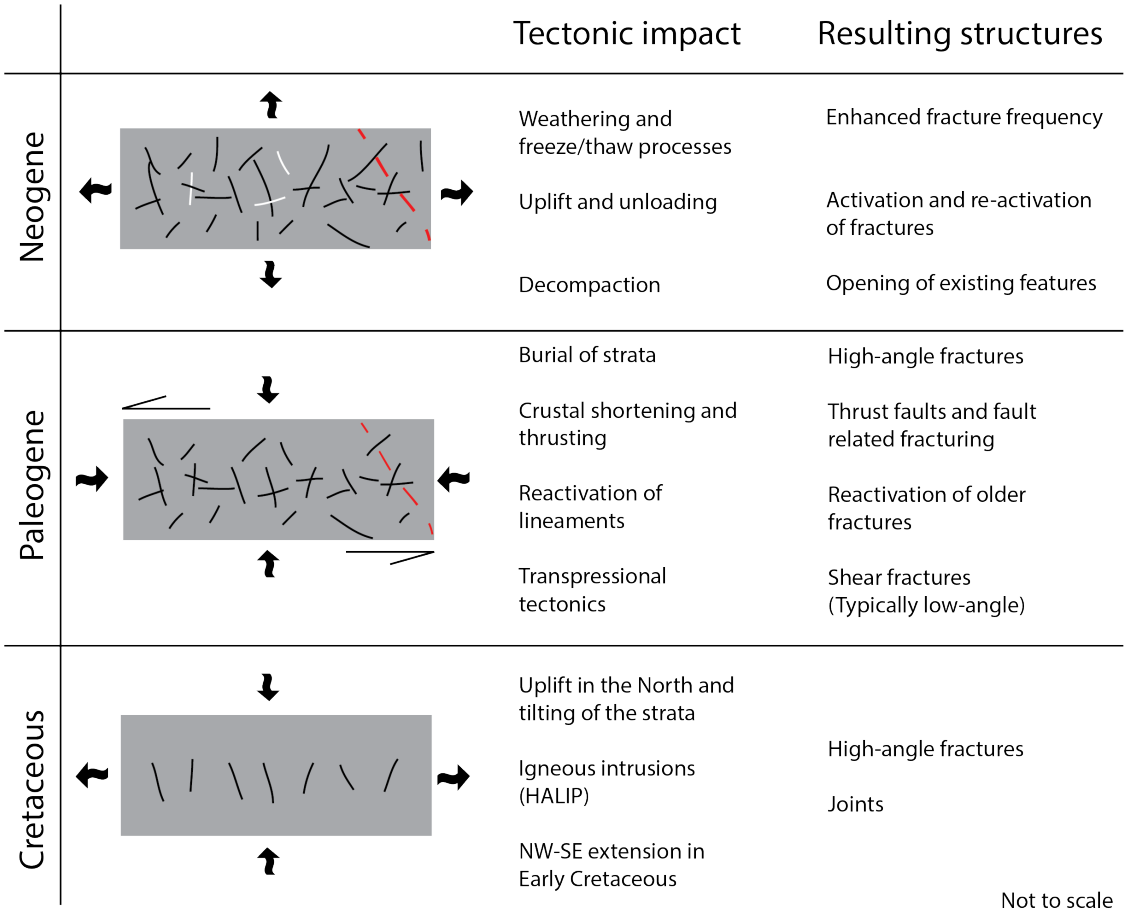

Figure 6.4: Tectonic events related to the deformation observed. Red, dashed lines illustrates thrust faulting, black lines indicate fractures and the white lines indicate mineralized fractures. Further explanation of the tectonic events is found in the text. Based on Ogata et al. (2014b).

6.2 Mineralogy of the upper Agardhfjellet and lower Rurikfjellet formations

In this study massive shale units with some inter-bedded siltstone and sandstone were observed throughout the upper Agardhfjellet and lower Rurikfjellet formations (Fig. 5.6). Dypvik (1984) described the upper Agardhfjellet Formation as a homogeneous, massive shale succession, and the lower Rurikfjellet Formation as mainly consisting of grey shales.

The previous descriptions match observations done in this study.

The results from the XRD and SEM analyses herein show typical shale composition (e.g., Gale et al., 2014), with constituents such as clay minerals, quartz, feldspar, pyrite, and carbonates (Tab. 5.2). This study concludes that clay minerals are the main constituents comprising the two formations, with 52.1% and 35.3% in the Rurikfjellet and Agardhfjellet formations respectively. The clay minerals observed are illite, kaolinite and chlorite. Dypvik (1984) lists the same clay minerals in addition to smectite. Quartz is the second most abundant mineral, with approximately 24% for both formations. In the shales of the Janusfjellet Subgroup, Dypvik (1984) also recorded quartz, feldspar, pyrite and siderite which is consistent with the findings in this study (Tab. 5.2).

Clay minerals and organic matter in shale can result in more ductile deformation (Gale et al., 2014), as is seen in the black shales of the Rurikfjellet Formation adjacent to the more competent fine-grained sandstone beds (Fig. 5.9). However, the high fraction of quartz can explain the brittle behavior of the Agardhfjellet and Rurikfjellet formations, as high silica content is reported to cause the rock to act in a more brittle way (Gale et al., 2014). It is also argued that high clay content can result in brittle deformation if catagenesis has occurred (Rodrigues et al., 2009).

Organic matter is observed within the matrix of the Agardhfjellet and Rurikfjellet formations and is distributed throughout the samples (Fig. 5.12, Fig. 5.11). A total amount of 12% TOC has been recorded in the upper Agardhfjellet Formation, but decreases to about 1.5% to 2% towards the top of the Slottsmøya Member (Dypvik, 1984; Koevoets et al., 2018). The organic matter was also present along the fracture surfaces. This indicates that organic matter causes zones of weakness, and can control where fractures occur. It is important to note that the fracture surfaces studied herein were polished with slickensides, and the results may therefore primarily apply to surfaces with these characteristics.

Previous studies (e.g., Dypvik, 1984; Olaussen et al., 2019), reported smectite in the upper Agardhfjellet Formation. This does not match the results of this study, where no other indicators except an illite/smectite transition phase was observed. The previous studies report bulk XRD findings from samples collected in the field. This can be a reason for the contradicting findings. A higher content of illite or an absence of smectite can be related to the degree of burial (Shaw and Primmer, 1991). Illite is typical for deeper burial and a higher degree of diagenesis. The Agardhfjellet and Rurikfjellet formations has gone through at least 3 km of burial (Marshall et al., 2015a), as such the smectite is not expected to present. For the Longyearbyen CO_2 Lab, Olaussen et al. (2019) report that the

smectite, being a swelling clay, contribute to the sealing factor of the décollement zone. The results from this thesis imply that the smectite is not present in the sub-surface part of the formations, hence the sealing property of this mineral can not be relied on here.

The most prominent differences between the two studied formations are the carbonate content, and different amount of clay minerals present. The different mineral composition does not seem to affect the fracture frequency or dip angle as the samples from each formation is gathered in intervals of relatively similar fracture patterns (Fig. 5.1, Fig. 5.3). However, the large difference in abundance of clay minerals implies that the Rurikfjellet Formation can exhibit a more ductile deformation style than the Agardhfjellet Formation, due to the high clay mineral content (Gale et al., 2014). This can be seen by the presence of FPF and small-scale folding in the Rurikfjellet Formation (Fig. 5.10).

Further, the BI for the Rurikfjellet Formation is calculated to be lower than the one for the Agardhfjellet Formation. As stated by equation 5.1, the BI decreases with increasing clay content (Guo et al., 2013). This index indicates the ability of the rock to fracture (Wang and Gale, 2009). As such, the fracture frequencies should be lower in the Rurikfjellet Formation than in the Agardhfjellet Formation, which is not observed in this study. Both formations exhibit high fracture frequencies.

6.3 Implications for fluid flow and caprock properties

This section shortly considers the implications of the results herein for fluid flow and caprock properties of the upper Agardhfjellet and lower Rurikfjellet formations.

6.3.1 Implications for fluid flow

The Janusfjellet Subgroup mainly consists of shales, and is regarded as a low porosity and permeability rock with high tensile strength (Bohloli et al., 2014). The porosity of the succession is approximately 2% to 3% (Alemu et al., 2011). The frequency and orientation of the fractures within the caprock interval is therefore important to map when considering the possible fluid flow.

The presence of natural fractures and other meso-scale discontinuities in the upper Agardhfjellet and lower Rurikfjellet formations can contribute to positive (e.g., increase permeability by acting as conduits) or negative (e.g., act as barriers/baffles) conductivity (e.g., Laubach et al., 2019; Ogata et al., 2014b; Aplin et al., 1999). Mulrooney et al. (2019)

states that some of the discontinuities mapped in the underlying De Geerdalen Formation (the targeted reservoir rock for the Longyearbyen CO_2 Lab) can act as baffles for fluid flow and are tentatively credited for lack of pressure communication between wells during injection and leak-off tests. For a fault to act as a conduit in shale-dominated successions, it is preferential that the faulting is active (Aplin et al., 1999). The presence of an active tectonic setting or an increase of stress may therefore be important for the discontinuities to act as conduits, whereas an inactive setting can mean that the discontinuities act as baffles for fluid flow. Currently, Spitsbergen is assumed to be an area with little tectonic activity, which indicates a preferential regime for closing of the observed fractures.

The intersection of multiple fracture sets with different trends can create connectivity (Gale et al., 2014). Fractures observed in this study are oriented perpendicular and oblique to each other, and they are observed to have a cross-cutting relationship which can imply preferential fluid flow pathways (Fig. 6.5). The amount of sub-horizontal fractures observed in the core imply a bed-parallel flow, whereas the high amount of sub-vertical fractures show that the fluids may migrate vertically too. However, the aperture size is relevant for CO_2 to flow. With an aperture below the critical value, the fluid will not flow (Edlmann et al., 2013). The permeability of the rock caused by fractures are important for fluid flow. The apertures of the fractures within this study are interpreted to be small (mm scale). Permeability measurements conducted on the reservoir rock in DH4 indicate that an increase in confining pressure will lead to a partial closure of the fractures within the rock (Van Stappen et al., 2018). Some fractures experienced as much as 40% closing of the original aperture size, causing a 90% drop of permeability, due to confining pressure (Van Stappen et al., 2018). These findings are from a greater depth than where the Agardhfjellet and Rurikfjellet formations are located, but the confining pressure acting on these formations is also here assumed to reduce permeability due to the overburden pressure from approximately 400 m of strata. Further, the presence of mineralized and healed fractures act as barriers, as they terminate fluid flow where they intersect with the open fractures (Fig. 6.5).

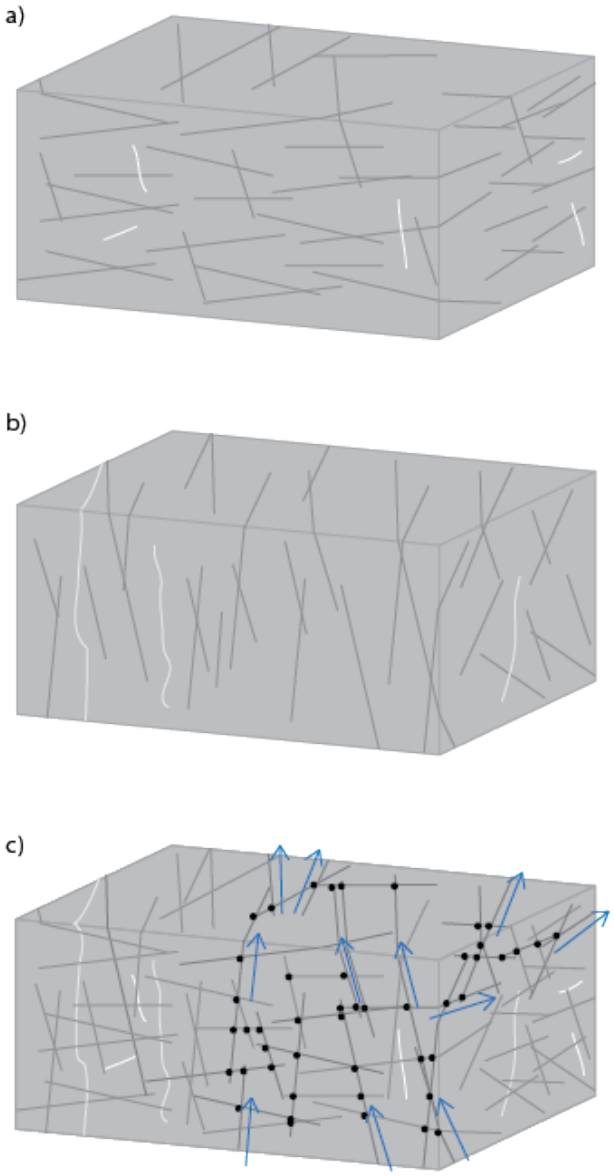

Figure 6.5: Schematic illustration of how the fractures are connected, and what implications this have for fluid flow. a) fractures in the drill cores, mainly consisting of sub-horizontal fractures and some high-angle fractures, b) fractures measured in field based on KW3, where the dominant fracture sets are F1 and F4, c) combination of fractures in the cores and in the outcrop to see how fluids may migrate. Grey lines indicate fractures, white lines indicate mineralized and healed fractures, and blue arrows indicate fluid flow pathways along the connected fractures where intersection points are marked with black circles.

The ductile deformation observed in the black shales (Fig. 5.9) can act as barriers for fluid flow, and trap the CO_2. The folds forms a small, structural trap. However, the formation of folds often result in fracturing of the fold limbs, which can allow for fluids to flow.

The large amount of low-angle fractures observed in the drill cores and the presence of a sub-horizontal thrust plane can indicate flow along the beds rather than across (Fig. 6.5). Previous studies have shown that the permeability caused by fractures across and perpendicular to bedding is limited (no more than 30 mD) compared to fracturing parallel to bedding which can be as much as 300 mD (Carey et al., 2015).

6.3.2 Caprock potential of the upper Agardhfjellet and lower Rurikfjellet formations

The analyses of the mineralogy within the upper part of the Agardhfjellet and lower part of the Rurikfjellet formations conducted show an illite-matrix supported rock with low porosity, as is previously stated by Dypvik (1984) and Alemu et al. (2011). The targeted caprock succession for the Longyearbyen CO_2 Lab has a thickness of more than 400 m (Dypvik et al., 1991; Braathen et al., 2012). The time-equivalent Hekkingen and Fuglen formations in the Barents Sea act as functional caprocks today (Gabrielsen and Kløvjan, 1997). However, the intensely fractured and deformed succession present onshore Svalbard may compromise this.

The major uncertainty of the Upper Jurassic-Lower Cretaceous succession, the Janusfjellet Subgroup, in central Spitsbergen is the intensely fractured rock mass. Natural fractures have been proven to increase the permeability in the targeted reservoir rock below the Agardhfjellet Formation (Braathen et al., 2012; Ogata et al., 2014b; Senger et al., 2015). Faults in the reservoir rock have also proven to act as baffles when it comes to fluid flow between two of the boreholes (DH7 and DH5R) located close to DH4 (Mulrooney et al., 2019).

The décollement zone with crushed intervals present in the studied succession is assumed to be a contributing factor to the sealing property of the Janusfjellet Formation. Braathen et al. (2012) reported fault gouge along the thrust plane, that can act as a membrane. The high clay content recorded in this study can contribute to the sealing factor the gouge has.

The fractures in this study shows connectivity, and are both sub-vertical and sub-

horizontal. This indicate possible fluid flow both laterally and vertically (Fig. 6.5). However, the presence of mineralized and healed fractures results in prevention of fluid flow at some intersections. Veins have been identified to work as baffles for fluid flow (Gale et al., 2014). The low lateral resolution of the drill cores results in a bias towards the low-angle fractures and high-angle veins may have been missed and is therefore assumed to be more present than observed.

Injection of CO_2 into the subsurface leads to increased pore pressure and reduced effective stress, hence the likelihood of exceeding the capillary entry pressure of the caprock will increase (Edlmann et al., 2013). Bohloli et al. (2014) conclude that the high tensile strength of the Agardhfjellet and Rurikfjellet formations combined with the pre-existing fractures implies that further fracturing is unlikely to occur. In addition, the low pressure measured in the reservoir formation (30 bar to 50 bar) gives a significant pressure margin when the maximum tolerated pressure has been calculated to approximately 170 bar (Bohloli et al., 2014).

The current stress field affecting Svalbard has a SW—NE orientation (M. Jochmann, pers. comm), which is perpendicular or sub-perpendicular to some of the fracture sets observed (F1 and F5). Within the mines in central Spitsbergen, the horizontal stress is measured to be significantly greater than the vertical stress (M. Jochmann, pers. comm). This can affect the fractures by keeping them closed during this stress regime. Studies from the Snorre Field in the North Sea show how fractures in the caprock re-opened due to the current stress directions. Along these fractures, leakage occured (Caillet, 1993). If the current stress fields remain stable, several of the observed fractures are assumed to be closed. As such, they will prevent fluid flow.

Vertical pressure differences recorded in the targeted CO_2 storage succession, between the reservoir and overburden, show that the caprock has a sealing property, at least on a thousand year scale (Huq et al., 2017). The underpressure recorded in the reservoir rock testify to this (Olaussen et al., 2019).

The samples examined (S383 and S427) are clay-rich, with low presence of carbonates. A caprock can act as an active participant regarding storing CO_2, by e.g. trapping the CO_2 into stable mineral forms (Zhang and Song, 2014; Alemu et al., 2011). Alemu et al. (2011) observed that the clay rich shale experienced less reaction with the injected CO_2 than the carbonate rich clay. Still, the Ca-rich minerals (e.g., carbonates) can react with the injected CO_2 causing permanent trapping within stable minerals (Alemu et al., 2011). For the clay-rich shale, the alteration of porosity due to injection of the fluid does not seem very likely

(Alemu et al., 2011). The CO_2 reacting with material present in the rocks have also been recognised by Song and Zhang (2013) to contribute with trapping of the minerals. The presence of carbonates in the studied interval is limited, but may still play an active role meaning that if some CO_2 were to leak into the Agardhfjellet and Rurikfjellet formations, the caprock may participate as a trap.

An important aspect as to why the Janusfjellet Subgroup has a caprock potential is the thickness of the succession (approximately 450 m). Thick caprocks perform as better hydraulic seals (Song and Zhang, 2013). The confining pressure caused by the overburden is proven to close fracture apertures, and reduce permeability resulted by the presence of fractures (Van Stappen et al., 2018).

As stated previously, the presence of smectite has been regarded as to increase the seal capacity of the caprock interval based on samples from various outcrops in central Spitsbergen (Olaussen et al., 2019). The absence of this mineral in the drill cores makes its occurrence in the subsurface uncertain.

The results discussed herein show that the targeted caprock succession is highly fractured, with interconnected prevalent fracture sets that may promote fluid flow. However, pressure differences between the targeted reservoir and caprock for the Longyearbyen CO_2 Lab suggest a sealing caprock. The reason for this is not fully understood, but could be due to several observations:

- The thickness of the succession results in a permeable barrier (Song and Zhang, 2013). The confining pressure as a result of 400 m of overburden can reduce the permeability caused by the fractures (Van Stappen et al., 2018). The sub-horizontal shear fractures observed may have preferential orientation and properties for the confining pressure to close them.

- The upper décollement zone acts as a horizontal baffle, where membranes composed of mainly clay-rich shale reduce the pore throat size. Décollement zones have previously shown to act as barriers to vertical fluid migration (Tobin et al., 2001).

- The mineralogical composition is preferential, with clay minerals that can form clay cement and shale gouge (Song and Zhang, 2013). Clay minerals can also affect the fracture closure (Van Stappen et al., 2018).

- The current SW—NE oriented regional stress is preferential for the fractures to close, by being parallel or sub-parallel to the some of the dominating fracture sets (e.g., F4).

6.4 Limitations of the study

The results are based on subjective gathering and interpretation of the studied material. This introduces uncertainties and limitations to the data sets.

Both data acquisition in the field and from the drill cores can be affected by sampling bias. Uneven surfaces, fractures not oriented perpendicular to the rock faces, poor measurements and omitted surfaces affect the results negatively. The outcrops were in some places scree-covered and highly weathered, which made the acquisition of data challenging. The presence of beds for scanline construction was limited, and resulted in fewer and shorter scanlines than optimal. The scree covered, weathered outcrops made the distinction between bed-confined and through-going fractures difficult resulting in a reduced data set which would be helpful in understanding fluid flow characteristics of the succession.

For the drill core data, the difference between drilling induced and natural fractures may have been misinterpreted. In addition, the vertical drill cores have a natural bias towards intersecting horizontal fractures and hence have a low lateral resolution (Gale et al., 2014).

The results of the mineralogy are based on analyses of only two samples which provides limited, but useful understanding of the composition of the two members.

The field campaigns of 2018 and 2019 were shortened due to polar bear encounters, resulting in evacuation of the field camps. This limited the amount of field days from the planned 21 days to 14 days, and hence the amount of data collected from the outcrops were reduced accordingly.

6.5 Future research opportunities

In this study, the deformation present in the upper Agardhfjellet and lower Rurikfjellet formations has been investigated with a main focus on the fracturing. The mineralogy of the formations has also been examined to understand if any correlation is found between the fracturing and mineralogy present. The results show indications of how this can be related to the caprock potential of the studied succession, but more research should be done to form an even more comprehensive understanding. Suggestions for further work:

- Form a better understanding of the current stress regime, and how it may affect the

deformation present related to fluid flow pathways. A model of the fractures based on the in-situ stress should be constructed to determine likeliness of reactivation. An important investigation would be to map if the fractures are currently open or closed, and how they are related to in-situ stress.

- The mineralogy within the caprock can have an important control on sealing properties. The presence of smectite has been listed as one of the sealing factors within the Agardhfjellet and Rurikfjellet formations. The absence of the mineral within this study suggests that the sealing effect of the succession results from something else. It is therefore recommended that more mineralogical analyses of the caprock succession should be conducted to improve the understanding of the sealing properties of the rock.

- An investigation of the microstructures present should be conducted. The geomechanical properties of shale is a function of the mineralogy and microstructures (Guo et al., 2013), hence an investigation of the microstructures will increase the understanding of the geomechanical properties of the Agardhfjellet and Rurikfjellet formations.

- The contractional features mapped in the field are just a few out of many such features present in the lower part of Janusfjellet. The mapping of these structures in this study focused on the orientation of the thrust faults. Further structural studies of the fault structures locally here will enhance the understanding of the presence of contractional features in the Agardhfjellet and Rurikfjellet formations.

- A discrete fracture model should be made including the data collected for this study combined with previous studies of the reservoir-caprock succession for the Longyearbyen CO_2 Lab. This could increase the understanding of fracture connectivity and permeability, and help optimize rates of CO_2 injection.

Chapter 7

Conclusion

This study integrates drill core and outcrop data collected in central Spitsbergen in order to investigate the natural fracture network in the upper Slottsmøya member of the Agardhfjellet Formation and the lower Wimanfjellet Member of the Rurikfjellet Formation. In addition, the mineralogy above and below the boundary between the two members has been studied. This work has been carried out in order to investigate the caprock integrity of the studied interval. The following conclusions have been made:

- Highly fractured zones within the studied interval suggest that a decollément zone is present, with slip surfaces interpreted to be along the boundary between the Agardhfjellet and Rurikfjellet formations. This zone has been a dominating factor for the fracturing within the aforementioned succession.
- The fractures in the upper Slottsmøya Member and lower Wimanfjellet Member can be classified as five high-angle fracture sets striking NNW—SSE, NNE—SSW, NE—SW, NW—SE and ENE—WSW. These sets were formed during three main events. The first important event occurred during the Cretaceous, where uplift and extension created decompaction related fracturing and joints. Secondly, Paleogene transpression forming the WSFTB is assumed to be responsible for the majority of fractures that were encountered in this study. Both joints and shear fractures were formed due to this event. The last event is associated with decompaction as a result of deglaciation and erosion in the Quaternary.
- The connectivity of the fractures within the lower Agardhfjellet and upper Rurikfjellet formations imply that there is pathways for fluids to flow. The flow may happen

both vertically and horizontally along beds. Veins and healed fractures terminate the flow when intersecting with the open fractures. The sampling bias of the cores limits the mapping of the veins, which are assumed to be more abundant than what is observed in this study.

- Several contractional thrust structures are observed in addition to the décollement zone. These structures have been interpreted to be related to the Cenozoic transpressional event, with orientations consistent with large fold and fault structures related to the WSFTB. The structures mapped suggests that the study area is located in the frontal part of the fold-and-thrust-belt system.

- The mineralogy of the upper Slottsmøya Member of the Agardhfjellet Formation and the lower Wimanfjellet Member of the Rurikfjellet Formation show typical shale composition. The clay content is higher in the Wimanfjellet Member, and comprises more than half of the total mineral occurrence. The Agardhfjellet Formation, on the other hand, has a clay content of approximately one third of the total mineral content. The difference in fractions of clay minerals does not seem to affect the fracture frequencies within the studied interval, but ductile deformation seems more abundant in the Rurikfjellet Formation.

- The clay XRD reveals that there is no smectite in the studied samples. This indicate that the previously reported swelling clays are absent in the subsurface part of the studied interval. The core data from this study is assumed to be more reliable than previous field work studies on the mineralogy content.

- The Janusfjellet Subgroup, which consists of the Agardhfjellet and Rurikfjellet formations, is regarded to be a functional caprock for the Longyearbyen CO_2 Lab. The reason for it being functional can be assigned to a combination of the thickness of the succession, preferential current stress closing the fractures present, high fractions of clay minerals, as well as the presence of a décollement zone.

References

Alemu, B. L., Aagaard, P., Munz, I. A., and Skurtveit, E. (2011). Caprock interaction with CO2: A laboratory study of reactivity of shale with supercritical CO2 and brine. *Applied Geochemistry*, 26(12):1975–1989.

Allmendinger, R. W., Cardozo, N., and Fisher, D. M. (2011). *Structural geology algorithms: Vectors and tensors*. Cambridge University Press.

Andersen, E., Davey, H., Steinhoff, C., and Davis, T. (2013). Investigating the relationship between microseismic events and geomechanical variations in the Montney Shale reservoir–a case study. *First break*, 31(2).

Anderson, E. M. (1905). The dynamics of faulting. *Transactions of the Edinburgh Geological Society*, 8(3):387–402.

Andresen, A., Haremo, P., Swensson, E., and Bergh, S. G. (1992). Structural geology around the southern termination of the Lomfjorden Fault Complex, Agardhdalen, east Spitsbergen. *Norsk Geologisk Tidsskrift*, 72(1):83–91.

Aplin, A. C., Fleet, A. J., and Macquaker, J. H. (1999). Muds and mudstones: Physical and fluid-flow properties. *Geological Society, London, Special Publications*, 158(1):1–8.

Bælum, K., Johansen, T. A., Johnsen, H., Rød, K., Ole Ruud, B., and Braathen, A. (2012). Subsurface structures of the Longyearbyen CO 2 Lab study area in Central Spitsbergen (Arctic Norway), as mapped by reflection seismic data. *Norwegian Journal of Geology*, 92(4).

Beliveau, D., Payne, D. A., Mundry, M., et al. (1993). Waterflood and CO2 Flood of the Fractured Midale Field (includes associated paper 22947). *Journal of Petroleum Technology*, 45(09):881–817.

Bell, F. (1993). *Engineering Geology*. Wiley.

Bergh, S. G. and Andresen, A. (1990). Structural development of the Tertiary fold-and-thrust belt in east Oscar II Land, Spitsbergen. *Polar Research*, 8(2):217–236.

Bergh, S. G., Braathen, A., and Andresen, A. (1997). Interaction of basement-involved and thin-skinned tectonism in the Tertiary fold-thrust belt of central Spitsbergen, Svalbard. *AAPG bulletin*, 81(4):637–661.

Billings, M. P. (1972). *Structural geology*. Prentice-Hall, Englewood Cliffs, N.J, 3rd ed. edition.

Birchall, T., Senger, K., and Olaussen, S. (2018). Subnormal pressure regimes of the northern Barents Shelf: causes and implications for hydrocarbon exploration. In *80th EAGE Conference and Exhibition 2018*, pages 1–5. European Association of Geoscientists & Engineers.

Birol, F. (2010). World Energy Outlook 2010. Technical report, International Energy Agency, Paris.

Blinova, M., Faleide, J. I., Gabrielsen, R. H., and Mjelde, R. (2013). Analysis of structural trends of sub-sea-floor strata in the Isfjorden area of the West Spitsbergen Fold-and-Thrust Belt based on multichannel seismic data. *Journal of the Geological Society*, 170(4):657–668.

Bohloli, B., Skurtveit, E., Grande, L., Titlestad, G. O., Børresen, M., Johnsen, Ø., and Braathen, A. (2014). Evaluation of reservoir and cap-rock integrity for the Longyearbyen CO2 storage pilot based on laboratory experiments and injection tests. *Norwegian Journal of Geology*, 94(2–3):171–187.

Boyer, S. E. and Elliott, D. (1982). Thrust systems. *Aapg Bulletin*, 66(9):1196–1230.

Braathen, A., Baelum, K., Christiansen, H., Dahl, T., Eiken, O., Elvebakk, H., Hansen, F., Hanssen, T., Jochmann, M., Johansen, T. A., Johnsen, H., Larsen, L., Lie, T., Mertes, J., Mork, A., Mørk, M., Nemec, W., Olaussen, S., Oye, V., and Vagle, K. (2012). The Longyearbyen CO2 lab of Svalbard, Norway – initial assessment of the geological conditions for CO2 sequestration. *Norwegian Journal of Geology*, 92:353–376.

Braathen, A., Bergh, S., Karlsen, F., Maher, H., Andresen, A., Hansen, A.-I., and Bergvik, A. (1999). Kinematics of the Isfjorden-Ymerbukta Fault Zone: a dextral oblique-thrust ramp in the Tertiary fold-thrust belt of Spitsbergen. *Norwegian Journal of Geology*, 79(4):227–240.

Braathen, A., Sand, G., Mørk, A., Jensen, M., Bælum, K., and Elvebakk (2010). Longyearbyen co2 lab – prospects after the pilot project. In *Nordic Geological Winter Meeting 2010*.

Busch, A., Alles, S., Gensterblum, Y., Prinz, D., Dewhurst, D. N., Raven, M. D., Stanjek, H., and Krooss, B. M. (2008). Carbon dioxide storage potential of shales. *International journal of greenhouse gas control*, 2(3):297–308.

Butler, R. W. (1982). The terminology of structures in thrust belts. *Journal of Structural Geology*, 4(3):239–245.

Caillet, G. (1993). The caprock of the Snorre Field, Norway: a possible leakage by hydraulic fracturing. *Marine and Petroleum Geology*, 10(1):42–50.

Carey, J. W., Lei, Z., Rougier, E., Mori, H., and Viswanathan, H. (2015). Fracture-permeability behavior of shale. *Journal of unconventional oil and gas resources*, 11:27–43.

Cobbold, P. R. and Rodrigues, N. (2007). Seepage forces, important factors in the formation of horizontal hydraulic fractures and bedding-parallel fibrous veins ('beef'and 'cone-in-cone'). *Geofluids*, 7(3):313–322.

Cook, F. A. and Varsek, J. L. (1994). Orogen-scale decollements. *Reviews of Geophysics*, 32(1):37–60.

Crider, J. G. and Peacock, D. C. (2004). Initiation of brittle faults in the upper crust: a review of field observations. *Journal of Structural Geology*, 26(4):691–707.

Dallmann, W. K. (1999). *Lithostratigraphic Lexicon of Svalbard: Review and Recommendations for Nomenclature Use : Upper Palaeozoic to Quaternary Bedrock*. Norsk Polarinstitutt.

Dallmann, W. K., Elvevold, S., Gerland, S., Hormes, A., Majka, J., Ottemöller, L., Pavlova, O., and Sander, G. (2015). *Geoscience atlas of Svalbard*. Norsk Polarinstitutt.

Dörr, N., Clift, P., Lisker, F., and Spiegel, C. (2013). Why is Svalbard an island? Evidence for two-stage uplift, magmatic underplating, and mantle thermal anomalies. *Tectonics*, 32(3):473–486.

Dypvik, H. (1984). Jurassic and Cretaceous black shales of the Janusfjellet formation, Svalbard, Norway. *Sedimentary Geology*, 41(2-4):235–248.

Dypvik, H., Eikeland, T., Backer-Owe, K., Andresen, A., Johanen, H., Elverhøi, A., Nagy, J., Haremo, P., and Biærke, T. (1991). The Janusfjellet Subgroup (Bathonian to Hauterivian) on central Spitsbergen: a revised lithostratigraphy. *Polar Research*, 9(1):21–44.

Dypvik, H. and Harris, N. B. (2001). Geochemical facies analysis of fine-grained siliciclastics using Th/U, Zr/Rb and (Zr+ Rb)/Sr ratios. *Chemical Geology*, 181(1-4):131–146.

Edlmann, K., Haszeldine, S., and McDermott, C. (2013). Experimental investigation into the sealing capability of naturally fractured shale caprocks to supercritical carbon dioxide flow. *Environmental earth sciences*, 70(7):3393–3409.

Elvebakk, H. (2010). Results of borehole logging in well LYB CO2, Dh4 of 2009, Longyearbyen, Svalbard. *NGU, Trondheim, Norway*, 35.

Faleide, J. I., Gudlaugsson, S. T., and Jacquart, G. (1984). Evolution of the western Barents Sea. *Marine and Petroleum geology*, 1(2):123–150.

Festøy, M. H. (2017). Integrated characterization of igneous intrusions in Central Spitsbergen. Master's thesis, University of Tromsø.

Forster, A., Norden, B., Zinck-Jørgensen, K., Frykman, P., Kulenkampff, J., Spangenberg, E., Erzinger, J., Zimmer, M., Kopp, J., Borm, G., et al. (2006). Baseline characterization of the CO2SINK geological storage site at Ketzin, Germany. *Environmental Geosciences*, 13(3):145–161.

Fossen, H. (2010). *Structural Geology*. Cambridge University Press.

Fossen, H. (2016). *Structural geology*. Cambridge University Press.

Fossen, H. and Bale, A. (2007). Deformation bands and their influence on fluid flow. *AAPG bulletin*, 91(12):1685–1700.

Gabrielsen, R. and Kløvjan, O. (1997). Late Jurassic—early Cretaceous caprocks of the southwestern Barents Sea: fracture systems and rock mechanical properties. In *Norwegian Petroleum Society Special Publications*, volume 7, pages 73–89. Elsevier.

Gale, J. F., Laubach, S. E., Olson, J. E., Eichhubl, P., and Fall, A. (2014). Natural fractures in shale: A review and new observationsNatural Fractures in Shale: A Review and New Observations. *AAPG bulletin*, 98(11):2165–2216.

Geological Time Scale Foundation (2016). Barents sea chart. `https://timescalefoundation.org/resources/NW_Europe_Lex/litho/Barents_Chart.php`.

Grundvåg, S.-A., Jelby, M. E., Śliwińska, K. K., Nøhr-Hansen, H., Aadland, T., Sandvik, S. E., Tennvassås, I., Engen, T., and Olaussen, S. (2019). Sedimentology and palynology of the Lower Cretaceous succession of central Spitsbergen: integration of subsurface and outcrop data. *Norwegian Journal of Geology*.

Guo, Z., Li, X.-Y., Liu, C., Feng, X., and Shen, Y. (2013). A shale rock physics model for analysis of brittleness index, mineralogy and porosity in the barnett shale. *Journal of Geophysics and Engineering*, 10(2):025006.

Hancock, P. (1985). Brittle microtectonics: principles and practice. *Journal of structural geology*, 7(3-4):437–457.

Harland, W. B. (1997). Part 1: Chapter 3 Svalbard's geological frame. *Geological Society, London, Memoirs*, 17(1):23–46.

Henriksen, E., Bjørnseth, H., Hals, T., Heide, T., Kiryukhina, T., Kløvjan, O., Larssen, G., Ryseth, A., Rønning, K., Sollid, K., et al. (2011). Uplift and erosion of the greater Barents Sea: impact on prospectivity and petroleum systems. *Geological Society, London, Memoirs*, 35(1):271–281.

Huq, F., Smalley, P. C., Mørkved, P. T., Johansen, I., Yarushina, V., and Johansen, H. (2017). The Longyearbyen CO2 Lab: Fluid communication in reservoir and caprock. *International Journal of Greenhouse Gas Control*, 63:59–76.

Koevoets, M. J., Hammer, Ø., Olaussen, S., Senger, K., and Smelror, M. (2018). Integrating subsurface and outcrop data of the Middle Jurassic to Lower Cretaceous Agardhfjellet Formation in central Spitsbergen. *Norwegian Journal of Geology*, 98(4).

Kohlstedt, D. L., Evans, B., and Mackwell, S. J. (1995). Strength of the lithosphere: Constraints imposed by laboratory experiments. *Journal of Geophysical Research: Solid Earth*, 100(B9):17587–17602.

Laubach, S. E., Lander, R., Criscenti, L. J., Anovitz, L. M., Urai, J., Pollyea, R., Hooker, J. N., Narr, W., Evans, M. A., Kerisit, S. N., et al. (2019). The role of chemistry in fracture pattern development and opportunities to advance interpretations of geological materials. *Reviews of Geophysics*, 57(3):1065–1111.

Laubach, S. E., Olson, J. E., and Gross, M. R. (2009). Mechanical and fracture stratigraphy. *AAPG bulletin*, 93(11):1413–1426.

Lavadera, P. L., Kühn, D., Dando, B., Lecomte, I., Senger, K., and Drottning, Å. (2018). CO2 storage in the high Arctic: efficient modelling of pre-stack depth-migrated seismic sections for survey planning. *Geophysical Prospecting*, 66(6):1180–1200.

Lord, G. S. (2013). Steep Fracture Patterns and Their Characteristics Within The Triassic De Geerdalen Formation On Svalbard: An emphasis on regional trends, local variations and lithological controls. Master's thesis, Institutt for geologi og bergteknikk.

Maher, H., Bergh, S., Braathen, A., Manby, G., and Lyeberis, N. (2001). Discussion on pre-ocean opening compression of the Northwestern Atlantic margin: evidence from eastern Greenland: Journal, Vol. 157, 2000, 707–710. *Journal of the Geological Society*, 158(4):728–730.

Maher, S., Gee, J., Doran, A., Cheadle, M., and John, B. (2020). Magnetic Structure of Fast-Spread Oceanic Crust at Pito Deep. *Geochemistry, Geophysics, Geosystems*, 21(2):e2019GC008671.

Major, H., Haremo, P., Dallmann, W., and Andresen, A. (2000). Geological Map of Svalbard, 1: 100,000, Sheet C9G Adventdalen. *Norsk Polarinstitutt Temakart*, 31.

Marshall, C., Large, D. J., Meredith, W., Snape, C. E., Uguna, C., Spiro, B. F., Orheim, A., Jochmann, M., Mokogwu, I., Wang, Y., et al. (2015a). Geochemistry and petrology of Palaeocene coals from Spitsbergen—Part 1: Oil potential and depositional environment. *International Journal of Coal Geology*, 143:22–33.

Marshall, C., Uguna, J., Large, D. J., Meredith, W., Jochmann, M., Friis, B., Vane, C., Spiro, B. F., Snape, C. E., and Orheim, A. (2015b). Geochemistry and petrology of palaeocene coals from Spitzbergen—Part 2: Maturity variations and implications for local and regional burial models. *International Journal of Coal Geology*, 143:1–10.

McClay, K. (1992). Glossary of thrust tectonics terms. *Thrust tectonics*, pages 419–433.

McClay, K. and Insley, M. (1986). Duplex structures in the Lewis thrust sheet, Crowsnest pass, Rocky Mountains, Alberta, Canada. *Journal of Structural Geology*, 8(8):911–922.

McKerrow, W., Mac Niocaill, C., and Dewey, J. (2000). The caledonian orogeny redefined. *Journal of the Geological society*, 157(6):1149–1154.

Metz, B., Davidson, O., de Conic, H., Loos, M., and Meyer, L. E. (2005). IPCC Special Report on Carbon dioxide Capture and Storage. Technical report, IPCC.

Midtkandal, I., Holbrook, J. M., Faleide, J. I., Myers, C., van Yperen, A. E., Shephard, G. E., and Nystuen, J. P. (2018). Early Cretaceous Arctic palaeotopography as constrained by Barents Sea sediment budget. In *AGU Fall Meeting Abstracts*.

Midtkandal, I. and Nystuen, J. (2009). Depositional architecture of a low-gradient ramp shelf in an epicontinental sea: the lower Cretaceous of Svalbard. *Basin Research*, 21(5):655–675.

Miller, R. B. and Paterson, S. R. (1994). The transition from magmatic to high-temperature solid-state deformation: implications from the Mount Stuart batholith, Washington. *Journal of Structural Geology*, 16(6):853–865.

Moore, D. M. and Reynolds, R. C. (1997). X-ray diffraction and the identification and analysis of clay minerals.

Mulrooney, M. J., Larsen, L., Van Stappen, J., Rismyhr, B., Senger, K., Braathen, A., Olaussen, S., Mørk, M. B. E., Ogata, K., and Cnudde, V. (2019). Fluid flow properties of the Wilhelmøya Subgroup, a potential unconventional CO2 storage unit in central Spitsbergen. *Norwegian Journal of Geology*.

Nakken, L. (2020). Structural evolution of the lower Agardhfjellet Formation, in Central Spitsbergen. Master's thesis, University of Oslo.

Nejbert, K., Krajewski, K. P., Dubinska, E., and Pecskay, Z. (2011). Dolerites of Svalbard, north-west Barents Sea Shelf: age, tectonic setting and significance for geotectonic interpretation of the High-Arctic Large Igneous Province. *Polar Research*, 30(1):7306.

Nelson, R. (1985). *Geologic analysis of naturally fractured reservoirs*. Gulf Publishing Co., Houston, TX.

Norwegian Polar Institute (2012). Svalbardkartet. `https://geokart.npolar.no/Html5Viewer/index.html?viewer=Svalbardkartet`.

Nøttvedt, A., Cecchi, M., Gjelberg, J., Kristensen, S., Lønøy, A., Rasmussen, A., Rasmussen, E., Skott, P., and Van Veen, P. (1993). Svalbard-Barents Sea correlation: a short review. In *Norwegian Petroleum Society Special Publications*, volume 2, pages 363–375. Elsevier.

Nygård, R., Gutierrez, M., Bratli, R. K., and Høeg, K. (2006). Brittle–ductile transition, shear failure and leakage in shales and mudrocks. *Marine and Petroleum Geology*, 23(2):201–212.

Ogata, K., Senger, K., Braathen, A., Tveranger, J., and Olaussen, S. (2014a). Fracture systems and mesoscale structural patterns in the siliciclastic Mesozoic reservoir-caprock succession of the Longyearbyen CO 2 Lab project: Implications for geological CO 2 sequestration in Central Spitsbergen, Svalbard. *Norwegian Journal of Geology/Norsk Geologisk Forening*, 94.

Ogata, K., Senger, K., Braathen, A., Tveranger, J., and Olaussen, S. (2014b). The importance of natural fractures in a tight reservoir for potential CO2 storage: a case study of the upper Triassic–middle Jurassic Kapp Toscana Group (Spitsbergen, Arctic Norway). *Geological Society, London, Special Publications*, 374(1):395–415.

Ohm, S. E., Larsen, L., Olaussen, S., Senger, K., Birchall, T., Demchuk, T., Hodson, A., Johansen, I., Titlestad, G. O., Karlsen, D. A., et al. (2020). Discovery of shale gas in organic-rich Jurassic successions, Adventdalen, Central Spitsbergen, Norway. *Norwegian Journal of Geology*, 99(2).

Olaussen, S., Senger, K., Braathen, A., Grundvåg, S.-A., and Mørk, A. (2019). You learn as long as you drill; research synthesis from the Longyearbyen CO2 Laboratory, Svalbard, Norway. *Norwegian Journal of Geology*, 99(2):157–187.

Peacock, D., Nixon, C., Rotevatn, A., Sanderson, D., and Zuluaga, L. (2016). Glossary of fault and other fracture networks. *Journal of Structural Geology*, 92:12–29.

Poppe, L., Paskevich, V., Hathaway, J., and Blackwood, D. (2001). A laboratory manual for X-ray powder diffraction. *US Geological Survey open-file report*, 1(041):1–88.

Reed, S. J. B. (2005). *Electron microprobe analysis and scanning electron microscopy in geology*. Cambridge university press.

Rodrigues, N., Cobbold, P., and Løseth, H. (2009). Physical modelling of sand injectites. *Tectonophysics*, 474(3-4):610–632.

Rogelj, J., Den Elzen, M., Höhne, N., Fransen, T., Fekete, H., Winkler, H., Schaeffer, R., Sha, F., Riahi, K., and Meinshausen, M. (2016). Paris agreement climate proposals need a boost to keep warming well below 2 c. *Nature*, 534(7609):631–639.

Schaaf, N., Senger, K., Mulrooney, M., Ogata, K., Braathen, A., and Olaussen, S. (2017). Towards characterization of natural fractures in a caprock shale: an integrated borehole-outcrop study of the Agardhfjellet Formation, Svalbard. In *Norwegian Geological Society Winter Conference 2017*.

Schultz, R. A. and Fossen, H. (2002). Displacement–length scaling in three dimensions: the importance of aspect ratio and application to deformation bands. *Journal of Structural Geology*, 24(9):1389–1411.

Schultz, R. A. and Fossen, H. (2008). Terminology for structural discontinuities. *AAPG bulletin*, 92(7):853–867.

Senger, K., Roy, S., Braathen, A., Buckley, S. J., Bælum, K., Gernigon, L., Mjelde, R., Noormets, R., Ogata, K., Olaussen, S., et al. (2013). Geometries of doleritic intrusions in central Spitsbergen, Svalbard: an integrated study of an onshore-offshore magmatic province with implications for CO2 sequestration. *Geological controls on fluid flow and seepage in western Svalbard fjords, Norway. An integrated marine acoustic study*.

Senger, K., Tveranger, J., Braathen, A., Olaussen, S., Ogata, K., and Larsen, L. (2015). CO 2 storage resource estimates in unconventional reservoirs: insights from a pilot-sized storage site in Svalbard, Arctic Norway. *Environmental Earth Sciences*, 73(8):3987–4009.

Senger, K., Tveranger, J., Ogata, K., Braathen, A., and Planke, S. (2014). Late Mesozoic magmatism in Svalbard: A review. *Earth-Science Reviews*, 139:123–144.

Shaw, H. and Primmer, T. (1991). Diagenesis of mudrocks from the Kimmeridge clay formation of the Brae area, UK North Sea. *Marine and Petroleum Geology*, 8(3):270–277.

Singhal, B. B. S. and Gupta, R. P. (2010). *Applied hydrogeology of fractured rocks*. Springer Science & Business Media.

Smart, K. J., Ofoegbu, G. I., Morris, A. P., McGinnis, R. N., and Ferrill, D. A. (2014). Geomechanical modeling of hydraulic fracturing: Why mechanical stratigraphy, stress state, and pre-existing structure matter. *AAPG Bulletin*, 98(11):2237–2261.

Sone, H., Zoback, M., et al. (2011). Visco-plastic properties of shale gas reservoir rocks. In *45th US Rock Mechanics/Geomechanics Symposium*. American Rock Mechanics Association.

Song, J. and Zhang, D. (2013). Comprehensive review of caprock-sealing mechanisms for geologic carbon sequestration. *Environmental science & technology*, 47(1):9–22.

Steel, R. J. and Worsley, D. (1984). Svalbard's post-Caledonian strata—an atlas of sedimentational patterns and palaeogeographic evolution. In *Petroleum geology of the North European margin*, pages 109–135. Springer.

Tarduno, J., Brinkman, D., Renne, P., Cottrell, R., Scher, H., and Castillo, P. (1998a). Evidence for extreme climatic warmth from Late Cretaceous Arctic vertebrates. *Science*, 282(5397):2241–2243.

Tarduno, J., Brinkman, D., Renne, P., Cottrell, R., Scher, H., and Castillo, P. (1998b). Late Cretaceous Arctic volcanism: tectonic and climatic connections. In *Am. Geophys. Union Spring Meeting Abstracts. Washington, DC, Am. Geophys. Union*.

Tharp, T. M. (1987). Conditions for crack propagation by frost wedging. *Geological Society of America Bulletin*, 99(1):94–102.

Tobin, H., Vannucchi, P., and Meschede, M. (2001). Structure, inferred mechanical properties, and implications for fluid transport in the décollement zone, Costa Rica convergent margin. *Geology*, 29(10):907–910.

Torp, T. A. and Gale, J. (2004). Demonstrating storage of CO2 in geological reservoirs: The Sleipner and SACS projects. *Energy*, 29(9-10):1361–1369.

Van Stappen, J. F., Meftah, R., Boone, M. A., Bultreys, T., De Kock, T., Blykers, B. K., Senger, K., Olaussen, S., and Cnudde, V. (2018). In situ triaxial testing to determine fracture permeability and aperture distribution for CO2 sequestration in Svalbard, Norway. *Environmental science & technology*, 52(8):4546–4554.

Wang, F. P. and Gale, J. F. (2009). Screening criteria for shale-gas systems. *GCAGS Transactions*, 59:779–793.

Wennberg, O. P., Andresen, A., Hansen, S., and Bergh, S. G. (1994). Structural evolution of a frontal ramp section of the West Spitsbergen, Tertiary fold and thrust belt, north of Isfjorden, Spitsbergen. *Geological Magazine*, 131(1):67–80.

Wong, D. W., Gastineau, F. A., Gregorski, K. S., Tillin, S. J., and Pavlath, A. E. (1992). Chitosan-lipid films: microstructure and surface energy. *Journal of Agricultural and Food Chemistry*, 40(4):540–544.

Worsley, D. (2008). The post-Caledonian development of Svalbard and the western Barents Sea. *Polar Research*, 27(3):298–317.

Xue, Z., Tanase, D., and Watanabe, J. (2006). Estimation of CO2 saturation from time-lapse CO2 well logging in an onshore aquifer, Nagaoka, Japan. *Exploration Geophysics*, 37(1):19–29.

Zhang, D. and Song, J. (2014). Mechanisms for geological carbon sequestration. *Procedia IUTAm*, 10(0):319–327.

Appendix A

Mineralogy

Diffractograms from the bulk and clay XRD analyses are shown below with the interpretations done on them drawn in (Fig. A.3). In addition, graphs that were used to identify some of the minerals are also shown below.

A.1 Diffractograms derived from the bulk an clay XRD analyses

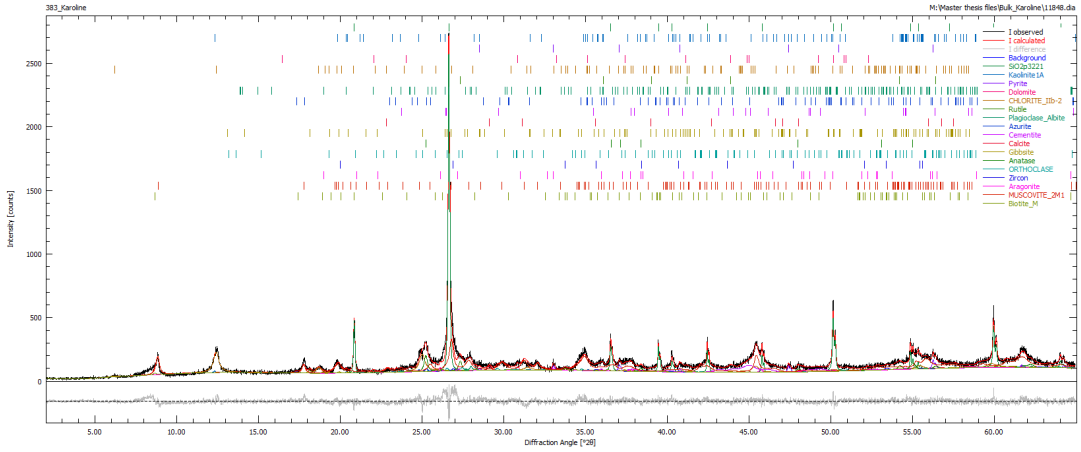

Figure A.1: Interpreted diffractograms from the bulk analysis conducted on sample S383.

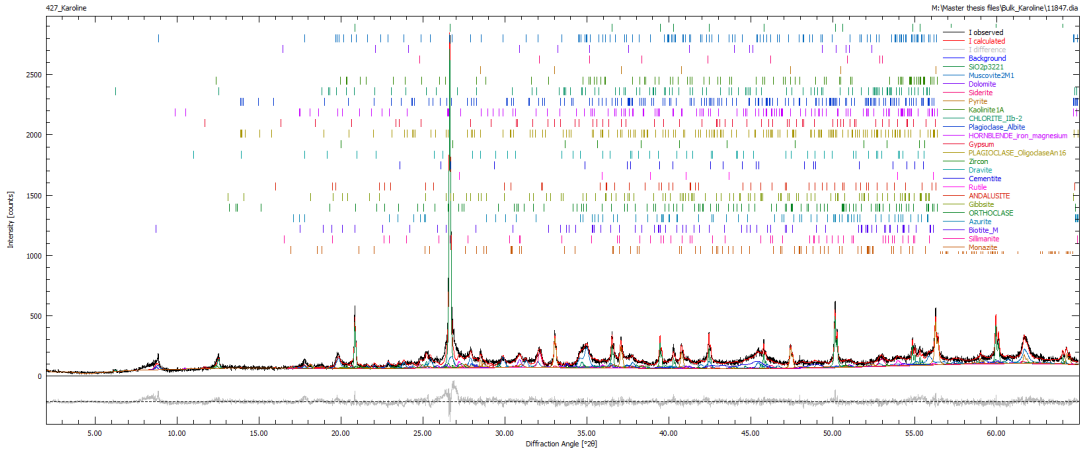

Figure A.2: Interpreted diffractograms from the bulk analysis conducted on sample S427

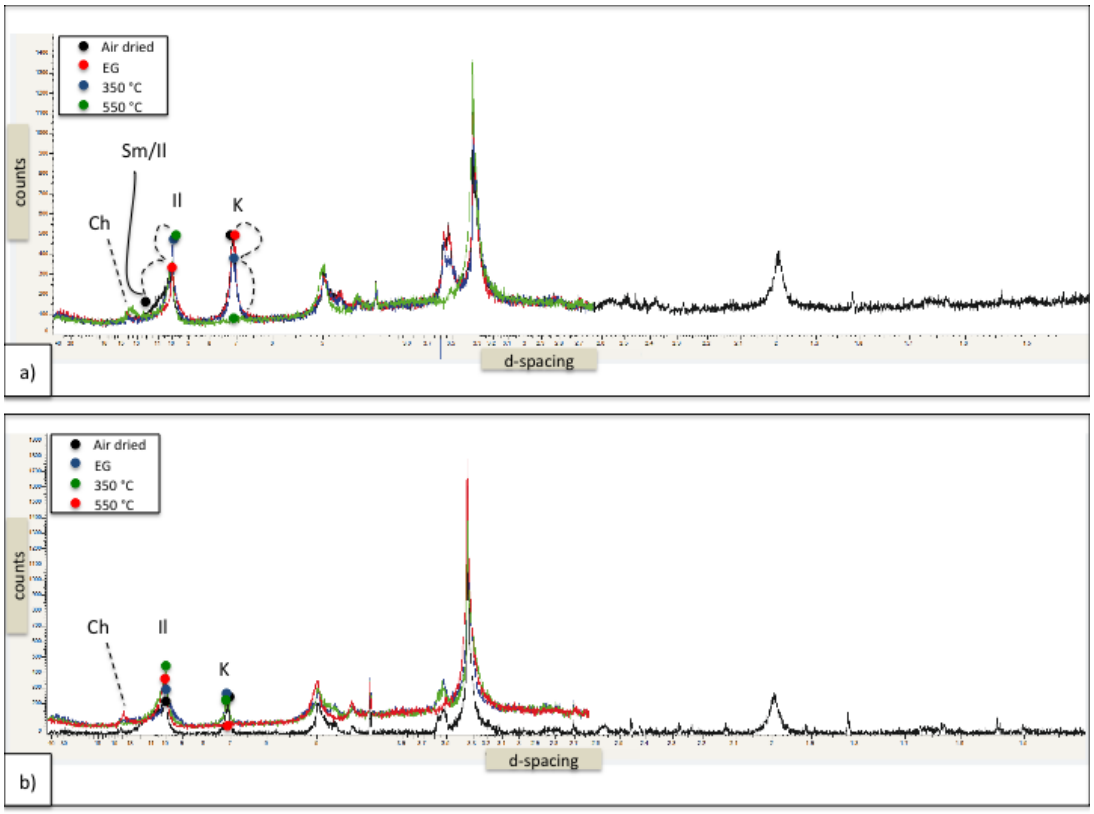

Figure A.3: Diffractograms for the two clay analyses conducted on samples from S383 and S427. a) the diffractogram for S383, b) the diffractogram for S427.

A.2 Graphs from SEM analysis

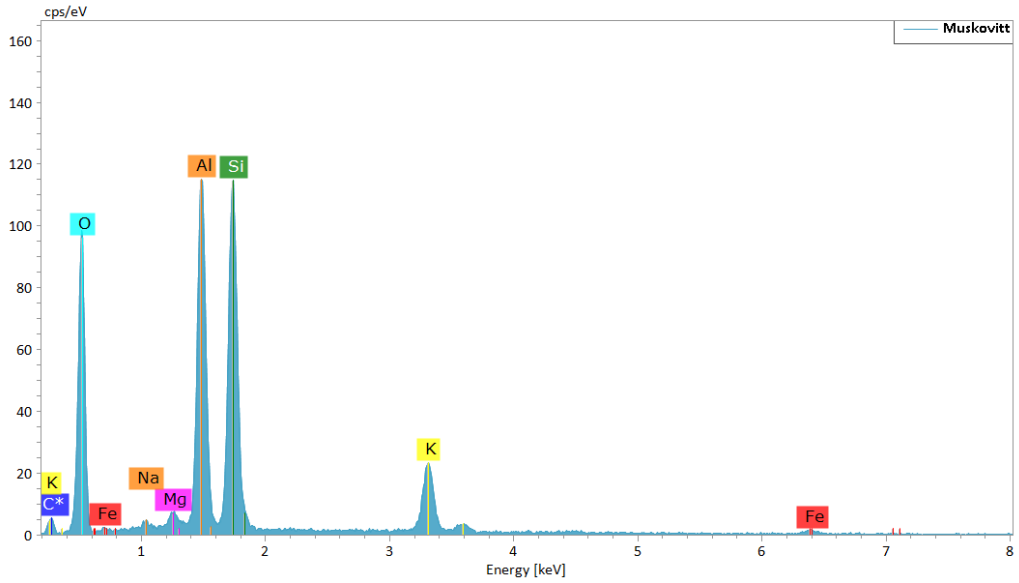

Figure A.4: Muscovite graph from the sample cut parallell to the direction of movement in sample S383.

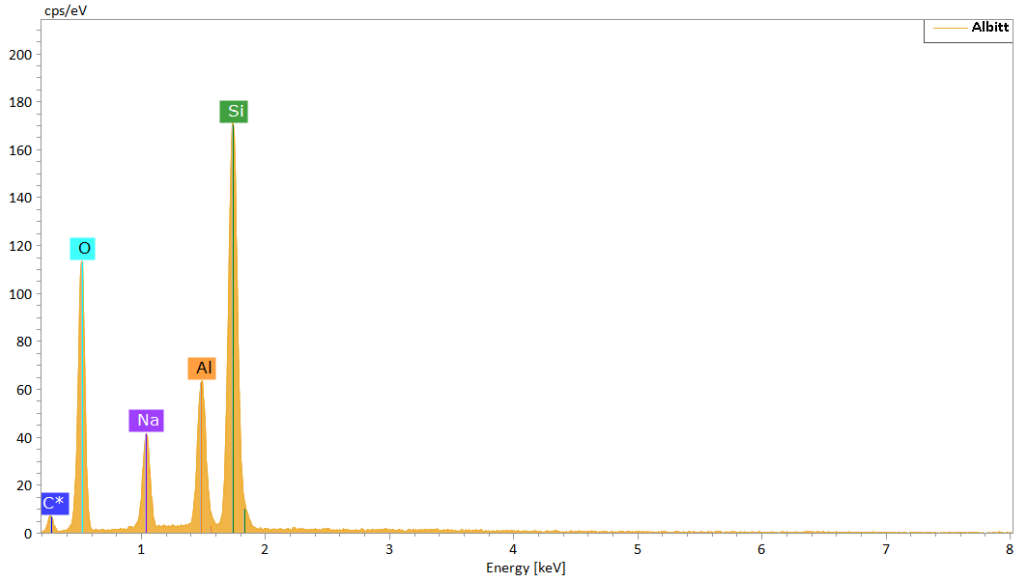

Figure A.5: Albite graph from the sample cut parallell to the direction of movement in sample S383.

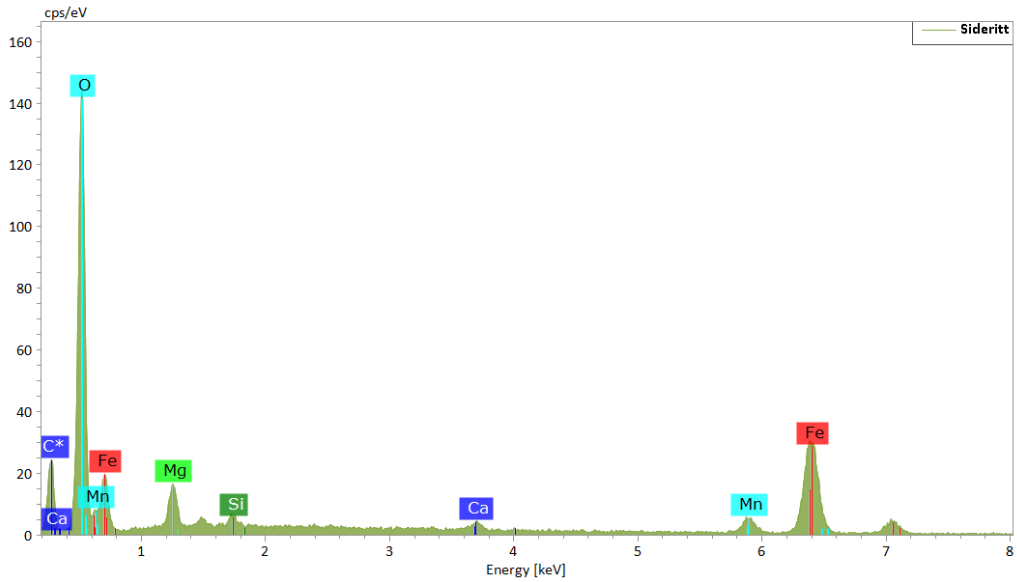

Figure A.6: Siderite graph from the sample cut parallell to the direction of movement in sample S383.

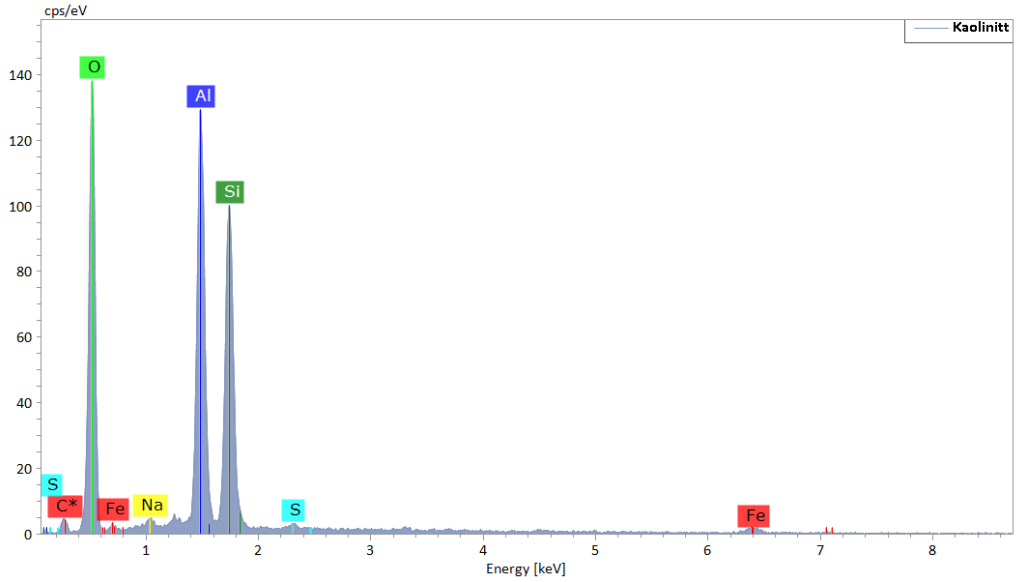

Figure A.7: Kaolinite graph from the sample cut parallell to the direction of movement in sample S383.

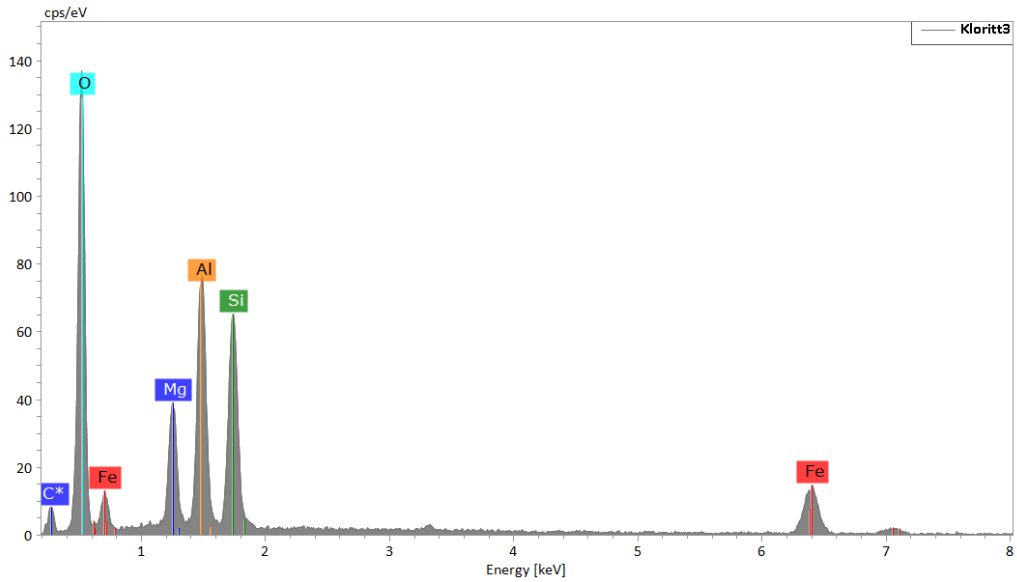

Figure A.8: Chlorite graph from the sample cut parallell to the direction of movement in sample S383.

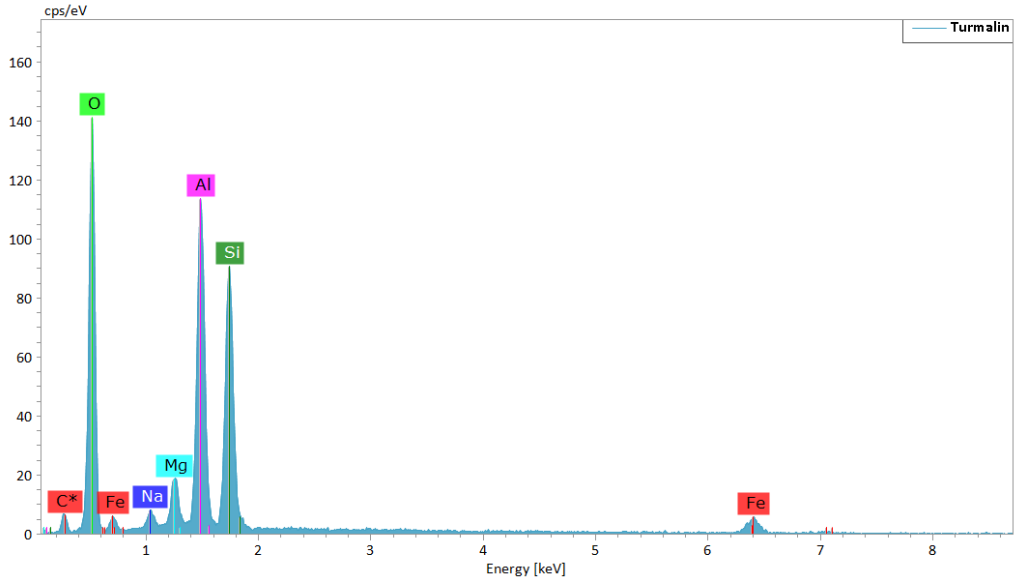

Figure A.9: Tourmaline graph from the sample cut parallell to the direction of movement in sample S383.

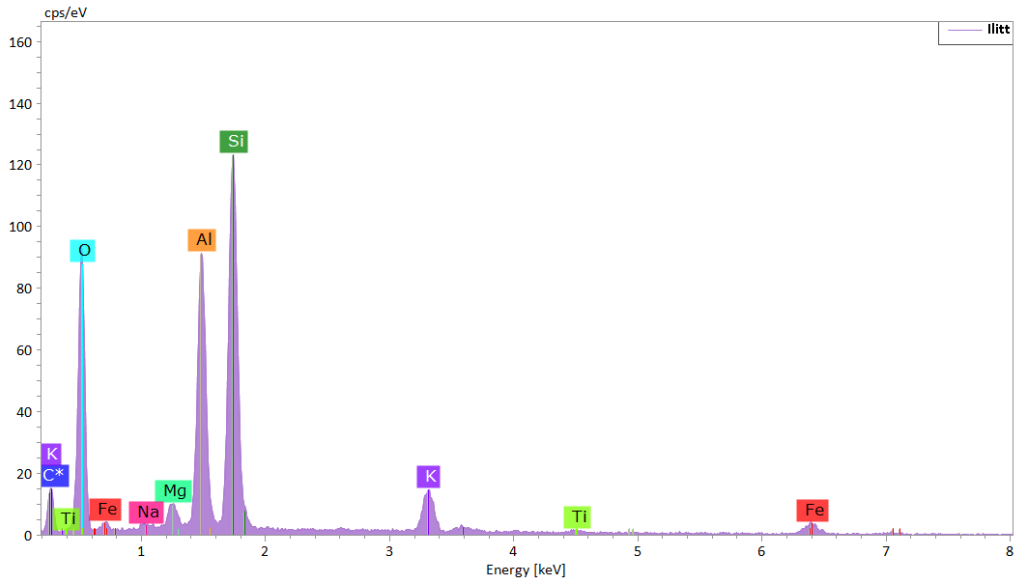

Figure A.10: Illite graph from the sample cut parallell to the direction of movement in sample S383.

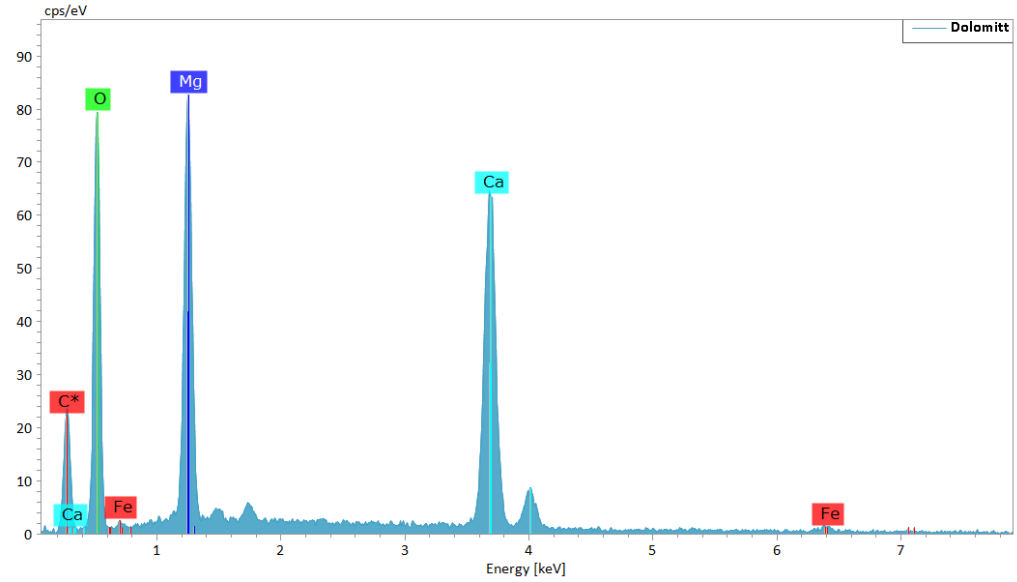

Figure A.11: Muscovite graph from the sample cut parallell to the direction of movement in sample S383.

Appendix B

Structural data

B.1 Outcrop data

In the field, the dominant fracture sets were distributed as in Table B.1.

Table B.1: Presence of the different fracture sets identified within each scanline produced.

Scanline	NNW–SSE	NW–SE	ENE–WSW/E–W	NE–SW	NNE–SSW
KW1	✓	✓	✓	–	–
KW2	✓	–	✓	✓	–
KW3	✓	✓	✓	✓	✓
KW4	✓	✓	–	✓	–
KW5	✓	✓	✓	✓	–

Fracture spacing observed in the scanlines

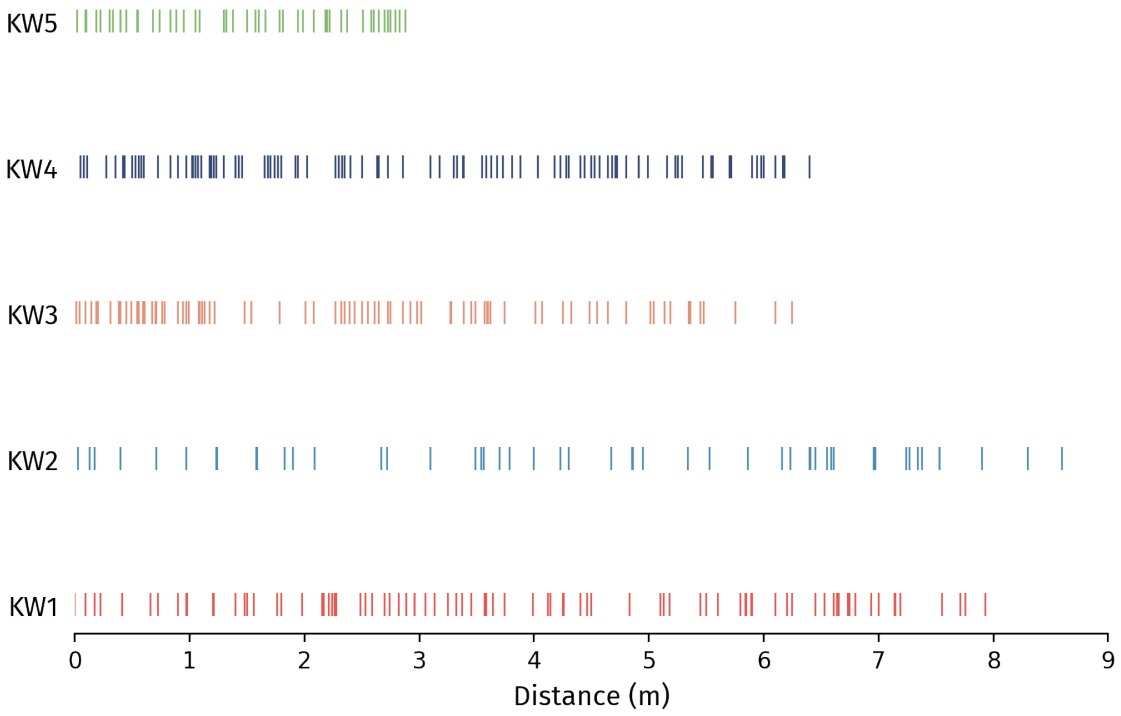

Figure B.1: Lateral fracture spacing observed in the scanlines obtained. Grey, horizontal line indicate approximately where the scanline was obtained.

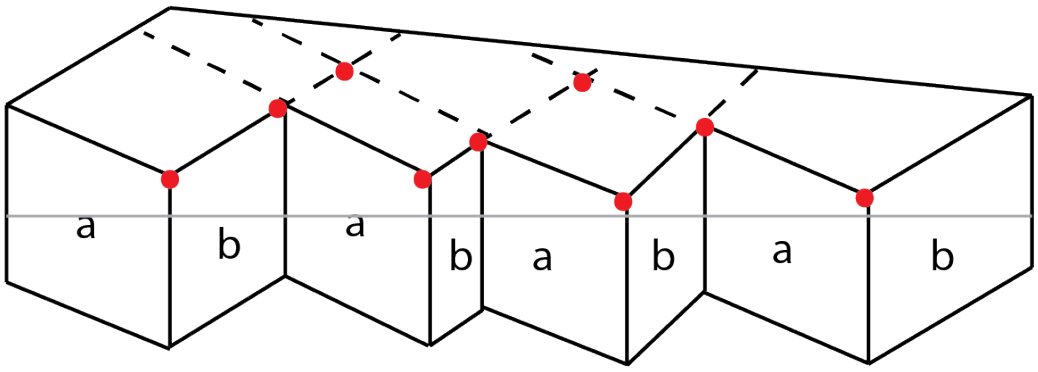

Figure B.2: Schematic illustration of how the faults might intersect in three dimensions. Based on photo from KW1.

B.2 Borehole data

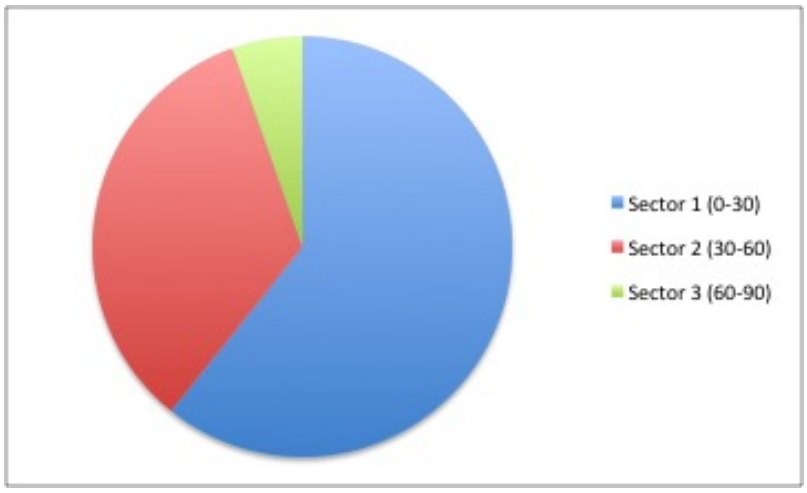

Figure B.3: Fracture dip angle distribution within DH2. Each sector is divided into intervals of 30°.

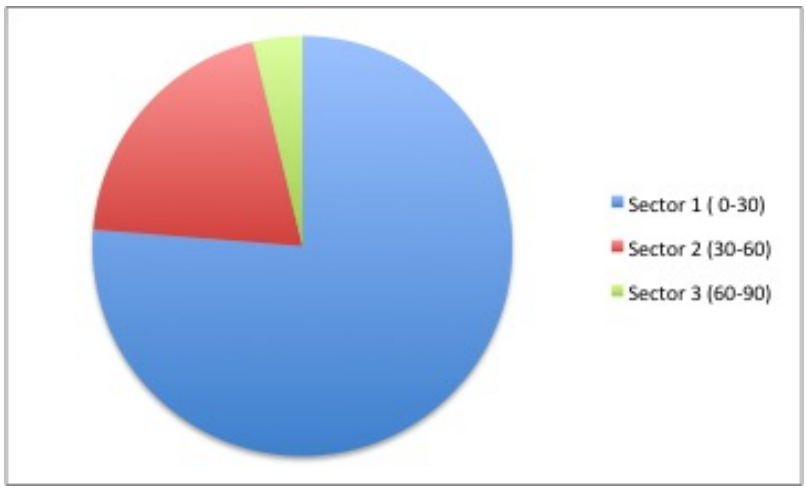

Figure B.4: Fracture dip angle distribution within DH4. Each sector is divided into intervals of 30°.

Appendix C

Contribution to the Nordic Geological Winter Meeting 2020

The preliminary results for this thesis were presented at the Nordic Geological Winter Meeting in Oslo, in January 2020. The results were presented alongside the work of co-student Lise Nakken, who studied the lower Agardhfjellet Formation.

Fracture characterization of the Agardhfjellet Formation in central Spitsbergen: insights from drill core and outcrop data

Løvlie[1, 2, *], K., Nakken[1, 2, #], L., Mulrooney[1], M., Senger[2], K., Schaaf[1, 2], N., Skurtveit[3, 1], E.

[1] Department of Geoscience, University of Oslo, Oslo, Norway
[2] Department of Arctic Geology, University Centre in Svalbard, Longyearbyen, Norway
[3] Norwegian Geotechnical Institute, Oslo, Norway
* email: karolihl@student.geo.uio.no
# email: lisena@student.geo.uio.no

The shale-dominated Upper Jurassic–Lower Cretaceous Agardhfjellet Formation forms the main top seal for the heterolithic reservoir of the Wilhelmøya Subgroup where CO_2 may be injected. The sealing integrity of the Agardhfjellet Formation is confirmed by a large pressure difference across the unit. However, structural characterization of the formation using drill cores and outcrop studies highlight an extensive natural fracture system in addition to several faults displacing up to 20(?) metres of strata. In view of possible CO_2 injection in the underlying aquifer, we strive to quantify to what extent these heterogeneities may affect the local caprock integrity. More specifically, a total of 322 meters of core was logged from two boreholes, DH2 and DH4.By defining a lower (Oppdalen and Lardyfjellet members) and an upper part (Slottsmøya Member) of the formation, we observe a significantly higher fracture frequency in the upper part. Generally, the fractures are sub-horizontal, polished and exhibit slickensides. In addition, the results reveal that finer grained units promote higher fracture frequencies. Further, we conducted a structural characterization of the formation where it outcrops 15km northeast of the boreholes. The structural characterization consisted of sedimentary logging, structural mapping and virtual outcrop modeling. The preliminary results reveal two sets of steeply dipping fractures, with a NE-SW and NW-SE orientation. In addition, sub-seismic structures were observed in the study area. Within the lower part of the formation, extensional faults with a NE-SW orientation were mapped where compressional features, such as reverse faults, were observed in the upper part of the formation. The reverse faults exhibit a NW-SE orientation. Fault and fracture orientations generally coincide with an overall northeast – southwest compressional regime associated with the Western Spitsbergen fold-and-thrust-belt. Integrating the core- and outcrop data, we define fracture networks that potentially affect the caprock integrity of the Agardhfjellet Formation. Provisional results suggest extensive fracturing in the upper part, promoting fluid flow, whereas fewer migration pathways occur in the lower part.

Fracture characterization of the Agardhfjellet Formation in central Spitsbergen: insights from drill core and outcrop data

K.H. Løvlie[1,2], L. Nakken[1,2], M.J. Mulrooney[1], K. Senger[2], N. Schaaf[1,2], E. Skurtveit[3,1].

[1] Department of Geoscience, University of Oslo, Oslo, Norway
[2] Department of Arctic Geology, University Centre in Svalbard, Longyearbyen, Norway
[3] Norwegian Geotechnical Institute, Oslo, Norway

Introduction

In this study, a structural characterization of the Upper Jurassic-Lower Cretaceous, shale dominated Agardhfjellet Formation at central Spitsbergen has been conducted. The formation consists of four members of which, three have been investigated herein. The Oppdalen and Lardyfjellet members are the lower-most, while the Slottsmøya Member is the upper-most (Dypvik et al., 1991). The study comprises data collected from outcrops at Deltaneset, located 15 km north of Longyearbyen, and two drill cores (DH2 and DH4) from boreholes in the Adventdalen area (Fig. 1). Due to uplift in the North of Svalbard, the stratigraphy dips southwards, as such the same stratigraphic units can be studied in outcrop (Henriksen et al., 2011).

The UNIS CO_2 LAB pilot project, located in Adventdalen, Central Spitsbergen investigated the possibility of capturing CO_2 from Longyearbyen´s coal-fueled power plant and injecting it into the subsurface for permanent storage (Fig. 1). The Agardhfjellet Formation forms the main top seal in this project, and a pressure difference has been recorded between the formation and the overburden (Braathen et al., 2012). This contribution aims to quantify how discontinuities within the Agardhfjellet Formation may affect local caprock integrity, by looking at data from drill cores and outcrop studies.

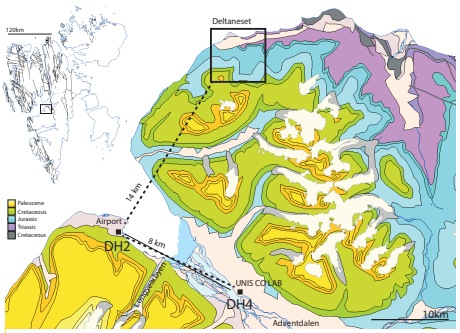

Figure 1: Overview map of Svalbard with major N-S-trending structures. Geological map of the study area, displaying the stratigraphy present. The location for the outcrop studies, Deltaneset, is marked with a black box. The locations of the two boreholes, where the cores are obtained, are marked with black squares. Basemap from NPD.

Method

The structural characterization herein integrates data from the subsurface in Adventdalen and outcrop studies conducted on Deltaneset (Fig. 1). Detailed structural logging (following the method of Singhal & Gupta, 2010) of 251 meters of cores has been performed. Orientations, dips, stratigraphic positions, spacing and frequency, surface asperity, and coating and infillings of fractures were recorded. This gives a vertical fracture frequency. The field investigations consisted of structural mapping using the same method as described above. Scanlines, i.e., the 1-d line intersection method, were produced. These were constructed in order to display the horizontal fracture frequency, counting the number of fractures per meter laterally. In addition, sedimentary logging and virtual outcrop modeling was conducted in order to connect the fracture analysis to the stratigraphy and to conduct further analyses of the faults and fractures from the virtual outcrops. By combining the vertical and horizontal data from respectively core and outcrop studies, structural characterization is conducted identifying fracture networks.

Results: Drill core

A significantly higher fracture frequency is observed within the upper part of the Slottsmøya Member compared to the two lower members, the Oppdalen and Lardyfjellet members (Fig. 2). The finer grained units within these members promote a higher frequency of fracturing, showing up to 34 fractures per meter. Within the coarser grained intervals, frequencies of between 0 and 8 fractures per meter are recorded. The fractures are generally sub-horizontal, but all dip angles are represented (Fig. 2). Mainly, polished surfaces with slickensides are observed. The fractures are predominantly open, but veins are also identified (Fig. 3). Un-logged intervals are represented by televiewer data provided by the UNIS CO2 Lab. In general, these data exhibit a much higher frequency than the logged intervals, with the highest counted fractures per meter being 54 (Fig. 2).

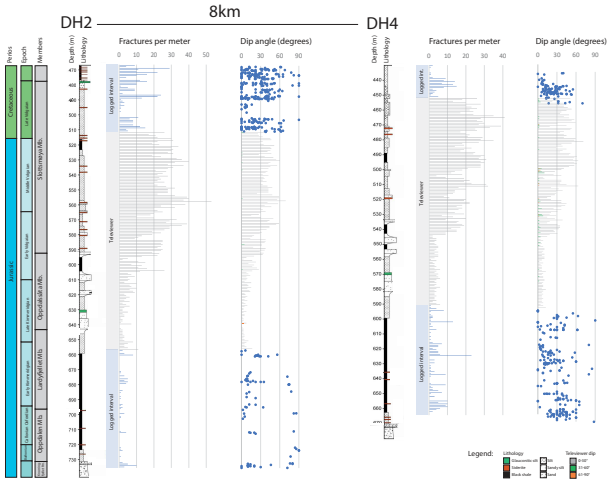

Figure 2: Results from the fracture analysis conducted on two intervals of DH2 and DH4. The histograms represent the number of fractures per meter at the given depth and the scatter plots represents measured dip angle of the fracture at the given depth. The interval in the middle is yet to be analyzed, and is represented with televiewer data. Dip data from televiewer is not measured dip but number of fractures exibiting a dip within three categories (see legend). For reference, logs from Koevoets et al. (2016) is used.

Figure 3: Photos from the fracture analysis. a) DH2 658.84m, b) DH2 659.95m, c) DH2 678.85m, d) DH2 675.84m, e) DH4 382.99m and f) DH4 439.64m. a) displaying a fracture of higher angle cutting two sub horizontal fractures. b) and c) displaying calcite veins and d)-f) displaying slip surfaces, which are partially polished slickensides. Core is 5cm in diameter.

Discussion

The dominant orientations of the faults and fractures generally coincide with an overall northeast – southwest contractional regime associated with the West Spitsbergen fold-and-thrust-belt (WSFTB). The upper part of the Slottsmøya Member is argued to be part of a detachment zone related to the WSFTB (Bergh et al., 1997). The results from the core analysis supports this, with an increased fracture frequency and crushed intervals observed in the upper part of the Slottsmøya Member.

The outcrop studies reveal through-going, steeply dipping fractures with an average horizontal frequency of 10, and a maximum of 24 fractures per meter. This maximum is recorded in an interval of increased fracture frequency near the normal fault in figure 5, which is interpreted as a damage zone. The sub-horizontal fractures observed in the cores are open with slickensides and exhibit an average of 1 fracture per meter in the two lowermost members and an average of 10 fractures per meter in the upper part of the Slottsmøya Member. The maximum frequency observed is 34 fractures per meter. The vertical and horizontal fractures connect in a fracture network allowing fluids to migrate. The observation of veins and mineral infills show fluids have previously been able to migrate within the prospective caprock.

Results: Outcrop

Within the Oppdalen and Lardyfjellet members, extensional faults showing up to 7 meters of displacement, striking NE—SW to ENE—WSW were mapped (Fig. 4). In the Slottsmøya Member, thrust faults exhibiting NW—SE orientations were observed (Fig. 3). The thrust faults have measured displacements of up to 1.8 meters. Scanlines (Fig. 5) revealed higher fracture frequencies within the finer grained beds and lower frequencies in well-cemented beds. In addition, the scanlines show higher fracture frequencies in the damage zone adjacent to the normal faults. The field studies show that the fracture sets observed are mainly through-going, steeply dipping, with ENE—WSW and N—S orientations (Fig. 6).

Upper Agardhfjellet Formation

Figure 4: Thrust faults observed in the Slottsmøya Member, showing a pop-up structure.

Lower Agardhfjellet Formation

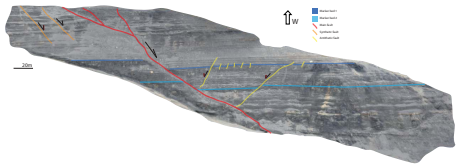

Figure 5: Normal fault, with adjacent synthetic and antithetic faults, observed in the lower part of the Agardhfjellet Formation. Scanline of marker bed 2 in figure 6b).

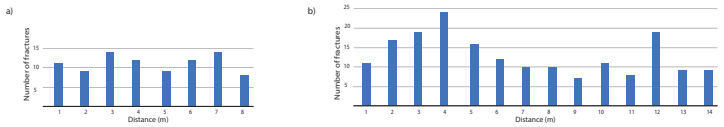

Figure 6: a) Scanline located in the Slottsmøya Member, obtained just below the thrust fault in figure 4. b) Scanline located in the Oppdalen Member in Marker bed 2 from both footwall (distance 1-4m) and hanging wall (distance 5-14m) of the main fault (fig. 5).

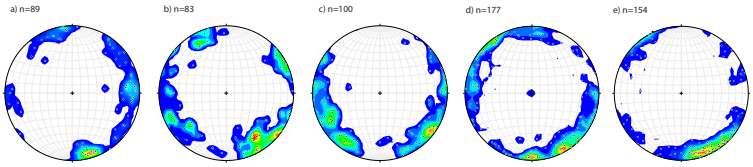

Figure 7: A total of 700 fractures, measured in 8 scanlines. a)-c) samples the Slottsmøya Member, where a) represents the lowermost part of the member and c) the uppermost part. a) plots the measured fractures from the scanline in figure 6a). d)-e) is obtained from the two lowermost members, the Oppdalen and Lardyfjellet members. d) plots the measured fractures from the scanline across the fault in figure 6b). n=number of fractures.

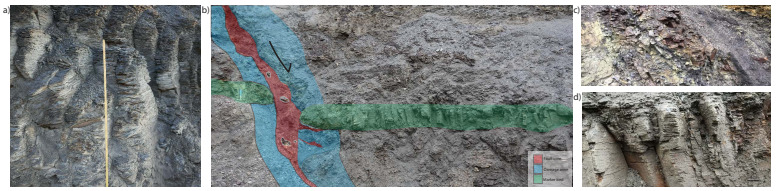

Figure 8: a) displays fractures from the obtained scanline in figure 6a). b) displays the lowermost part of the normal fault from figure 5, with a defined fault core and damage zone. c) close up of damage zone and d) marker bed in hanging wall.

Conclusion

- Higher frequencies of sub-horizontal fractures in the Upper part of the Slottsmøya Member, and higher frequencies of vertical fractures adjacent to the normal faults in the lower Oppdalen and Lardyfjellet members are recorded. This indicates that the WSFTB stress regime has controlled the fracturing.
- Highly fractured areas within the formation imply intervals of compromised caprock, but veins present and a confirmed pressure across the caprock in the borehole in Adventdalen, suggests barriers present resulting in a functional seal.

Acknowledgement

We would like to thank the Svalbard Science Forum (SSF) for funding the field campaigns for this project. Jan Christensen Legat provided resources beneficial for fieldwork. We also thank UiO for economic support in the completion of the fieldwork. Data access granted by the Longyearbyen CO_2 Lab is greatly appreciated. UNIS and UNIS Logistics are thanked for technical support during field season. NCCS are thanked. In addition, cooperation with Kei Ogata and field assistants Astrid Vikingstad, Matthjis Nuus, Peter Betlem, Rakul Johannesen and Tom Birchall is appreciated.

References

Bergh, S. G., Braathen, A., & Andresen, A. (1997). Interaction of basement-involved and thin-skinned tectonism in the Tertiary fold-thrust belt of central Spitsbergen, Svalbard. AAPG bulletin, 81(4), 637-661.
Dypvik, H., Eikeland, T. A., Backer-Owe, K., Andresen, A., Johanen, H., Elverhøi, A., ... & Bjærke, T. (1991). The Janusfjellet Subgroup (Bathonian to Hauterivian) on central Spitsbergen: a revised lithostratigraphy. Polar Research, 9(1), 21-44.
Henriksen, E., Bjørnseth, H. M., Hals, T. K., Heide, T., Kiryukhina, T., Kløvjan, O. S., ... & Stoupakova, A. (2011). Uplift and erosion of the greater Barents Sea: impact on prospectivity and petroleum systems. Geological Society, London, Memoirs, 35(1), 271-281.
Koevoets, M. J., Abay, T. B., Hammer, Ø., & Olaussen, S. (2016). High-resolution organic carbon–isotope stratigraphy of the Middle Jurassic–Lower Cretaceous Agardhfjellet Formation of central Spitsbergen, Svalbard. Palaeogeography, Palaeoclimatology, Palaeoecology, 449, 266-274.
Singhal, B. B. S., & Gupta, R. P. (2010). Applied hydrogeology of fractured rocks. Springer Science & Business Media.